LOW-ENERGY ELECTRON INDUCED PROCESSES IN MOLECULAR THIN FILMS CONDENSED ON SILICON AND TITANIUM DIOXIDE SURFACES

A Dissertation
Presented to
The Academic Faculty

By

Christopher D. Lane

In Partial Fulfillment
Of the Requirements for the Degree
Doctor of Philosophy in Chemistry

Georgia Institute of Technology

May, 2007

LOW-ENERGY ELECTRON INDUCED PROCESSES IN MOLECULAR THIN FILMS CONDENSED ON SILICON AND TITANIUM DIOXIDE SURFACES

Approved by:

Dr. Thomas M. Orlando, Advisor
School of Chemistry and Biochemistry
Georgia Institute of Technology

Dr. Z. John Zhang
School of Chemistry and Biochemistry
Georgia Institute of Technology

Dr. Mostafa A. El-Sayed
School of Chemistry and Biochemistry
Georgia Institute of Technology

Dr. Phillip N. First
School of Physics
Georgia Institute of Technology

Dr. Robert L. Whetten
School of Chemistry and Biochemistry
Georgia Institute of Technology

Date Approved: March 23, 2007

This thesis is dedicated to my parents, Gary and Judy Lane

ACKNOWLEDGEMENTS

First and foremost, I would like to thank my parents to whom this thesis is dedicated. Without their love, support, and life lessons, I would not have the foundation to attempt or persevere through the obstacles of graduate school. More thanks go to other people that have touched my life. I would like to thank my grandparents and extended family for their continual support; my brother, Joe, along with my close friends have always been a source of eternal friendship and an outlet for unwinding; and Mary Daula, who has been a invariable source of encouragement and a patient listener.

I would like to thank Mrs. Susan Smith, my high school chemistry teacher, for planting the seed for my interest in chemistry. Professors Farooq Khan, John Hansen, and Andrew Leavitt at the State University of West Georgia were more than mentors to me, but friends. With their instruction and the immense undergraduate research opportunities that they offered, my transition from undergraduate to graduate research was seamless.

Professor Thom Orlando has truly been an academic father. I can not appreciate his time, guidance, and encouragement more. During my graduate career, my fellow group members have been a source for advise, friendship, and venting frustrations. My past and present labmates include Jim Captain, Dr. Janine Captain, Matt Gilliland, Dr. Haiyan Chen, Dr. Yanfeng Chen, Dr. Taishan Fan, Kristin Sheppherd, Doogie Oh, Babajide Olanrewaju, Lan Sun, Ken Kite, and Marcus Johnson. Dr. Gregory Grieves and Dr. Alex Aleksandrov, the resident research scientists, have greatly contributed to my knowledge and research. Without their help, I could not call myself a scientist.

I must express my extreme gratitude to Dr. Nikolay Petrik and Dr. Greg Kimmel for allowing me to work with them at the Pacific Northwest National Laboratory. This was an opportunity to work with a first-class experimental vacuum chamber along with the people that move the scientific field. My interaction with Nick, Greg, and Mt. Rainier is an experience that I won't soon forget.

I would like to acknowledge the work of Carlson *et al*. and Chen *et al*. in Figure 2.1 and Q. Guo *et al*. in Figure 5.3 of this thesis. I would like to thank Dr. Jain Dong for his help taking the scanning electron microscopy images of the etched silicon surface presented in Figure 5.4. I would also like to acknowledge support for my work provided by the U.S. Department of Energy: Office of Basic Energy Sciences, the National Science Foundation awarded Nanoscience Interdisciplinary Research Team grant, and the Summer Research Institute on Interfacial and Condensed Phase Chemical Physics organized at the Pacific Northwest National Laboratory.

TABLE OF CONTENTS

LIST OF FIGURES

LIST OF SYMBOLS AND ABBREVIATIONS

θ	coverage
Å	Angstrom
amu	Atomic mass unit
arb. units	Arbitrary units
ASW	Amorphous solid water
BBO	Bridge bonding oxygen
BBO_V	Bridge bonding oxygen vacancy
CI	Crystalline water ice
cnts	Counts
DEA	Dissociative electron attachment
e^-	electrons
E_i	Incident electron energy
ESD	Electron-stimulated desorption
eV	Electron volt
(g)	Gas-phase
H_2O_{BBO}	Water adsorbed to bridge bonding oxygen
H_2O_{Ti}	Water adsorbed to titanium
Hz	Hertz
K	Kelvin
keV	Kiloelectron volt
kV	Kilovolts

meV	Millielectron volt
min	Minutes
ML	Monolayer
mm	Millimeter
mJ	Millijoules
μm	Microns
μs	Microseconds
mol	Molecules
N	Electron irradiation time
nm	Nanometer
ns	Nanosecond
OH_{BB}	Hydroxyl consisting of hydrogen on bridge bonding oxygen
OH_{Ti}	Hydroxyl group on titanium
O_{Ti}	Oxygen atom on titanium
PSD	Photon-stimulated desorption
QMS	Quadrupole mass spectrometer
REMPI	Resonance enhanced multi-photon ionization
s	Second
SEM	Scanning electron microscopy
STM	Scanning tunneling microscopy
TNI	Transient negative ion
TOF-MS	Time of flight mass spectrometer
TPD	Temperature programmed desorption

UHV	Ultra-high vacuum
UPS	Ultraviolet photoelectron spectroscopy
V	Volts

SUMMARY

The focus of the presented experimental research is to examine the fundamental physics and chemistry of electron-stimulated reactions upon adsorbate covered single crystal surfaces. Specifically, condensed $SiCl_4$ on the Si(111) surface and condensed H_2O on the TiO_2 (110) surface have been studied. By varying adsorbate film thicknesses, the coupling strength of the electron target molecule to the substrate and surrounding media dictates the progression of the electron induced reactions. To investigate the electron interactions with $SiCl_4$ on the Si(111) surface, a multilayer to monolayer approach was taken. Experiments measuring the electron stimulated desorption (ESD) of fragment cations are discussed in Chapter 3. ESD of neutrals was performed on a multilayer (100 ML) coverage of $SiCl_4$ and is discussed in Chapter 4. These experiments remove the influence of the silicon substrate on the electron induced dissociative processes that are monitored via time of flight mass spectrometry (ToF-MS). The results in Chapter 3 and Chapter 4 have been published in Surface Science 593 (2005) 173 and in the Journal of Chemical Physics 124 (2006) 164702, respectively. Results from electron induced reactions within thin films of $SiCl_4$ are presented in Chapter 5. In the low coverage region, the cation and neutral desorption channels are monitored simultaneously, and the adsorbate coupling strength to the silicon substrate is substantially greater. This affects the desorption yields and the autodetachment probability of the transient negative ion ($SiCl_4^-$).

Chapters 6 – 8 discuss work that focuses on the electron-stimulated reactions within the H_2O/TiO_2 system. A discussion of the interactions of H_2O with the TiO_2(110)

surface is presented in Chapter 6. The transition metal oxide surface is comprised of acidic and basic water adsorption sites along with intrinsic surface defects where surface oxygen atoms are missing. These surface defect sites significantly influence the interactions of water with the TiO_2 surface and consequently, govern much of the surface chemistry. Studies on electron induced oxidation of the TiO_2(110) surface and sputtering of H_2O from the TiO_2(110) surface are discussed in Chapter 7 and Chapter 8, respectively. The water interactions with the TiO_2 surface are revealed through the strong electron induced reaction dependencies on the amount of water present on the surface. Summarizing remarks and conclusions are presented in Chapter 9. Chapters 5, 7, and 8 represent papers which will be submitted for publication in the open scientific literature.

CHAPTER 1

INTRODUCTION

The objective of this research is to investigate the fundamental physics and chemistry of electron stimulated reactions upon adsorbate covered single crystal surfaces. This includes the initial inelastic electron scattering event that induces adsorbate decomposition into reactive fragment species that desorb, react with neighboring adsorbates, or react with the surface. More specifically, the experiments involve varying adsorbate film thicknesses to elucidate adsorbate coverage and substrate induced effects upon electron initiated reactions. Enhancement or suppression of electron stimulated surface reactions can be governed by whether the initial excitation occurs within the substrate, at the substrate-adsorbate interface, or within the bulk of the adsorbate film. Along with where the initial excitation occurs, the total film thickness determines the adsorbate target's coupling strength to the surface. Inevitably, these interactions dictate the excitation cross-sections, branching ratios for energy dissipation, and if dissociative, the escape probability from the surface.

The experimental results presented in this thesis is a culmination of experiments performed at the Georgia Institute of Technology and the Pacific Northwest National Laboratory which includes condensed $SiCl_4$ on the Si(111) surface and condensed H_2O on the TiO_2 (110) surface, respectively. Both adsorbate-substrate surface interfaces are model experimental systems and technologically relevant. Understanding the electron initiated non-thermal chemistry on each adsorbate-substrate system is pertinent for the

future developments in nanoscale plasma processing strategies and novel electrocatalytic electrode materials.

In addition, low energy electrons also stimulate chemistry at the adsorbate-substrate interface and in the thin adsorbate films consequent to high energy radiation bombardment. This is a result of the copious number of low energy secondary electrons that are generated during ionization events. These electrons must undergo inelastic scattering processes which include electron attachment. Electron attachment resonances that lead to dissociation are general and prevalent within the electron energy range of 1 – 20 eV which overlaps with secondary electron production distributions. Thus, the effective cross-section for chemical reactions due to electron attachment can be greatly enhanced. It has been shown that these resonances survive in thin films and the condensed phase [1]. Inelastic scattering of low-energy electrons and electron attachment resonances are discussed though much of this work, and a brief review is provided here.

A general diagram of some of the interactions that occur during electron scattering in this secondary electron energy range is presented in Figure 1.1(a). As an incident electron collides with a molecule (AB), pathways include: 1) elastic scattering, 2) inelastic scattering, 3) dissociation into neutrals, 4) dissociation into ground and excited state neutrals, 5) ionization of the parent molecule, 6) dissociation into a neutral and cation, 7) dissociation into an excited state neutral and cation, 8) ion-pair formation, and 9) electron attachment forming a transient negative ion (TNI). A summary of several of the important decay pathways of transient negative ions are shown in Figure 1.1(b). These include: 1) detachment without transfer of energy, 2) detachment leaving the neutral molecule in a rotationally and vibrationally excited state, 3) detachment leaving

the neutral molecule in an electronically, rotationally, and vibrationally excited state which can further dissociate, 4) dissociation producing a neutral and an anion, 5) dissociation producing an excited state neutral and an anion, 6) energy transfer that stabilizes the TNI, and 7) ionization through electron emission [2-4].

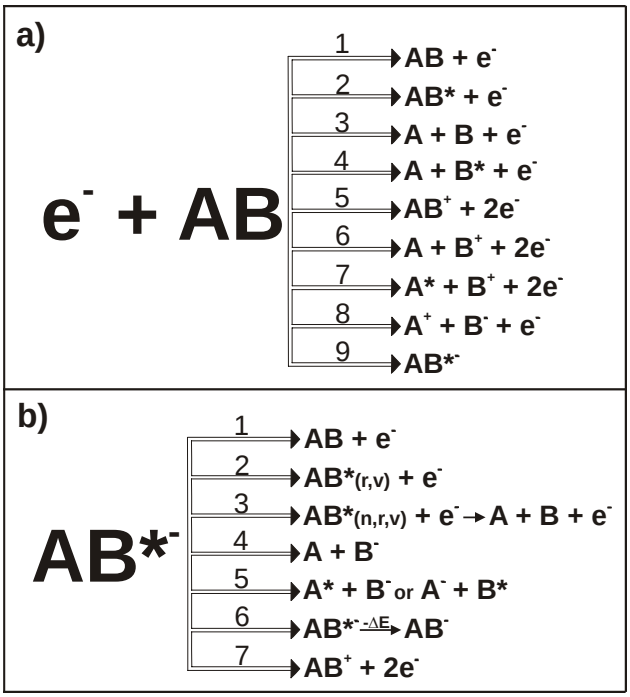

Figure 1.1 a) Possible processes that result from an electron collision with a target molecule, AB. b) Dissociation and energy dissipation pathways of the transient negative ion (TNI) created by electron attachment to AB. The labeled processes in each schematic are described in the text.

Transient negative ion resonances result when the ground or excited electronic states of molecular collision partners temporarily capture an incident electron during the electron-molecule collision. The simplest TNI is produced when the incident electron is trapped by the centrifugal potential arising from the interaction between the incident electron and the neutral molecule in its ground electronic state. These are referred to as single particle shape resonances. Shape resonances usually lie at energies above the

potential energy surfaces of the neutral molecule ground states. These resonances typically decay via autodetachment leaving the neutral molecule vibrationally and rotationally excited or via dissociative electron attachment (DEA) which involves the formation of anionic and neutral fragments. Shape resonances can also involve electronic excitations, and these core-excited shape resonances involve an attractive interaction between the incident electron and the excited state of the target molecule. Since the potential barrier is strongly dependent on the angular momentum value of the excited-state orbitals, resonances with *p*-, *d*- and *f*- wave character are expected. These resonances also lie above the neutral excited state energies and decay by autodetachment or DEA.

Another type of core excited resonance is referred to as a Feshbach (Type-I) resonance. This involves coupling of the kinetic energy of the captured electron to nuclear motion. If the incident electron excites a valence or shallow core level, a dynamic polarization is produced, and the electron can be temporarily trapped in the field of the excited target molecule. Electron correlation and reduced screening allows the incoming electron to couple to the excited electron and slightly positive core producing a one-hole, two-electron core-excited Feshbach resonance. These resonances lie below the corresponding excited states (i.e. they have a positive electron affinity). The energy gained in this correlation is referred to as the Feshbach decrement and is typically ~0.5 eV. As depicted in Figure 1.2, the transition is typically mediated by Frank Condon factors and the cross section is mediated by lifetimes against autodetachment and dissociative attachment [5]. The negative ion fragments are often produced with an excess kinetic energy which can be partitioned into reactive scattering events with

coadsorbed molecules or surface terminal groups. As illustrated in Figure 1.2, conservation of energy and momentum yields the most probable kinetic energy of the departing anion fragment, E_K^-, as:

$$E_K^- = (1-\beta)\,[\varepsilon + EA\,(B) - D\,(AB) - E_n] \qquad (1.1)$$

where β is the ratio of the mass of B^- to that of AB, ε is the captured electron's energy, EA (B) is the electron affinity of B, D (AB) is the bond energy of AB and E_n is the internal excitation energy of the fragments [6]. It is apparent that DEA favors the loss of the light fragment.

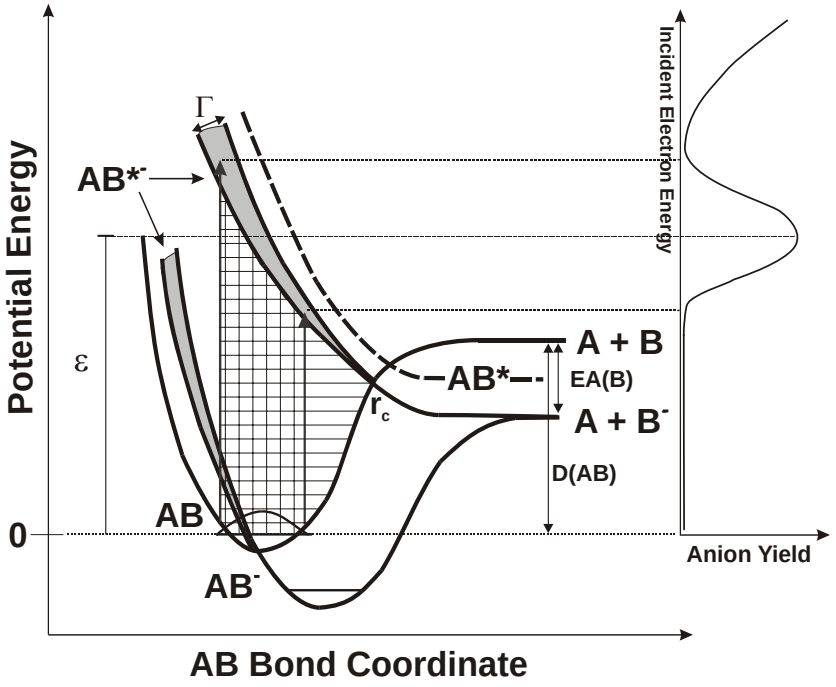

Figure 1.2 Diagram of potential energy surfaces that are involved with dissociative electron attachment. Upon excitation, the vertical lines represent the Franck-Condon region while the horizontal lines represent the region where electron autodetachment can occur.

The effects of the condensed phase on the DEA and TNI resonances have been studied and several aspects are well understood. Specifically, the DEA and TNI

resonances can be drastically altered due to third body interactions that open pathways for energy dissipation [7-10]. These interactions can have an effect during the lifetime of the TNI as well as alter products after the TNI dissociates. Most notably, dissociation from the low energy shape resonances is suppressed while dissociation from the Feshbach resonances can be enhanced by the surrounding medium. Although there is no detection of anions from the low energy shape resonance, dissociation could still occur where the products simply do not gain sufficient kinetic energy to escape the surface potential. Mechanisms for enhancement in dissociation can be explained by the effects of the medium on the electron autodetachment probability. One mechanism for dissociation enhancement through the Feshbach resonance is the lowering in energy of the anionic potential energy surface via the substrate and surrounding medium polarization interaction [11]. Due to the lowering of the ionic state potential, the wavepacket spends less time traversing the TNI potential, thus lowering the autodetachment probability. Another explanation for enhanced dissociation in the condensed phase is the more efficient conversion of an open channel resonance into a Feshbach resonance due to interactions with the medium [11]. An open channel resonance lies higher in energy than the Feshbach resonance and only requires a one electron transition to return to the associated neutral molecule compared to the two electron transitions needed for the Feshbach resonance. The electron autodetachment probability is higher for the one electron transition compared to the two, thus the Feshbach resonance is more probable to survive electron autodetachment and dissociate into a neutral and anionic fragment.

CHAPTER 2

CONDENSED SILICON TETRACHLORIDE FILMS ON SILICON(111)

2.1 Introduction

Low-energy electron interactions with molecular targets, condensed molecular solids, and adsorbates are of fundamental and technological importance. For example, the inelastic scattering of low energy electrons is important in i) the formation of planetary atmospheres [12, 13], ii) radiation damage of materials and biological systems [14, 15], iii) possibly the destruction of the ozone layer [16], and iv) electron beam based processing/ patterning strategies. In the latter case, low-energy electron interactions with molecules containing halogens are of particular concern since these molecules are often used in plasma and electron-beam processing of substrates and interfaces important in electronic devices and are regulated due to their negative impact on the environment. We have therefore studied silicon tetrachloride as the target molecule due to its frequent usage in halogen based plasma etching of silicon and is also relevant to understanding the details of Cl interactions with Si surfaces.

There have been a substantial number of experimental and theoretical studies on electron interactions with gas-phase $SiCl_4$. In summary, elastic integral cross-section calculations for electron collisions with $SiCl_4$ have been performed [17] which are in reasonable agreement in magnitude above 50 eV with measurements of the absolute total electron scattering cross-section from 0.3 eV – 4 keV [18]. Electron-impact ionization studies observing singly and doubly charged fragments revealed that dissociative

ionization is dominant from the low energy thresholds near 20 eV to 900 eV [19]. Concentrating on the low electron energy regime (0 – 40 eV), calculations of the integral elastic, differential elastic, and rotationally inelastic cross-sections were conducted [20]. These calculations are in reasonable agreement with experimental total cross-sections from electron transmission spectroscopy where structure in the 0 – 10 eV region was observed due to negative ion states [18, 21]. Dissociative electron attachment (DEA) resonances have also been observed in the Cl^- ion yield in the 0 – 10 eV region [22-24].

Few reports regarding electron or photon interactions with solid molecular silicon tetrachloride have been published. There have been photon-stimulated desorption (PSD) measurements of multilayer $SiCl_4$ films investigating cation fragment desorption from K-edge excitation [25, 26], as well as cation fragment desorption [27-29] and Cl^- desorption [30] from Si(2p) and Cl(2p) core level excitations. These high energy transitions populate antibonding and Rydberg levels that are relevant to low energy interactions with the molecular solid; however, the desorption mechanisms producing the ionized fragments involve deep core level Auger decay processes that do not occur in our low energy experiments. Other experiments at low coverages (1 – 2 monolayers) of $SiCl_4$ condensed on Si(100) have been conducted which include detection of $SiCl_x^+$ fragments and the coverage dependence of Cl^- and Cl^+ from ESD at 150 eV [31]. From additional experiments at monolayer coverages but low incident electron energies, structure in the Cl^- yield at 11 eV was attributed to DEA [32] which agrees with gas phase measurements near 10 eV [22-24].

2.2 Electronic Structure

In order to obtain a comprehensive understanding of the results presented in the next few chapters, a brief description of the electronic structure of condensed silicon tetrachloride is necessary. The ground state electronic configuration of an isolated silicon tetrachloride molecule is $(6a_1)^2(6t_2)^6(7a_1)^2(7t_2)^6(2e)^4(8t_2)^6(2t_1)^6$. From photoelectron [33, 34] and photoabsorption [35-37] measurements as well as multiple-scattering Xα and discrete variational Xα calculations [38-40], a general synopsis of the occupied and unoccupied molecular orbitals of $SiCl_4$ relevant to our experiments is illustrated in Figure 2.1. In this figure, the energy range derived from the available experimental and theoretical gas phase values are referenced to the vacuum level and listed on the left. The highest occupied levels are the $2t_1$ (12.1 eV), $8t_2$ (12.9 eV), and 2e (13.5 eV) non-bonding orbitals; the $7t_2$ (14.8 eV) and $7a_1$ (17.7 eV) bonding orbitals; and the $6t_2$ (25.1 eV) and $6a_1$ (26.7 eV) inner valence orbitals [40]. The unoccupied antibonding levels are designated as $9t_2$ (5.0 eV) and $8a_1$ (6.6 eV) and there are multiple levels between the $9t_2$ and the vacuum level which possess Rydberg character [39]. Experimentally, the $11t_2$ and $10t_2$ were assigned to the same transition [39]. The center portion of the figure contains a juxtaposition of the redrawn total electron yields from gas phase [33] and condensed phase [28] photoelectron experiments. As $SiCl_4$ condenses, the molecular orbital energy levels do not shift though there is broadening. Although broad and weak, the Rydberg along with the $9t_2$ and $8a_1$ valence transitions are preserved in solid $SiCl_4$ as indicated by Si 2p core-level photoabsorption; however, the transition to the 3e state does not survive [27, 28, 41].

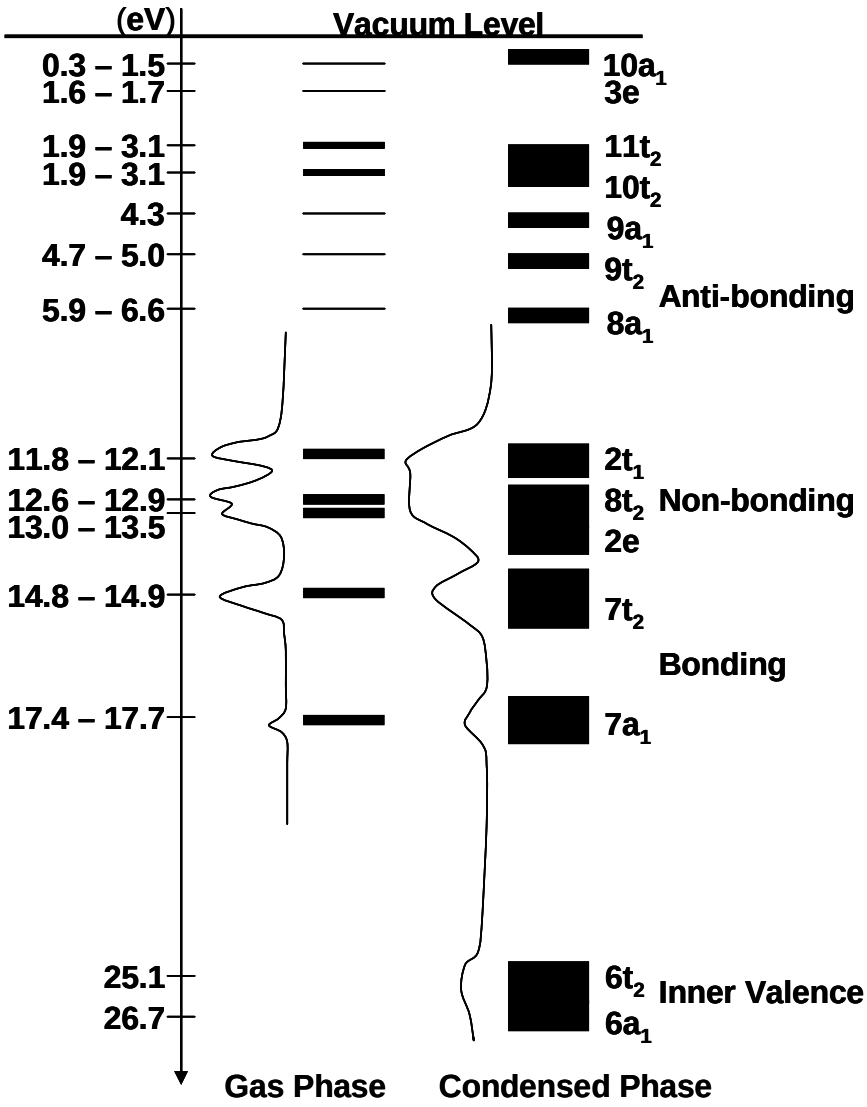

Figure 2.1 Schematic of the energy level diagram of $SiCl_4$ multilayers referenced to the vacuum level. The range of values on the left incorporate experimental and theoretical values from Tse *et al*. [39] for unoccupied levels, and averaged experimental data from Carlson *et al*. [33] and Green *et al*. [34] and theoretical values from Ishikawa *et al*. [40] for occupied levels. The $SiCl_4$ photoelectron data was traced from gas phase experiments by Carlson *et al*. [33] and condensed phase experiments by Chen *et al*. [28].

2.3 General Experimental Approach

The experimental set-up involves a custom designed ultra-high vacuum (UHV) chamber with a 3×10^{-10} Torr base pressure which is depicted in Figure 2.2. The substrate is the (111) face of a n-type silicon single crystal mounted to a liquid nitrogen cooled rotatable cryomount. The temperature of the silicon crystal can be varied from 110 – 1320 K via thermal contact with liquid nitrogen and resistive heating. The temperature is monitored with a type-K thermocouple shrouded in tantalum foil clipped to the front face of the substrate. The chamber is equipped with a quadrupole mass spectrometer (QMS) for temperature programmed desorption (TPD) analysis, a pulsed electron gun with a

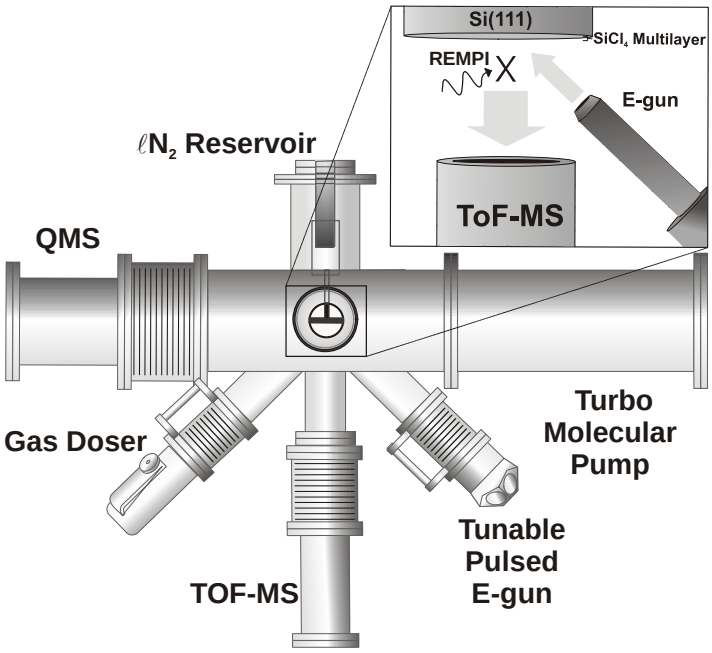

Figure 2.2 Depiction of the UHV chamber where experiments were performed. All cations and ionized neutrals are detected using the ToF-MS, and TPD experiments were conducted with the QMS. In the blow up, Cl($^2P_{3/2}$) and Cl($^2P_{1/2}$) REMPI and nonresonant Si and SiCl ionization occurs at **X**.

narrow energy dispersion oriented 45˚ relative to the silicon surface, and a time of flight mass spectrometer (ToF-MS). The ToF-MS is mounted directly below the substrate where intrinsic desorbing cations are detected, as well as neutrals ionized via resonance enhanced multi-photon ionization (REMPI).

In order to detect the neutral fragments, we routinely utilize REMPI/time-of-flight spectrometry [42-46]. A diagram of the ToF-MS and pulse sequence that we utilize is shown in more detail in Figure 2.3. Since we use a pulsed electron beam, varying the delay time between the electron-beam pulse and the focused laser beam allows us to map out a quantum resolved velocity distribution of the desorbing neutrals. Typically all desorbing ions are removed by an initial pulsed extraction field followed by ionization of the neutrals under constant field conditions. The detection sensitivities of this arrangement are ~10^6 atoms/quantum state/cm^3 [47].

In general, a plume of desorbates containing both neutrals and ions is created as a result of electron interactions with the target substrate. A negative potential extraction pulse is applied immediately after the electron beam pulse that extracts all cations from the sample region while neutral species are left in their desorbing trajectories with their initial kinetic energy. Detection of neutral desorbates can then be accomplished by focusing a tunable pulsed laser above and parallel to the surface region. To ionize the ground and excited state atomic chlorine species, the Cl($4p\ ^2D_{3/2} \leftarrow 3p\ ^2P_{3/2}$) at 235.336 nm and Cl($4p\ ^2P_{1/2} \leftarrow 3p\ ^2P_{1/2}$) at 235.205 nm (2 + 1) REMPI schemes were used, respectively [48, 49]. To create the photons for these transitions, we used the visible output of a Nd:YAG pumped Master Oscillator/Power Oscillator (MOPO) which is then doubled using a beta Barium Borate (β-BBO) crystal. Approximately 0.4 mJ/pulse of the

laser light was directed and focused to a point ~ 1 mm over the silicon substrate. To measure the neutral ESD yields as a function of incident electron energy the laser pulse was kept constant in time relative to the end of the electron pulse. A wide electron pulse

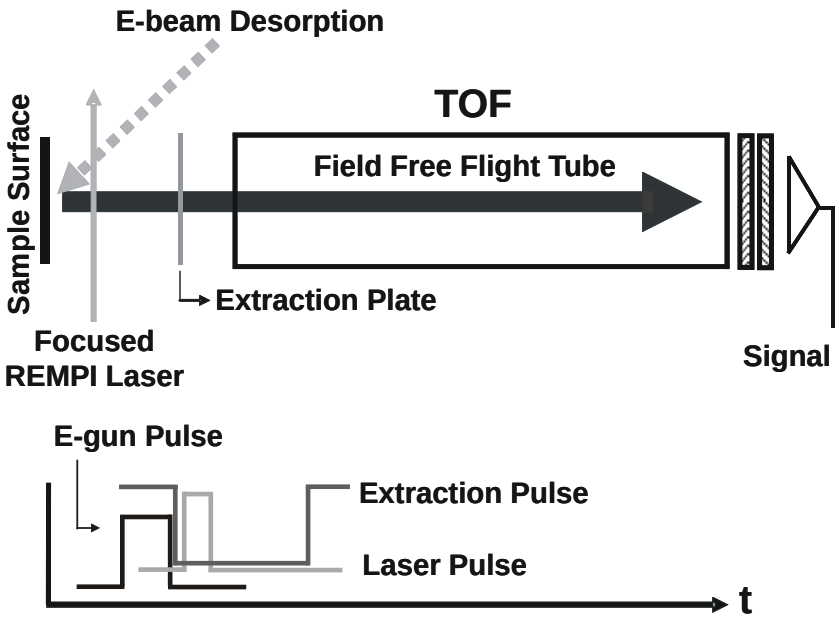

Figure 2.3 Diagram of the REMPI/ToF-MS experiment with the pulse sequence used for the detection of neutral species from electron stimulated processes on condensed molecular films. The pulsed nature of the experiment allows the measurement of quantum-resolved velocity distributions.

was used ensure all neutrals with variable velocities are present in the ionizing laser field. The velocity distributions of the neutrals were measured by delaying the laser pulse relative to the electron pulse. In this case, a narrow electron pulse was used to select neutrals with specific velocities to be ionized. The ESD yields of cations are measured without the presence of the laser pulse.

Before depositing $SiCl_4$ multilayers on the silicon substrate, liquid silicon tetrachloride (99.998% pure) was degassed using multiple freeze-pump-thaw cycles. The

silicon substrate was degassed followed by removal of the oxide layer. Prior to each dose of $SiCl_4$, the silicon surface was cleaned and annealed by multiple cooling-heating cycles which involved cooling to 120 K, slowly heating to 1300 K, re-cooling to 120 K, and then flash heating to 1100 K. These cycles annealed the Si(111) after $SiCl_2$ removal at [50-52] at 1100 K and minimized remnants of chemisorbed Cl atoms and background contaminants on the surface. Multilayers of $SiCl_4$ (~100 monolayers) were deposited by directionally dosing the vapor at 1.0×10^{-7} Torr for 15 min with a backing pressure of approximately 2 Torr. The sample temperature was kept below 110 K to achieve a sticking coefficient close to unity.

CHAPTER 3

ELECTRON-STIMULATED DESORPTION OF CATIONS FROM SILICON TETRACHLORIDE MULTILAYERS ADSORBED ON THE SILICON(111) SURFACE

3.1 Introduction

Though electron scattering [18, 19, 23, 39] and recently photodissociation with synchrotron radiation [53] has been studied with gas phase $SiCl_4$, relatively little information exists regarding electron scattering with condensed multilayers of this non-polar molecule. Work on the electron-stimulated desorption (ESD) of Cl^+ from $SiCl_4$ monolayers [31, 32] and photon-stimulated desorption (PSD) of cations from $SiCl_4$ multilayers [29, 30] have been reported. These previous studies [29-32] demonstrated that i) intermolecular multilayer adsorbate interactions are limited, ii) ESD from the monolayer regime was much more efficient and iii) the electronic structure does not change dramatically when comparing the gas and condensed phases. Despite the desorption measurements mentioned above, there have been no measurements of the threshold energies and branching ratios of all of the possible cationic products. This information is necessary for a detailed understanding of the states and mechanisms governing cationic ESD and PSD from $SiCl_4$ multilayers. In this chapter, a detailed study of the ESD of cations from multilayers of $SiCl_4$ adsorbed on Si(111) is reported. We concentrate on measurements of threshold energies and discuss the probable electronic processes governing ESD.

3.2 Experimental Details

In order to measure threshold values, ESD data of cations were taken by stepping the incident electron energy from 1 to 50 eV in 1 eV increments. Collection efficiency was maximized by grounding the substrate and applying a -255 V, 100 μs extraction pulse to the ToF-MS entrance grid immediately after the electron pulse. Due to the likely possibility of charge buildup in the $SiCl_4$ multilayer, low electron fluxes (3.64×10^{10} e^- /pulse cm^2) were maintained throughout the experiments by using 400 ns pulses at 500 Hz. The use of such short electron pulses minimized surface charging during the pulse and the frequency allowed complete discharging between pulses.

The temperature of the sample was variable from 110 – 1200 K and monitored using a type-K thermocouple clipped to the front face of the sample. TPD experiments were carried out using a heating rate of 1.5 K/s and the desorbing neutrals were detected with the ionizer/QMS assembly. Note that the TPD data was obtained in a multiplex mode which allowed simultaneous monitoring of several masses.

3.3 Results

3.3.1 TPD and coverage measurements

An example of the TPD spectra used to determine the multilayer coverage is shown in Figure 3.1. The filled circles in the figure and the inset represent the data obtained from the Si^+ ion which is from the cracking of $SiCl_4$(g) in the QMS ionizer. The

inset figure demonstrates the multilayer and the monolayer desorption of $SiCl_4$ in the low coverage regime. The solid and dashed lines are fits to the multilayer and monolayer

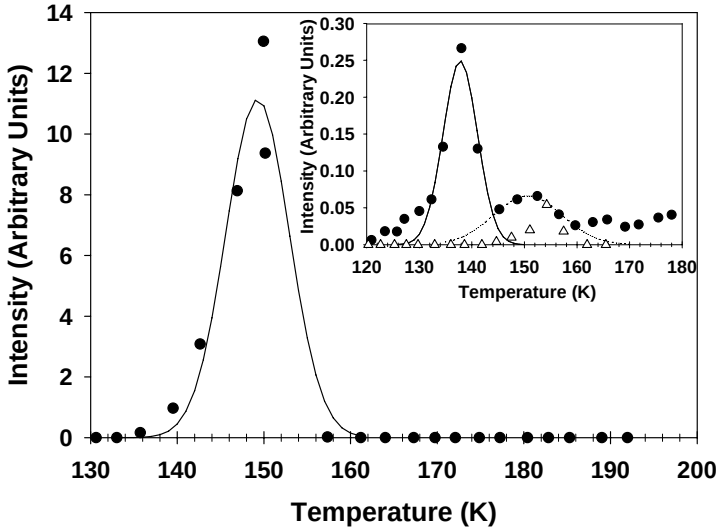

Figure 3.1 Temperature programmed desorption (TPD) spectra of $SiCl_4$ adsorbed on a Si(111) substrate taken in a multiplex mode which allowed simultaneous monitoring of several masses. The filled circles in the figure represent data obtained using the Si^+ ion produced from cracking of $SiCl_x(g)$ in the QMS ionizer. This provides a convenient signature of $SiCl_4$ desorption. The open triangles (inset) represent the signal from the $SiCl_4^+$ parent ion peak indicating molecular adsorption. The $SiCl_4^+$ and Si^+ features near 150 K in the inset are from the desorption of the monolayer in the low coverage regime. The solid and dashed lines are fits to the multilayer and monolayer desorption features, respectively.

desorption features, respectively. The open triangles within the inset represent the signal from the $SiCl_4^+$ parent ion peak indicating molecular adsorption. The $SiCl_4^+$ and Si^+ features near 150 K in the inset are from the desorption of the monolayer in the low coverage regime. The multilayer feature for high coverage is shown in the main figure and is peaked at 148 K. The low coverage multilayer peak shown in the inset is peaked at 138 K. The shift of the leading edge to higher temperature (relative to the onset of the multilayer feature in the inset) is indicative of zero order desorption kinetics which is

typical for desorption of weakly interacting overlayers. The overall coverage which the experiments were carried out was ~100 ML. This was determined by integrating the multilayer desorption peak then dividing that value by the area under the monolayer peak. At such thicknesses, substrate effects are minimized and only condensed $SiCl_4$ intermolecular interactions need to be considered.

3.3.2 Threshold data

Figure 3.2 illustrates the yields of electron-stimulated desorption products (cations) as a function of the incident electron energy. In Frame A, the dominant product is Cl^+ (filled circles) and the yield has been divided by a factor of six compared to the other ions including Si^+ (filled triangles), $SiCl^+$(empty triangles), $SiCl_2^+$ (filled squares), and $SiCl_3^+$ (empty diamonds). It can be seen that there is structure in the Cl^+ data which is not present or apparent in any of the other channels.

Over this incident electron energy range, $SiCl^+$ and $SiCl_3^+$ have comparable yields whereas the $SiCl_2^+$ and Si^+ yields are smaller relative to the other ions. In addition, there appears to be a distinct threshold for these sets of products. At ~17 eV, Cl^+ and $SiCl_3^+$ are the only observable ions. This is true until 24 – 25 eV where Si^+, $SiCl^+$, and $SiCl_2^+$ begin to desorb. To clearly show the two distinct desorption thresholds which are represented in Frame B of Figure 3.2, the $SiCl_3^+$ yield was normalized to the Cl^+ yield and the Si^+ and $SiCl_2^+$ yields were normalized to the $SiCl^+$ yield. This normalization procedure clearly delineates the difference between groups of ions that desorb at each threshold and assists in the assignments of the different ESD mechanisms.

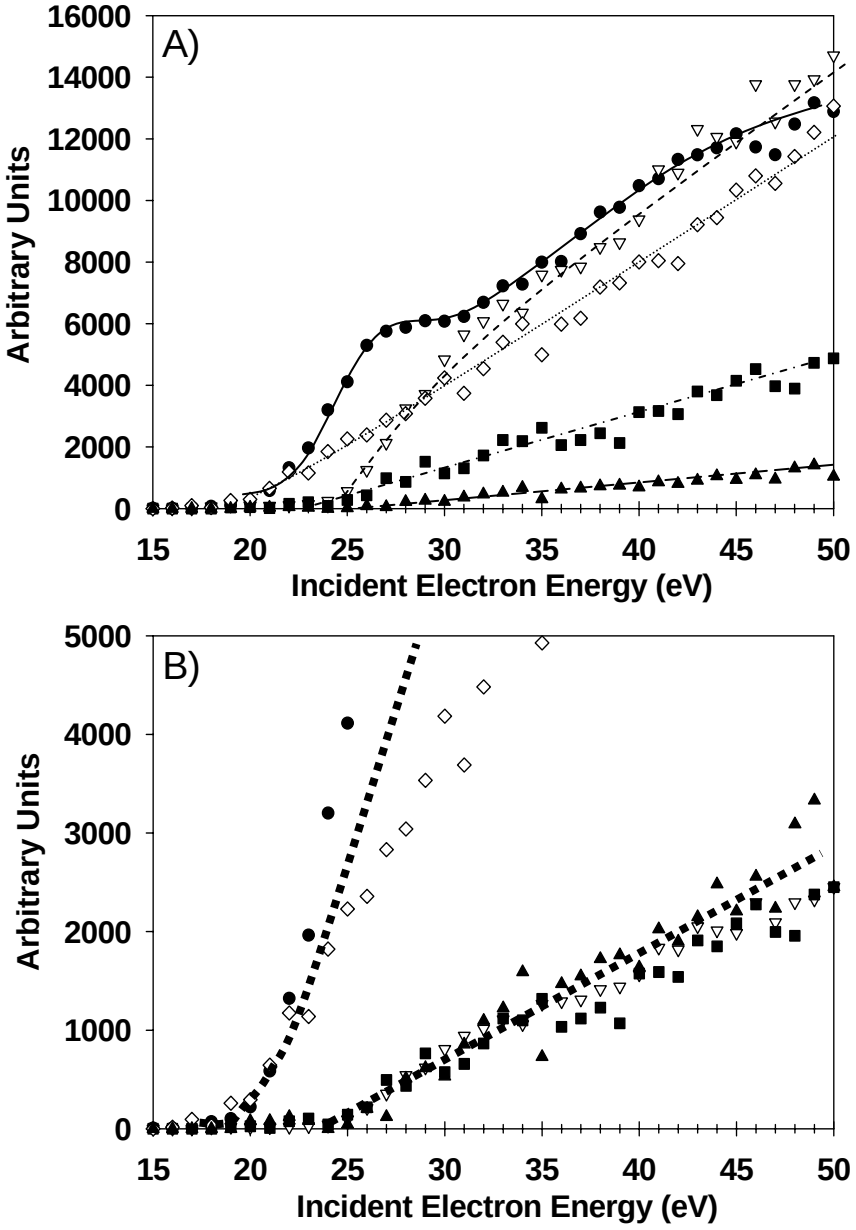

Figure 3.2 Frame A: ESD cation yields as a function of incident electron energy. In both plots, cations are represented as follows: Si^+ (▲), Cl^+ (●), $SiCl^+$ (▽), $SiCl_2^+$ (■), $SiCl_3^+$ (◇). Note the Cl^+ ion yield was divided by a factor of six. Frame B: A more detailed view of the threshold region. Note the $SiCl_3^+$ was normalized to the Cl^+ yield while Si^+ and $SiCl_2^+$ were normalized to $SiCl^+$. This delineates the separation of cations into the two distinct threshold regions. All lines were added to guide the eye.

The Cl^+ and $SiCl_3^+$ ions desorb at 17 eV while Si^+, $SiCl^+$, and $SiCl_2^+$ desorb at 24 - 25eV. Similar to condensed phase, ion thresholds from photoionization and electron scattering of $SiCl_4$(g) occur in this incident electron energy range along with structure in the dominant channel around 25 eV. In the gas-phase, $SiCl_4^+$, doubly charged ions, and molecular chlorine ions are observed. [19, 54] None of these products have been observed in stimulated desorption studies of $SiCl_4$ monolayer or multilayers [30, 32]. The disappearance of these ion channels in desorption studies is not surprising since the departing ions must gain sufficient energy to overcome many body interactions, high trapping probability, and electron-ion recombination. This typically requires Coulomb repulsions and multi-hole states.

3.4 Discussion

3.4.1 Low-energy threshold

According to Figure 2.1, the 17 eV threshold for Cl^+ and $SiCl_3^+$ ESD can be formed by direct ionization from the $7t_2$ and $7a_1$ bonding levels. A localized hole produced in the Si-Cl bond from direct ionization from the $7t_2$ and $7a_1$ bonding levels can produce a highly excited state that can decay into either $SiCl_3$ + Cl^+ or $SiCl_3^+$ + Cl. This is shown schematically in Figure 3.3 and as mechanism 1 in Figure 3.4. The production of two-hole states and Auger processes are less likely at 17 eV than direct single particle excitations. We have also observed that the yield of Cl^+ and the overall slope of this product is much larger

than the yield and slope of $SiCl_3^+$. This could be due to the dominance of Si-Cl bonds at the vacuum surface interface and a higher velocity and overall escape probability for Cl^+.

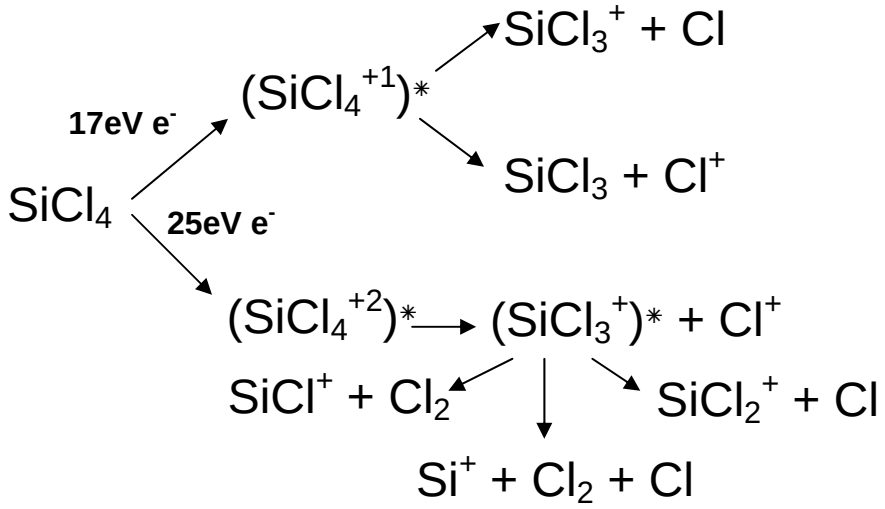

Figure 3.3 Possible low and high energy decomposition pathways of single and doubly ionized $SiCl_4$. * indicates possible internal energy

3.4.2 Resonance structure

The Cl^+ curve increases to 25 - 26 eV then begins to level off as shown in Frame A of Figure 3.2. This feature can be explained by direct transitions to the antibonding $9t_2$ and $8a_1$ levels from the $6t_2$ and $6a_1$ levels. These are resonant transitions with an expected onset energy of ~22 eV, a peak transition probability around 25 - 26 eV, as observed. The yield then levels at 32 eV since the transitions are no longer resonant. Since the $9t_2$ and $8a_1$ excited states are dissociative and holes in the deep $6t_2$ and $6a_1$ levels can be filled by Auger processes, these transitions should produce Cl^+ directly, but with a resonant structure. This produces a 2-hole, 1-electron state that is shown as

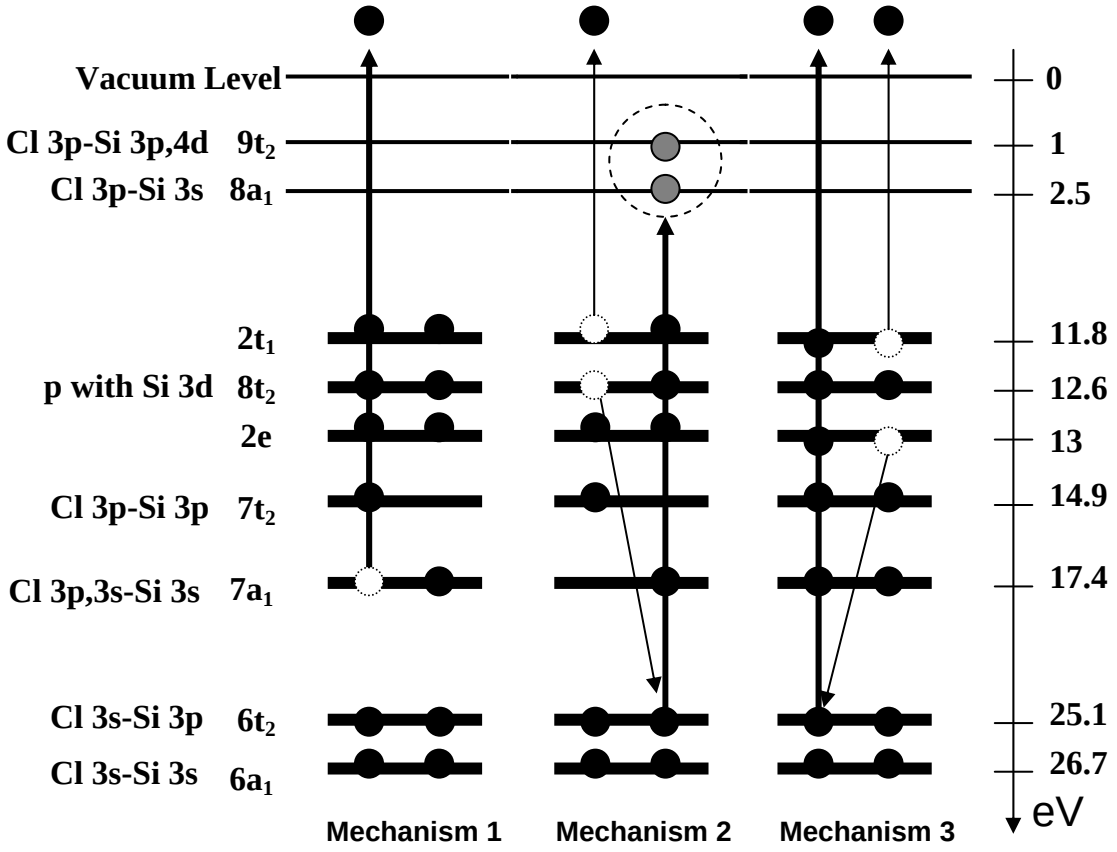

Figure 3.4 Illustration of potential electronic desorption mechanisms. Mechanism 1 and 2 demonstrate direct ionization from the $7a_1$ level into the vacuum as well as the creation of a dissociative excited state from the $6t_2$ level. These direct excitation mechanisms explain the low energy threshold and the resonance structure in the Cl^+ ion yield, respectively. Mechanism 3 demonstrates an example of a 2-hole state created by Auger decay. Note there are several possible 2-hole and 2-hole, 1-electron states that can be produced in the high energy threshold region.

mechanism 2 in Figure 3.4. It is also very similar to some states implicated in the ESD of Cl^+ from Si(100) and Si(111) [55-59]. We observe the resonant structure mainly in the Cl^+ yield curve, with little evidence of structure in the other channels.

3.4.3 High-energy threshold

The thresholds for the other ESD products, (i.e. Si^+, $SiCl^+$, and $SiCl_2^+$) all appear at an incident electron energy of ~25 eV. This energy is correlated with direct ionization from the $6t_2$ and $6a_2$ inner valence molecular orbitals. These can Auger decay and produce several different 2-hole states. The most plausible Auger processes may proceed by a 25 eV incident electron producing a hole in the $6t_2$ or $6a_1$ inner valence levels, which induces a shake off from the $8t_2$ orbital then ejection of an adjacent electron in the $8t_2$ or $2t_1$ levels. $SiCl^+$, $SiCl_2^+$, and Si^+ ions can then be produced via Coulomb explosion of the doubly ionized parent $SiCl_4^{+2}$. This is shown as mechanism three in Figure 3.4. As the incident electron energy is increased to 50 eV, all ESD cations increase steadily because of an overall increase in the ionization cross section and an increased contribution of multi-electron excitations.

These complicated multielectron transitions could also involve the production of Cl^+ and vibrationally excited $SiCl_3^+$. The latter species can then undergo unimolecular decomposition forming the Si bearing ions as already discussed. The relative signal intensities may also be governed by the favorable energetics associated with a molecular elimination step forming Cl_2. This could explain the relatively large signal strength of $SiCl^+$ compared to Si^+ and $SiCl_2^+$. These reaction pathways are depicted in Figure 3.3.

3.5 Conclusion

Low energy (5 - 50 eV) electron stimulated desorption of Si^+, Cl^+, $SiCl^+$, $SiCl_2^+$, and $SiCl_3^+$ has been observed from multilayers of $SiCl_4$ adsorbed on a Si(111) surface. Two threshold energies are observed in the cation yields as well as resonance structure in the Cl^+ yield. The low energy threshold at 17 eV that produces Cl^+ and $SiCl_3^+$ can be assigned to direct ionization of the $7t_2$ and $7a_1$ bonding orbitals and possible unimolecular decay of the resulting highly excited parent ion. The resonant structure between 22 - 32 eV can be associated with resonant transitions from the $6t_2$, $6a_1$ to the antibonding $8a_1$ or $9t_2$ levels followed by Auger decay. The threshold near 25 eV was observed for all other ESD products (i.e. Si^+, $SiCl^+$, and $SiCl_2^+$). We tentatively correlate this threshold with direct ionization of the $6t_2$ and $6a_1$ levels which then decay to form several 2-hole states. All resultant 2-hole, 1-electron final states Coulomb explode yielding primarily Cl^+ desorption.

CHAPTER 4

LOW-ENERGY ELECTRON-STIMULATED DESORPTION OF NEUTRALS FROM MULTILAYERS OF SILICON TETRACHLORIDE ON THE SILICON(111) SURFACE

4.1 Introduction

In the case of condensed $SiCl_4$, the desorbing ions produced by low-energy electrons must escape charge transfer to neighbors in the molecular solid, the surface potential, and reactive scattering processes. These channels produce neutral species which may have enough kinetic energy to leave the surface. Although the neutral yields resulting from low-energy electron induced processes can be complicated due to multiple decay mechanisms, neutral detection is necessary to fully understand the desorption process [5]. Single-photon ionization [60] and REMPI [61] have been used to detect neutrals desorbed during the etching of Si(100) by molecular Cl_2. To date there have been no studies that concentrate on the ESD of neutral species from multilayers or monolayers of adsorbed silicon tetrachloride.

4.2 Experimental Details

Using the experimental setup described in Chapter 2, time of flight distributions and yields versus incident electron energy measurements were performed to provide information concerning the production and decay mechanisms of excited parent states. Time of flight distributions of the desorbing neutrals were taken by delaying the laser

pulse relative to the falling edge of the electron pulse. To record the velocity distribution, the electron pulse (200 ns) and the laser step increments (200 ns) were kept as small as possible while still obtaining a measurable amount of ions. In order to measure threshold values, ESD data were taken by stepping the incident electron energy from 1 to 50 eV in 1 eV increments while maintaining a constant electron pulse to laser pulse delay of 200 ns. To integrate over the entire velocity distribution, 15 μs electron pulse widths were used. All data points correspond to the integrated area below each specific mass peak, except the chlorine data, which are represented by only the 35 amu isotope.

Due to the possibility of charge buildup in the $SiCl_4$ multilayer during these experiments, low electron fluxes (time averaged 7.29×10^{8} and 5.47×10^{10} $e^-/s\ cm^2$) were used during velocity distribution and threshold measurements, respectively. The use of short electron pulses minimized surface charging during the pulse and the frequency (20 Hz) allowed discharging between pulses.

4.3 Results

4.3.1 Incident electron energy dependence

Our measured neutral $Cl(^2P_{3/2})$ and $Cl(^2P_{1/2})$ yields are presented versus incident electron energy (1 – 50 eV) in Figure 4.1. To demonstrate that there is essentially no nonresonant ionization of neutral chlorine, the off resonance neutral chlorine yield is also plotted. This measurement was taken when the photon energy was between the ground and excited chlorine REMPI transitions; i.e. at 235.270 nm. For the sake of comparison,

the y-axes were offset, and the Cl($^2P_{1/2}$) yield was normalized to the Cl($^2P_{3/2}$) yield at 50 eV by a multiplying factor of 5.8.

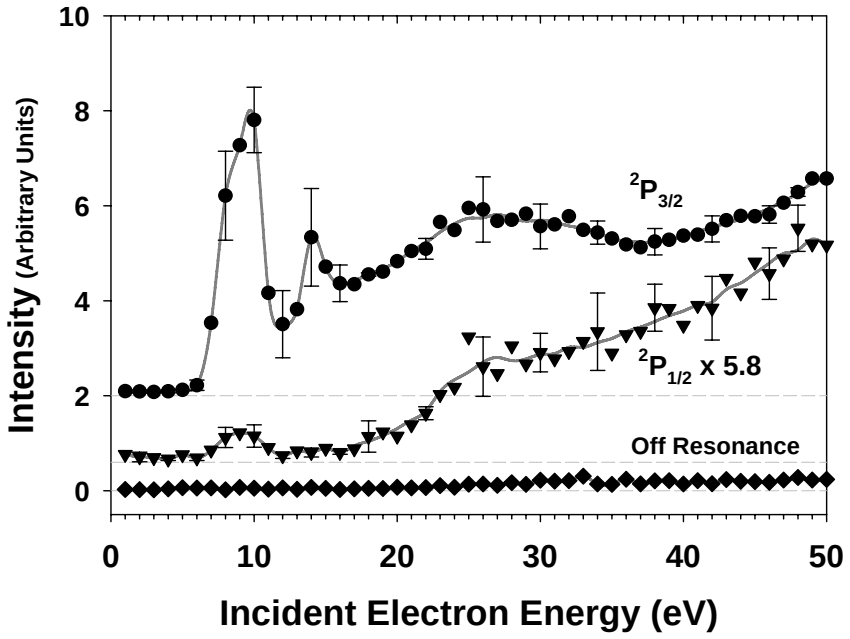

Figure 4.1 Plot of neutral atomic chlorine yields Cl($^2P_{3/2}$)(●), Cl($^2P_{1/2}$)(▼), and chlorine from an off resonance wavelength(◆) versus incident electron energy. The zeros shown by grey dashed lines have been offset for comparison. Error bars verify the structure and the grey solid lines guide the eye.

There is a considerable amount of neutral atomic chlorine in the ground $^2P_{3/2}$ state, as well as, a measurable amount of spin-orbit excited $^2P_{1/2}$ chlorine desorbing due to electron impact of condensed $SiCl_4$ multilayers. The ground state Cl($^2P_{3/2}$) data contains two sharp features at 10 and 14 eV with a broad feature from approximately 22 to 32 eV. Cl($^2P_{3/2}$) has an appearance threshold at 6 – 7 eV from which there is a monotonic increase of the baseline upon which the 10 and 14 eV features are superimposed. The Cl($^2P_{1/2}$) plot has similar features at 7 – 11 eV, as well as a broad

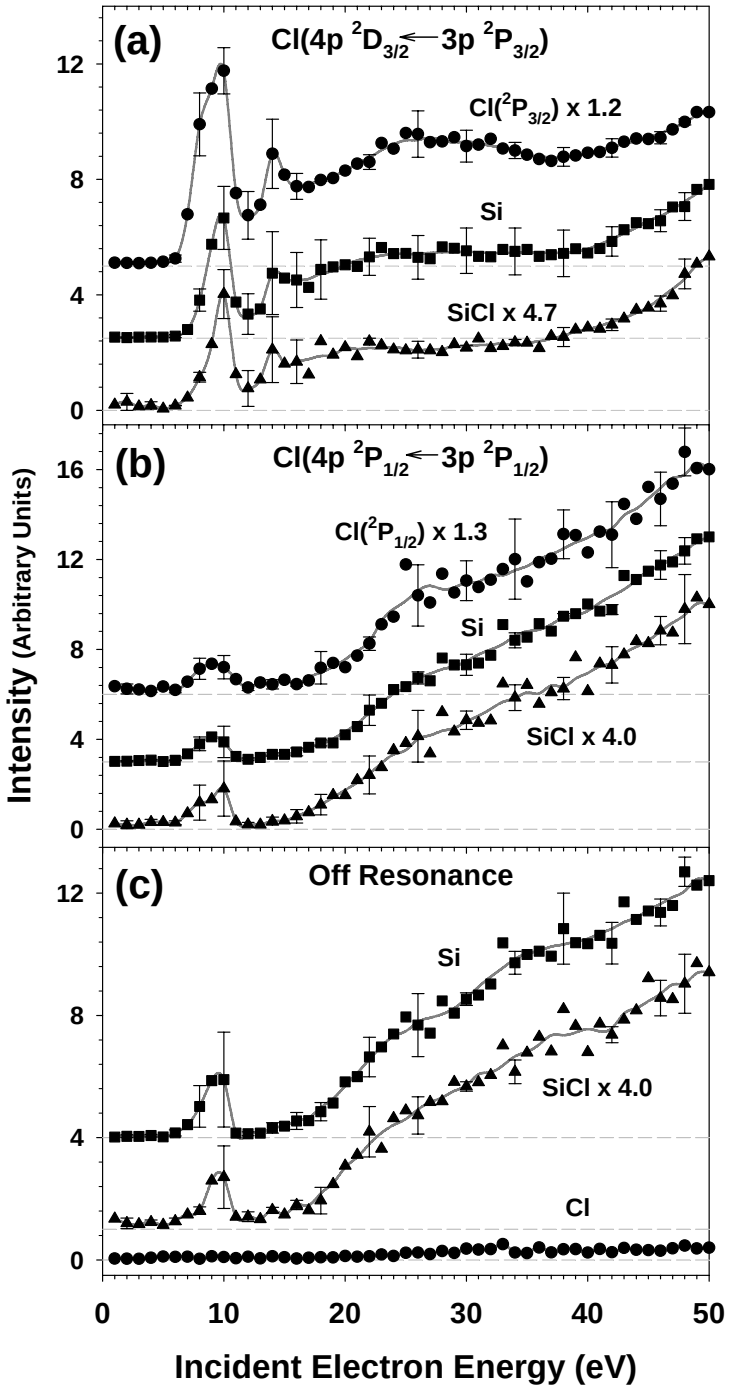

Figure 4.2 Plots of the neutral yields of Cl(●), Si(■), and SiCl(▲) versus incident electron energy. The data was taken utilizing (a) the Cl(4p $^2D_{3/2}$ ← 3p $^2P_{3/2}$) REMPI transition, (b) the Cl(4p $^2P_{1/2}$ ← 3p $^2P_{1/2}$) REMPI transition, and (c) an off resonance excitation. The zeros shown by horizontal grey dashed lines have been offset for comparison. Error bars of selected data points verify the structure and the grey solid lines guide the eye. Plots are normalized at 50 eV with the multiplicative normalization constant labeled.

feature from 23 to 27 eV. Although the $Cl(^2P_{1/2})$ is normalized for relative comparison, the total yield is an order of magnitude smaller in the low energy region, and there is not a detectable feature at 14 eV.

Silicon and silicon chloride ions are also produced nonresonantly due to the presence of the laser. This nonresonant ionization is compared to the resonant ionization of $Cl(^2P_{3/2})$ and $Cl(^2P_{1/2})$ in Figures 4.2(a) and 4.2(b), respectively. Figure 4.2(c) illustrates neutral yields when the photon energy is not resonant with any transition of Cl, Si, or SiCl. All spectra are normalized to the silicon data (the largest yield at 50 eV) in each section with the normalization multiplicative factor indicated. There are many important aspects to note. First, the 10 eV feature is present for all products except for off resonant atomic chlorine. Second, when the photon energy is in resonance with the $^2D_{3/2}$ intermediate state in (Figure 4.2(a)), there is an enhancement of the 10 eV feature, appearance of the 14 eV feature, and a general rise in yield intensity for $Cl(^2P_{3/2})$, Si and SiCl at all incident electron energies compared to product yields in Figure 4.2(b) and 4.2(c). Third, the magnitudes of the 10 eV feature of Si and SiCl in the off resonance plot (Figure 4.2(c)) are comparable to the magnitudes of the same feature when the photon energy is in resonance with the $^2P_{1/2}$ intermediate state (Figure 4.2(b)). Not only is this feature comparable, but the overall incident electron energy dependent desorption structures from 0 – 50 eV are similar. Finally, no other $SiCl_x$ species were observed other than silicon and silicon chloride.

4.3.2 Time of flight distributions

In order to determine possible mechanisms and to gain an understanding of the origin of these neutral species, relative time of flight distributions were taken at specific incident electron energies and fit to the Maxwell-Boltzmann expression below:

$$I(t) = C_1 t^{-3} \exp\left(-\frac{m}{2kT_1}\frac{d^2}{t^2}\right) + C_2 t^{-3} \exp\left(-\frac{m}{2kT_2}\frac{d^2}{t^2}\right) \qquad (4.1)$$

The fitting procedure to the Maxwell-Boltzmann expression has been previously described [62]. Briefly, multiple components are fit to the time of flight data where C_1 and C_2 are proportionality constants, m is the mass of the desorbing neutral fragment, d is the distance from the surface to the laser beam, T_1 and T_2 are effective temperatures, k is the Boltzmann constant, and t is the delay time between the electron and the laser beams.

Figure 4.3 contains the ground state Cl($^2P_{3/2}$) distribution data at 10 eV (top) and 25 and 50 eV (bottom). Figure 4.4 contains the excited state Cl($^2P_{1/2}$) distribution data at 50 eV (top) and an average of the Si ToF distribution (bottom) at 10, 25, and 50 eV. In both figures, the dotted lines represent the thermal Maxwell-Boltzmann distribution with an effective temperature of 110 K. The short dashed and dashed/dotted lines represent the highly energetic nonthermal component and a nonthermal intermediate component, respectively. As discussed in more detail below, the long dashed lines in the Cl($^2P_{3/2}$) and the Si distribution of Figure 4.3 and 4.4 refer to a thermal distribution arising from

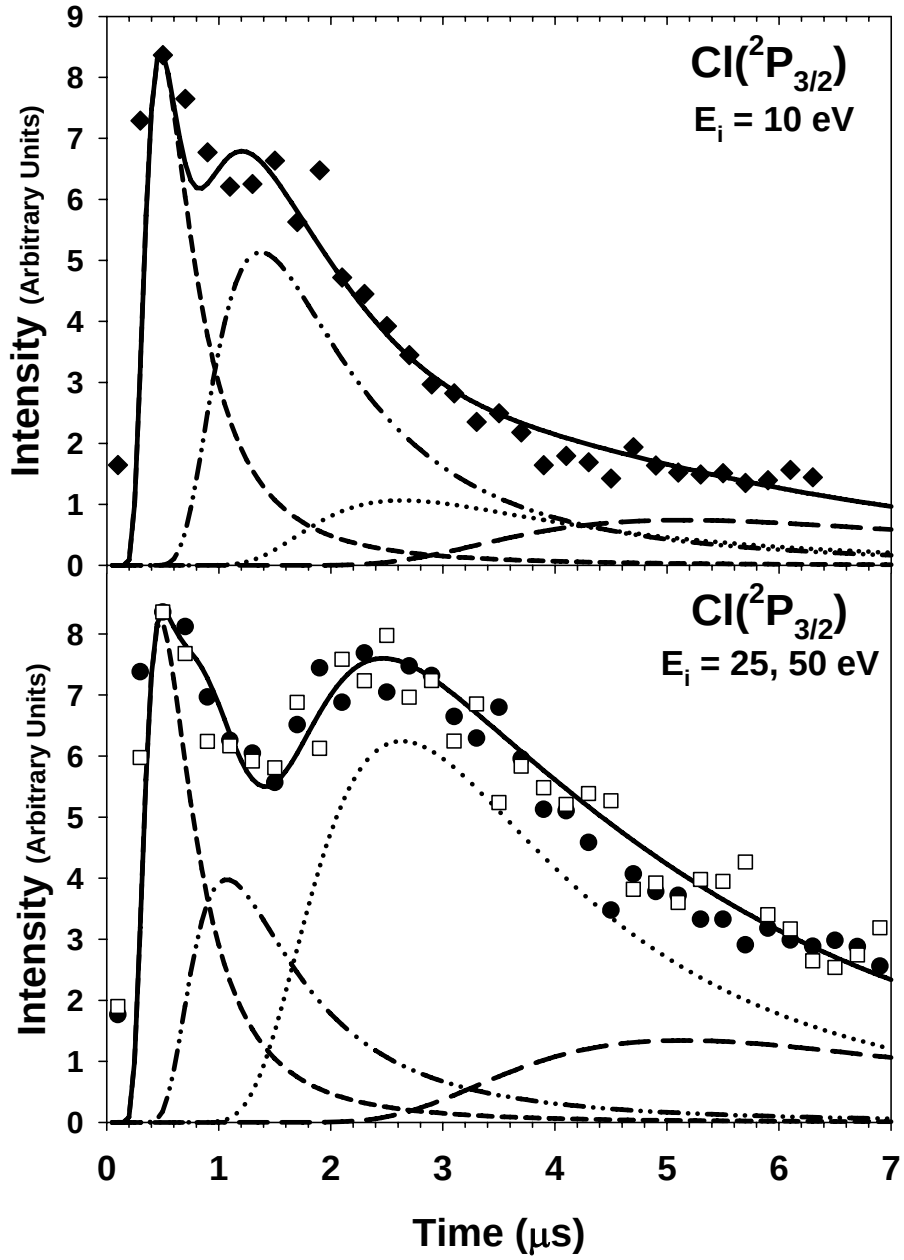

Figure 4.3 Summation of multiple Maxwell-Boltzmann distributions (solid line) fit to $Cl(^2P_{3/2})$ ToF data taken at 10 eV(◆) (top) and 25(□) and 50 eV(●) (bottom). The dotted lines represent the thermal Maxwell-Boltzmann with an effective temperature of 110 K. The short dashed and dashed/dotted lines represent the highly energetic nonthermal component and a nonthermal intermediate component, respectively. The long dashed lines are representative of possible contributions from photodissociated $SiCl_x$ precursors. In this fit, $SiCl_3$ at 110 K was used.

dissociation of $SiCl_x$ precursors. It is evident that the $Cl(^2P_{3/2})$ distributions at 25 and 50 eV overlap and are bimodal with a narrow, fast peak at 0.5 μs and a broad, slow peak at ~ 2.4 μs. However, the chlorine distribution at 10 eV does not have the same structure that is seen in the 25 and 50 eV plots. Rather, this ToF distribution is dominated by the fast peak with a much smaller contribution from a slow component. Both plots in Figure 4.3 contain identical energetic nonthermal components with a relative translational kinetic energy of ~425 meV corresponding to an effective temperature of 3287 K. The $Cl(^2P_{3/2})$ distribution from 10 eV contains a contribution from an intermediate component at 405 K (~52 meV). The intermediate component for the 25 and 50 eV distribution contributes less but is faster with an effective temperature of 665 K (~86 meV). Both distributions contain thermal components at 110 K (~14 meV) and this thermal component contributes approximately four times more to the total distribution at 25 and 50 eV, relative to 10 eV.

In the top portion of Figure 4.4, the $Cl(^2P_{1/2})$ distribution can be fit using three Maxwell-Boltzmann distributions. However, this time of flight distribution is mostly composed of nonthermal components. The effective temperature of the highly energetic nonthermal component is 4700 K having a kinetic energy of ~608 meV, the intermediate component is 800 K (~103 meV), and the thermal component is 110 K (~14 meV). When comparing the highly energetic nonthermal components of $Cl(^2P_{3/2})$ and $Cl(^2P_{1/2})$, the $Cl(^2P_{1/2})$ has a higher kinetic energy. Since the Si ToF distributions are independent of incident electron energy, the average of the nonresonant silicon data at 10, 25, and 50 eV is plotted in the bottom portion of Figure 4.4. The silicon distribution is fit using three Maxwell-Boltzmann distributions with a broad single peak at ~1.5 μs. The

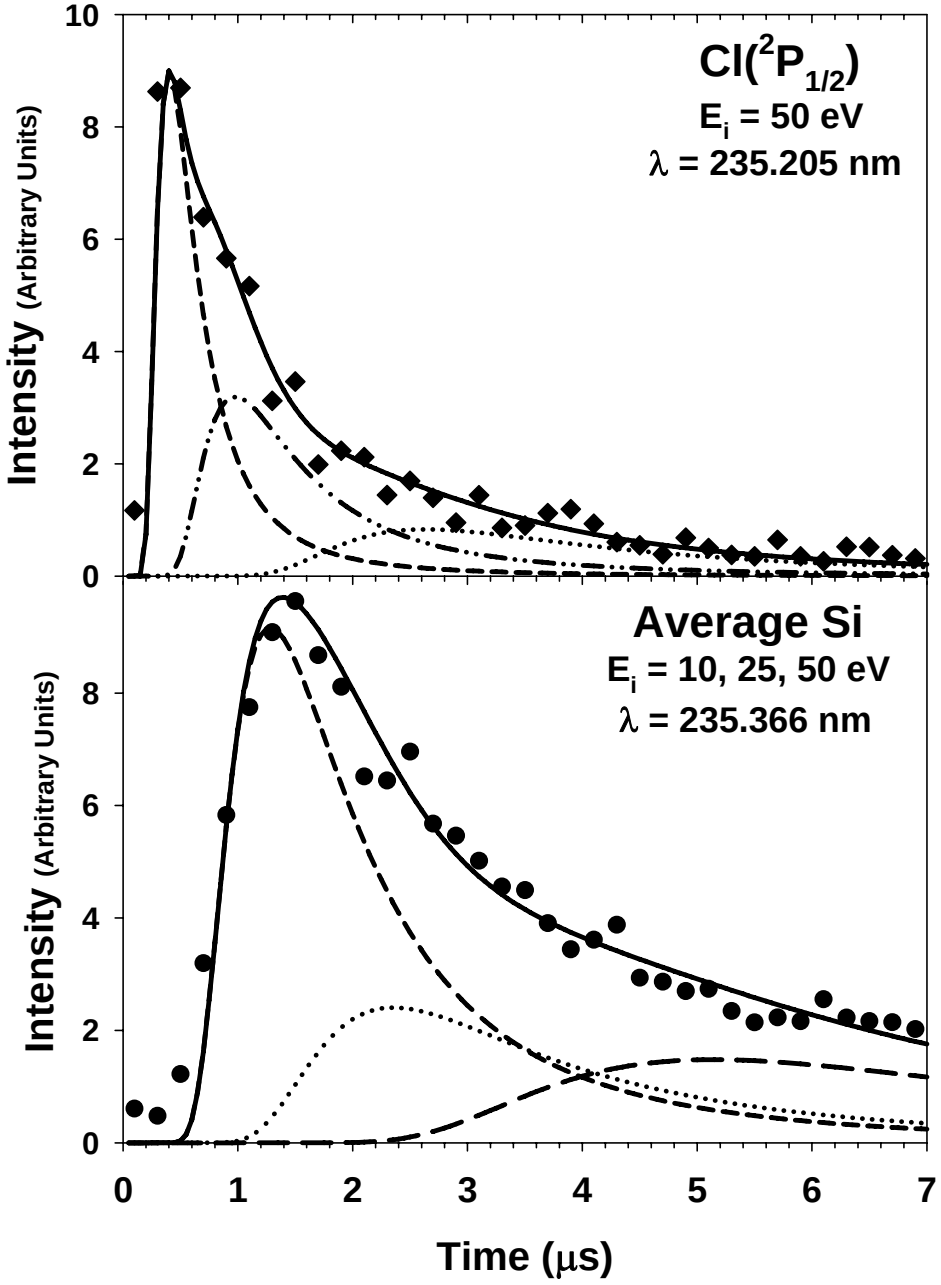

Figure 4.4 Summation of multiple Maxwell-Boltzmann distributions (solid line) fit to $Cl(^2P_{1/2})$ ToF data taken at 50 eV(◆) (top), and an average of nonresonant Si ToF data taken at 10, 25, and 50 eV(●) (bottom). The dotted lines represent the thermal Maxwell-Boltzmann distribution with an effective temperature of 110 K. The dashed and dashed/dotted lines represent the highly energetic nonthermal component and a nonthermal intermediate component, respectively. The long dashed line is representative of possible contributions from photodissociated $SiCl_x$ precursors. In this fit, $SiCl_3$ at 110 K was used.

nonthermal component corresponds to an effective temperature of 370 K with a kinetic energy of ~47 meV, and again the thermal component is 110 K, ~14 meV. Surprisingly, the kinetic energy of the nonthermal $Cl(^2P_{3/2})$ and $Cl(^2P_{1/2})$ components is an order of magnitude hotter than the nonthermal Si component.

The data in Figures 4.3 and 4.4 were fit to the minimal number of components needed to adequately fit the short flight time region; however, at long flight times, the thermal distribution (dotted line) of $Cl(^2P_{3/2})$ and Si did not adequately match the data. This could be due to an asymmetric detection efficiency of off normal desorption trajectories and complicated interactions with phonons of the molecular solid. In addition, heavy $SiCl_x$ precursors that first photodissociate then are either resonantly or nonresonantly ionized in the laser field can contribute to the Cl or Si ToF distribution, respectively. This would result in two aspects affecting the ToF distributions: 1) If these precursors desorb nonthermally, the Cl and Si fragments can contribute to the intermediate components of the Cl distributions and the nonthermal Si distribution. 2) If the precursors desorb with a thermal kinetic energy prior to photodissociation, this would explain the enlarged Cl and Si yields at long flight times. The formation of possible $SiCl_x$ precursors is thoroughly discussed below. Although the specific precursor identity, desorption kinetic energy, and dissociation branching ratios are unknown, a Maxwell-Boltzmann distribution of $SiCl_3$ at 110 K (long dashed lines) was added to the $Cl(^2P_{3/2})$ and Si ToF distributions to demonstrate the good fit and the likelihood of this mechanism. It is interesting to note that there are no contributions to the $Cl(^2P_{1/2})$ yield at long flight times which could indicate that the excited spin-orbit state of Cl is not produced from the photodissociation of $SiCl_x$.

4.4 Discussion

4.4.1 Structure in ESD yields vs. electron energy

4.4.1.1 Feature at 10 eV

There is significant structure in the ESD yield of $Cl(^2P_{3/2})$, $Cl(^2P_{1/2})$ as well as Si and SiCl centered at 9 - 10 eV which is below the ionization potential of $SiCl_4$ (12.1 eV). Below we describe several mechanisms that can give rise to this interesting structure. DEA can occur when the incoming incident electron interacts inelastically with either the $2t_1$, $8t_2$, and 2e molecular orbitals thereby promoting an electron to a Rydberg level, or electron interaction with the $7t_2$ promoting an electron to the antibonding $9t_2$ orbital or $9a_1$ Rydberg level. The original incident electron can then be temporarily trapped in the antibonding or mixed valence/Rydberg levels, creating a core-excited negative ion resonance. These are formally one hole, two electron Feshbach resonances. These resonances and a qualitative representation of the potentials involved in the electron-interactions with $SiCl_4$ for energies below the ionization potential are shown in Figure 4.5.

As previously mentioned, resonances near 10 eV have been observed in electron scattering cross-section measurements [18] and electron impact measurements while monitoring atomic chlorine anions in both gas phase [22-24] and monolayer coverages of $SiCl_4$ on Si(100) [32]. If the $SiCl_4^-$ transient negative ion escapes autodetachment, it

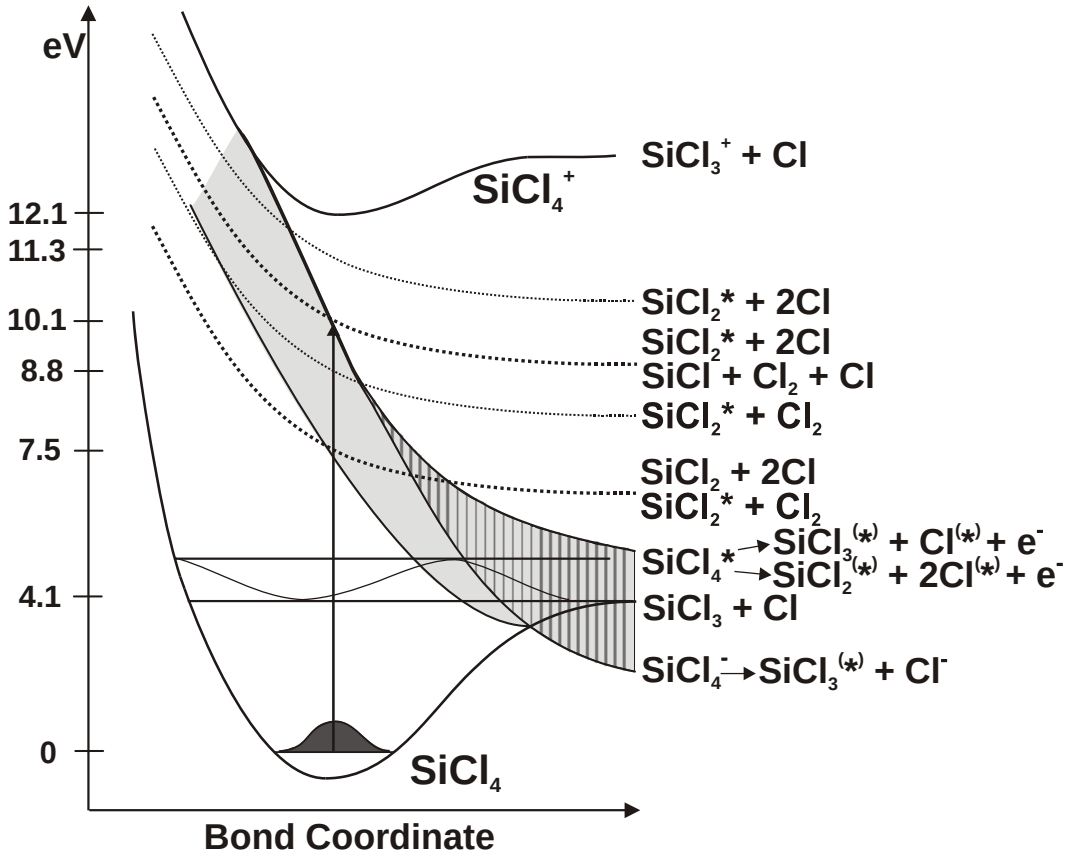

Figure 4.5 Qualitative potential energy diagram of states available below the ionization potential of $SiCl_4$. The light grey shaded area is the region where autodetachment of the Feshbach resonances occur. The light grey area with vertical lines represents dissociative excitonic states produced from autodetachment. Potential energies for dissociative states and the identities of fragment products have been reported (Refs. [63-65]).

dissociates into $SiCl_3^{(*)}$ and Cl^-. In the gas phase, Moylan *et al*. [23] demonstrated that only Cl^- was produced from DEA with no structure in the $SiCl_3^-$ yield. Though DEA resonances are generally preserved at surfaces of molecular solids, the importance of many body interactions and autodetachment can be enhanced in the condensed phase.

Following DEA, the chlorine anion can retain much of the energy gained from the repulsive force in the excited state. This excited anion can then undergo autodetachment or charge transfer to the surrounding medium before desorbing as a neutral chlorine atom. If chlorine atoms desorb via this process, they are expected to have a much higher kinetic energy relative to the thermal distribution. As discussed in more detail later, this is consistent with the nonthermal velocity distribution dominant at the 10 eV resonance.

Direct and indirect dissociation of the excited parent or molecular fragments can also occur when the electron autodetaches. When the electron leaves, neutral $SiCl_4$ can be left in various electronic and vibrationally excited states depending on the wavefunction overlap and the autodetachment lifetimes. This process is illustrated as the grey region with vertical lines in Figure 4.5. The excited neutral $SiCl_4$ can dissociate into the neutral and possibly excited fragments: $SiCl_3^{(*)} + Cl^{(*)}$ or $SiCl_2^{(*)} + 2Cl^{(*)}$.

In addition, other processes that directly produce neutral chlorine occur near 10 eV. As shown in Figure 4.5, unimolecular dissociation into $SiCl_2^* + 2Cl$, $SiCl + Cl_2 + Cl$, and $SiCl_2^* + 2Cl$ at excitation energies of 9.9, 10.1, and 11.3 eV, respectively, have been reported [63-65]. These dissociative states along with another state [64] at 7.5 eV lie within the 10 eV structure and directly produce neutral atomic chlorine atoms in the ground state. In the $Cl(^2P_{3/2})$ ESD data, there appears to be an increase in the baseline

that begins within the resonance at 10 eV. This monotonic increase materializes below the IP and could be due to an overlap with the resonance centered at 14 eV.

Although none of the mechanisms mentioned above produce neutral silicon directly, each of these precursors will likely fragment into Si^+ and $SiCl^+$ upon desorption and interaction with the laser field. Decay pathways from the DEA resonances will produce vibrationally and possibly electronically excited $SiCl_3^{(*)}$ which can further fragment to $SiCl_2^{(*)}$ or $SiCl^{(*)}$. The dissociative states at 7.5, 9.9, 10.1, and 11.3 eV produce $SiCl_2$, $SiCl_2$*, SiCl, and $SiCl_2$* respectively [63-65]. Since these $SiCl_x^{(*)}$ species are produced concurrently with atomic chlorine, their fragmentation into neutral silicon and silicon chloride produces the similar structures as illustrated in the data of Figure 4.2.

There have been no reports of $Cl(^2P_{1/2})$ production from these dissociative states or dissociation originating from the Feshbach resonance. We suggest that the upper spin state of neutral chlorine is produced from Feshbach related dissociations via vibronic coupling. In summary, we attribute the significant structure in the ESD yield of $Cl(^2P_{3/2})$, $Cl(^2P_{1/2})$, as well as Si and SiCl centered at 9 - 10 eV as products of several processes including DEA, direct and indirect dissociation via vibronic coupling, and unimolecular decay.

4.4.1.2 Features above the ionization potential

Just above the ionization potential at 12.1 eV, there is a sharp feature in the $Cl(^2P_{3/2})$, Si, and SiCl yields at 14 – 15 eV shown in Frame A of Figure 4.2. The 14 – 15 eV feature could be due to the onset of states involving the $7a_1$ and $7t_2$ levels or

dissociative ionic states of $SiCl_4^+$. These include direct ionization from the $7t_2$, excitation from the $7t_2$ to the $10a_1$, $11t_2$, and $10t_2$ Rydberg levels, or excitation from the $7a_1$ to the antibonding $8a_1$ or $9t_2$ and $9a_1$ Rydberg levels. These transitions will generate excited states that autoionize to an ionic state or directly dissociate into neutral and cationic fragments. The energetic states relevant to a 14 - 15 eV excitation are illustrated in Figure 4.6. In the gas phase, the repulsive A^2T_2 and B^2E states and the bound C^2T_2 state of $SiCl_4^+$ have been observed at 13.0, 13.5, and 15.3 eV, respectively [66, 67]. The parent $SiCl_4^+$ ion in the A^2T_2 and B^2E states directly dissociate into $SiCl_3^+$ and Cl. Although bound, the C^2T_2 state completely decays via fluorescence to the A^2T_2 and the X^2T_1 state with a 4:1 ratio producing $SiCl_3^+$ + Cl and $SiCl_4^+$ which further fragments into $SiCl_3^+$ + Cl [66, 68, 69]. This process could occur nonradiatively in the condensed phase. From gas phase electron-impact ionization [19] and photoionization [70] measurements, the appearance energy of $SiCl_3^+$ is 12.5 eV. There is a weak threshold for the ESD of $SiCl_3^+$ from condensed $SiCl_4$ multilayers [71] at approximately 17 eV which correlates with these single hole states. However, the primary states leading to $SiCl_3^+$ desorption are two-hole or two-hole, one-electron states, and these do not produce the amount of $SiCl_3^+$ necessary to account for our observed Si and SiCl yields at this incident electron energy. Without the force from a two-hole Coulombic repulsion, the $SiCl_3^+$ produced from the dissociative ionic states could remain on the surface or be neutralized and desorb as $SiCl_3$. Thus, we suggest that the enhanced structure at 14 – 15 eV in the neutral yields is due to resonant dissociative ion states superimposed on the yield from direct dissociative ionization with some possible contributions from DEA.

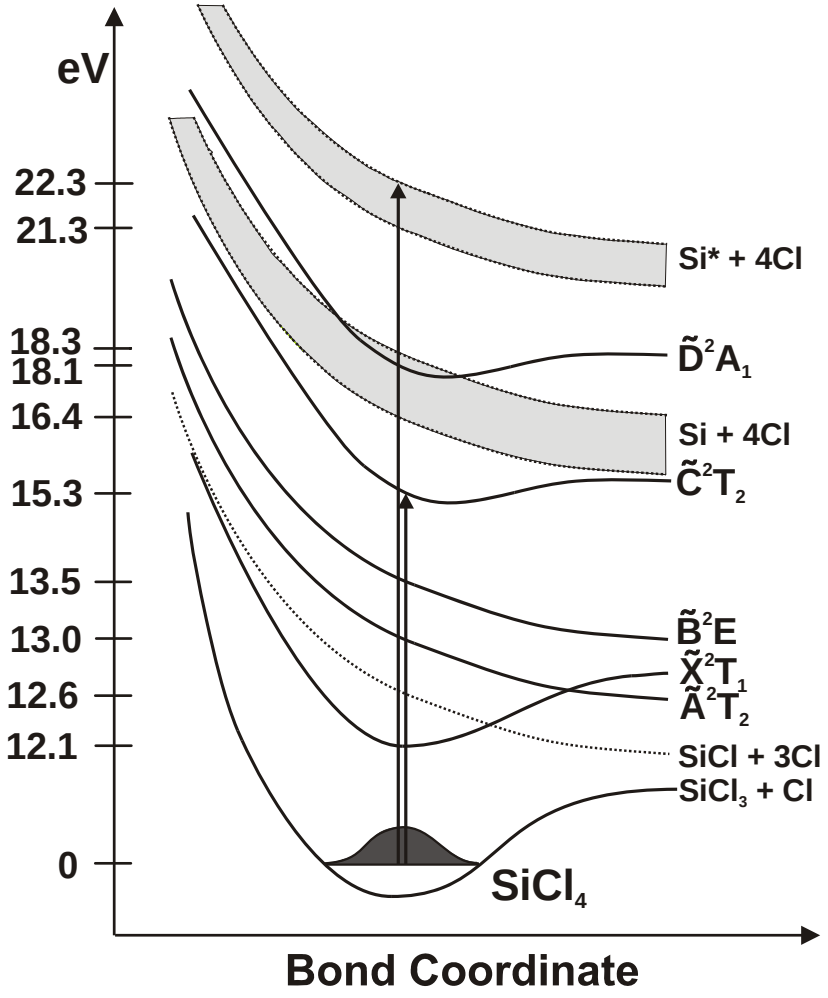

Figure 4.6 Qualitative potential energy diagram of ionic states and dissociative neutral states available above the ionization potential of $SiCl_4$. The light grey shaded areas represent multiple states that produce Si + 4Cl and Si* + 4Cl. Potential energies for ionic and dissociative states and the identities of fragment products have been reported (Refs. [64, 66]).

As the incident electron energy is increased, an abrupt increase in the yields of Si, SiCl, and Cl($^2P_{1/2}$) occurs near 18 eV, and there is a broad feature centered at approximately 25 eV in the Cl($^2P_{3/2}$) data in Figure 4.2. Transitions leading to dissociation occurring at 18 eV probably originate from the $7a_1$ molecular orbital although the $6t_2$ and $6a_1$ molecular orbitals will contribute to the broad feature at 25 eV. The gas phase $SiCl_4$ molecule sequentially dissociates to Si + 4Cl between 16.4 – 18.3 eV and to Si* + 4Cl between 21.3 – 22.3 eV [64]. The bound D^2A_1 ionic state nonradiatively decays to $SiCl_2^+$ + 2Cl and $SiCl_3^+$ + Cl at 18.1 eV [66]. These transitions are illustrated in Figure 4.6. The onset of these dissociative states can explain the yield increase at 18 eV, but not the broad 25 eV feature.

A pronounced maximum in the cross-sections for producing $SiCl^+$, $SiCl_2^+$, $SiCl_3^+$ and $SiCl_4^+$ from electron-impact ionization of gas phase $SiCl_4$ was observed at 30 – 35 eV indicating contributions from indirect ionization channels [19]. We reported a resonance structure in the Cl^+ yield from ESD of $SiCl_4$ multilayers between 22 and 32 eV. This was attributed to initial hole production in the $6t_2$ and $6a_1$ followed by an Auger process initiating desorption via Coulomb repulsion [71]. Lower energy processes such as dissociation resulting from the 10 eV excitation initiated by inelastic electron scattering and secondary emission begin to contribute at these energies as well. It is evident that multiple processes producing both neutral and cationic species occur at these incident electron energies, and it is difficult to assign a dominant mechanism.

4.4.1.3 Enhancement of nonresonant yields at the $^2D_{3/2} \leftarrow {}^2P_{3/2}$ transition

When comparing the yields of Si and SiCl in Figure 4.2(b) and 4.2(c) to those in Figure 4.2(a), it is clear that there is an enhancement of the yields at the chlorine $^2D_{3/2} \leftarrow {}^2P_{3/2}$ intermediate state transition. This enhancement is solely a function of the photon wavelength and not due to a surface phenomenon. Of the resonant neutral species that desorb as a result of ESD, ground state chlorine, $Cl(^2P_{3/2})$, is the most abundant. Due to the high population density in the laser field, resonant ionization of $Cl(^2P_{3/2})$ can induce cation-electron recombination, ion-molecule reactions, and other reactive scattering processes in the gas phase similar to plasma induced reactions. These gas phase reactions can further break apart $SiCl_x$ species rendering an enhancement of nonresonant Si^+, $SiCl^+$, and possibly Cl^+ yields. When the photon energy is in resonance with the chlorine ($^2P_{1/2} \leftarrow {}^2P_{1/2}$) transition, the population density of $Cl(^2P_{1/2})$ is simply not enough to induce these gas phase reactions. Therefore, the nonresonant yields of Figure 4.2(b) match those in Figure 4.2(c) within experimental error.

4.4.2 Kinetic energies and mechanisms

4.4.2.1 The $Cl(^2P_{3/2})$ energy distributions

As suggested above in Figure 4.5, possible dissociative pathways that produce the features seen in the $Cl(^2P_{3/2})$, $Cl(^2P_{1/2})$, Si, and SiCl ESD yields at 10 eV include: DEA, direct and indirect dissociation via vibronic coupling, and unimolecular decay. The

nonthermal 425 meV component in the $Cl(^2P_{3/2})$ ToF distribution is likely due to repulsive forces associated with the DEA resonances and the dissociative excited states produced via autodetachment. Multiple components in the energy distributions typically indicate either multiple excited states or different initial states which have varying Franck-Condon factors. If $Cl(^2P_{3/2})$ does not desorb directly from the near surface region upon excitation, the departing Cl may also undergo collisions or scatter along the surface and begin to thermalize and equilibrate to the surface temperature. Thus the intermediate energy likely involves Cl atoms which suffer only one collision or originate from a layer below, whereas the component fully equilibrated to the substrate temperature obviously involves multiple collisions.

The higher energy incident electrons excite dissociative ionic states and secondary electrons excite the lower energy DEA resonances. It has been reported that the kinetic energy release to $SiCl_3^+$ + Cl fragments from the Franck-Condon maximum of the C^2T_2 $SiCl_4^+$ ion state is 0.43 eV which may be a direct measurement of the repulsiveness of the A^2T_2 and the X^2T_1 states if C^2T_2 completely decays to A^2T_2 and X^2T_1 [68]. Although the authors suggest this measurement may be degraded due to multiple isotopes of chlorine and silicon [66], their 0.43 eV value agrees well with our measurement of the $Cl(^2P_{2/3})$ nonthermal component at 425 meV. It is important to note that the thermal contribution increases as the incident electron energy and penetration depth increases. Thus, it is very reasonable to expect a distribution which is dominated by a nonthermal component at E_i = 10 eV and one which is dominated by a thermal component for E_i = 25 and 50 eV.

4.4.2.2 The Cl($^2P_{1/2}$) energy distributions

Though the low Cl ($^2P_{1/2}$) yield near 10 eV precluded a measurement of the time of flight distribution, it is likely associated with DEA and vibronic interactions, and therefore, should be at least as energetic as that observed for the Cl ($^2P_{3/2}$) product at 10 eV. In fact, the effective temperature of the highly energetic nonthermal component is 4700 K having a kinetic energy of ~608 meV. This is considerably higher than the nonthermal component of the Cl ($^2P_{3/2}$) product. In addition, the thermal component is very small relative to the nonthermal component even at E_i = 50 eV (see Figure 4.4). We have previously shown that desorption products which have only nonthermal components are indicators of exciton decay directly at the surface [46]. This is normally the lowest n-exciton and can be the parent excited state of the DEA resonances leading to the Cl^- anion. Having similar partial cross section values for spin-orbit production in multiphoton detachment [72], autodetachment of the Cl^- anion should generate both Cl($^2P_{3/2}$) and Cl($^2P_{1/2}$). The lack of thermal contributions in the Cl($^2P_{1/2}$) time of flight distribution is consistent with direct dissociation from take-off trajectories normal to the surface where post-dissociation scattering is minimal.

4.4.2.3 The Si energy distributions

The time of flight distributions of nonresonant silicon from the $^2D_{3/2} \leftarrow {}^2P_{3/2}$ transition of chlorine have the same relative distribution profile as the incident electron energy is increased. Since silicon is a product of a $SiCl_x$ precursor that dissociates and is

nonresonantly ionized in the laser field, the silicon distributions will have the kinetic energy signature of a heavier parent molecule. The broad Si ToF distribution is produced from the desorption of $SiCl_x$ precursors that are created from the identical mechanisms that produce chlorine. Since Si is a byproduct of these desorption mechanisms via the laser field, its kinetic energy will not be necessarily relevant to specific surface processes producing $SiCl_x$, but helpful for chlorine kinetic energy comparisons.

4.5 Conclusions

We have detected the desorption of ground state neutral chlorine, $Cl(^2P_{3/2})$, excited state neutral chlorine, $Cl(^2P_{1/2})$, as well as Si and SiCl during low-energy electron bombardment of multilayers of $SiCl_4$ adsorbed on a Si(111) substrate. Resonance structure in the $Cl(^2P_{3/2})$ yield at 10 eV was attributed to dissociative electron attachment, direct dissociation from repulsive excited states, and unimolecular decay of excited products produced via autodetachment. These processes yield $Cl(^2P_{3/2})$ with a nonthermal kinetic energy of 425 meV and a slower component near the surface thermal temperature. Other structures at 14 eV and 25 eV were also observed in the $Cl(^2P_{3/2})$ yield originating from excitation of electrons in the 2e, $7t_2$ and $6t_2$, $6a_1$ molecular orbitals, respectively. Although the 14 eV feature was not present in the $Cl(^2P_{1/2})$ yield, the 10 eV resonance and broad 25 eV feature are present. The former involves DEA, autodetachment and direct dissociation, whereas the latter involves complex Auger decay of holes in the $6t_2$ and $6a_1$ levels. As the incident electron energy is increased, direct ionization, excitonic states, and DEA from secondary electron scattering, can occur

contributing to all neutral atomic chlorine yields. Si and SiCl species were also detected via nonresonant ionization of $SiCl_x$ precursors that desorb from the $SiCl_4$ multilayers. These precursors are produced via the same mechanisms that yield atomic chlorine where the broad time of flight distribution of Si retains the kinetic energy profile of the precursors. This study can help elucidate the mechanisms of low-energy electron induced decomposition of adsorbed $SiCl_4$ and may be useful for tailored surface reactions induced by monoenergetic incident electron energies.

CHAPTER 5

ELECTRON IRRADIATION OF THIN FILMS OF SILICON TETRACHLORIDE ON SILICON(111)

5.1 Introduction

The objective of the previous two chapters was to investigate the electron induced reactions on and within thick (100 ML) films of $SiCl_4$ on Si(111) using time of flight spectrometry (ToF-MS) as a tool to detect the neutral and cationic desorption products. Taking a multilayer to monolayer approach to examine the $SiCl_4$/Si(111) system, this chapter discusses electron induced reactions on thin films of $SiCl_4$ ($\theta < 3$ ML). Here, the ESD yields of Cl^+ and $Cl(^2P_{3/2})$ from thin films of $SiCl_4$ on Si(111) are presented, and the trends in the ESD yields are discussed as a function of $SiCl_4$ adsorbate coverage.

As illustrated in Figure 2.1 of Chapter 2, the electronic structure of condensed $SiCl_4$ is similar to that of gas phase $SiCl_4$, but with some broadening due to formation of the bands. To date, there have been no photo-electron measurements from thin films of $SiCl_4$ on Si(111) to ascertain the substrate effects on the electronic structure; however, ESD of Cl^- has been performed from 1 ML of $SiCl_4$ on Si(100) [32]. These experiments demonstrated that resonance structure at 8 - 12 eV due to DEA is present from a monolayer of $SiCl_4$ on Si(100) [32]. Structure in both spin-orbit states of neutral Cl desorption between 8 - 12 eV was observed from the $SiCl_4$ multilayer and assigned as a product of a DEA resonance discussed in Chapter 4 and generally corresponds with the Cl^- data. The correlation in the $Cl(^2P_{3/2})$ ESD resonant structure from the $SiCl_4$

monolayer and multilayer suggests that electron excitations in the multilayer are relevant to a monolayer coverage of $SiCl_4$.

Understanding the electron-induced reactions in multilayers and thin layers of $SiCl_4$ was performed to exploit low-energy electrons as an assisting tool for controlled silicon surface etching with $SiCl_4$. With a background pressure of $SiCl_4$, etching experiments were executed with and without the presence of a rastering beam of electrons. The scanning electron microscope (SEM) images of both the electron irradiated and non-irradiated surfaces are presented at the end of this chapter along with general conclusions.

5.2 Experimental Details

The procedures for obtaining the results in this chapter are similar to those in the experimental sections of Chapter 4. Here, the ESD yields of Cl^+ and the ground spin-orbit state of neutral Cl were taken simultaneously. A brief description of the detection method is as follows, a plume of desorbates containing both neutrals and ions is created as a result of inelastic electron collisions with the $SiCl_4$ film. A negative potential pulse is applied immediately after the electron beam pulse that extracts Cl^+ from the sample region while $Cl(^2P_{3/2})$ neutrals are left in their desorbing trajectories with their initial kinetic energy. A 0.4 mJ/pulse laser beam is focused approximately 1 mm above the surface to ionize the $Cl(^2P_{3/2})$ species via (2 + 1) REMPI. The 2 + 1 scheme involved the $Cl(4p\ ^2D_{3/2} \leftarrow 3p\ ^2P_{3/2})$ transition at 235.336 nm [48, 49]. ESD yields as a function of incident electron energy were taken by increasing the incident electron energy from 1 to

50 eV in 1 eV increments while maintaining a constant electron pulse to laser pulse delay time of 200 ns. (In the time of flight spectrum the Cl^+ and $Cl(^2P_{3/2})$ signals are separated by 200 ns.) To sample the entire spectrum of $Cl(^2P_{3/2})$ desorption velocities, a 15 μs electron beam pulse width was used. Due to the large width of the electron beam pulse, slow and fast $Cl(^2P_{3/2})$ are present in the ionizing laser field simultaneously. The low electron fluence (5.47×10^{10} e^-/cm^2 s) minimized surface charging during the electron pulse and the frequency (20 Hz) allowed discharging between pulses.

5.3 Results and Discussion

5.3.1 TPD of thin films of $SiCl_4$

ESD yields of Cl^+ and $Cl(^2P_{3/2})$ were measured from a 1.6 ML and a 2.1 ML coverage of $SiCl_4$ deposited on the Si(111) surface by directionally dosing the vapor at 1.0×10^{-7} Torr for 1.5 s and 3.0 s, respectively. During deposition, the backing pressure was approximately 2 Torr, and the silicon substrate temperature was kept below 110 K to achieve a relatively high sticking coefficient. The TPD spectra of both $SiCl_4$ coverages are plotted in Figure 5.1. Due to cracking of $SiCl_4$ in the QMS ionizer, Si^+ (mass 28) was monitored in the TPD measurements to determine $SiCl_4$ coverage. The temperature ramp for the TPD measurements was 1.5 K/s, and the coverages were calculated by dividing the integrated amount in the multilayer peak (~138 K) by that in the monolayer peak (~150 K). In the figure, the monolayer desorption peak is labeled, and the y-axes of the TPD spectra have been offset for comparison.

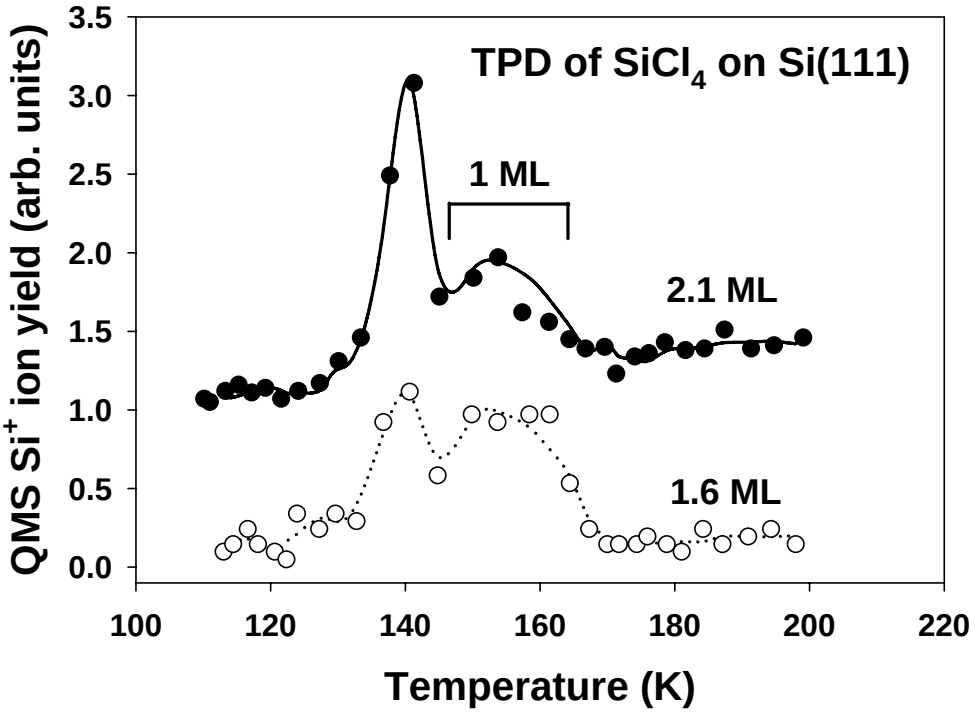

Figure 5.1 Temperature programmed desorption (TPD) spectra of 1.6 ML(○) and 2.1 ML(●) coverages of $SiCl_4$ from the Si(111) surface.

5.3.2 ESD of Cl^+

The ESD yields of Cl^+ from $SiCl_4$ coverages of 1.6 and 2.1 ML are plotted in Figure 5.2 as a function of incident electron energy. Both coverages have an appearance threshold at ~ 17 eV which is easily seen in the zoomed (x10) inset of Figure 5.2. The threshold value of 17 eV agrees with that of the ESD Cl^+ yield of from the multilayer coverage of $SiCl_4$ (100 ML) shown in Figure 3.2. There, the 17 eV Cl^+ threshold was assigned to direct ionization or single particle excitations from the $7a_1$ bonding level which is located 17.4 eV below the vacuum level. After the initial desorption near 17 eV, the Cl^+ ESD yield intensities increase monotonically as the incident electron energy is

increased to 50 eV. However, the Cl^+ ESD yield intensity from 2.1 ML of $SiCl_4$ remains greater than that from the 1.6 ML film. The ionization cross-section producing Cl^+ should not change due to increasing the $SiCl_4$ coverage from 1.6 to 2.1 ML but, the increase in the Cl^+ desorption yield could be resulting from a higher desorption escape probability. This could occur because the inelastic electron scattering event takes place further away from the substrate and ion recombination with secondary electrons and interaction with the substrate image potential are minimized.

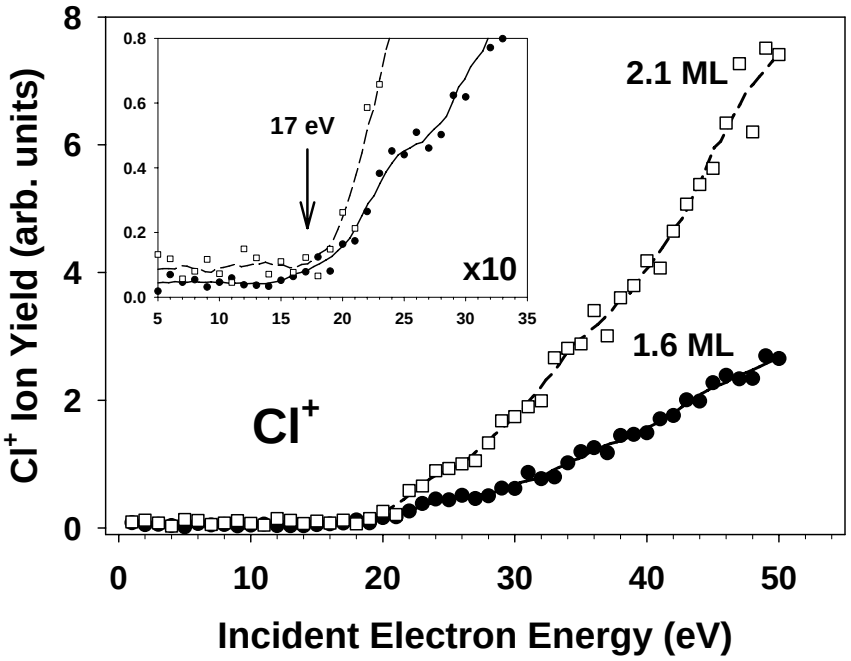

Figure 5.2 ESD yields of Cl^+ from 1.6 ML(●) and 2.1 ML(□) of $SiCl_4$ on Si(111). The inset shows the zoomed (x10) portion of the threshold region at low incident electron energy.

Although the 17 eV appearance threshold is present for Cl^+ ESD yields from both thick and thin films of $SiCl_4$, there is a dissimilarity at higher incident electron energy. The resonance feature found between 22 and 32 eV in the Cl^+ ESD yields from the $SiCl_4$

multilayer is not present in either Cl^+ ESD yields from 1.6 or 2.1 ML $SiCl_4$ films. The resonance structure was associated with resonant transitions from the $6t_2$ or $6a_1$ to the antibonding $8a_1$ or $9t_2$ levels followed by an Auger decay process. A possible explanation could be that the molecule's close proximity to the silicon substrate perturbs the $8a_1$ and the $9t_2$ levels, thus quenching the excitation.

5.3.3 ESD of $Cl(^2P_{3/2})$

Along with the measurement of the Cl^+ ESD yield during electron irradiation, detection of the ground spin-orbit state of chorine ($Cl(^2P_{3/2})$) was carried out using a (2 + 1) REMPI scheme. The ESD yields of neutral $Cl(^2P_{3/2})$ from 1.6 and 2.1 ML coverages of $SiCl_4$ are shown in the top portion of Figure 5.3. The ESD yields from the 2.1 ML film have been displaced on the y-axis for comparison with the 1.6 ML film. Evident from the figure, the $Cl(^2P_{3/2})$ ESD yields from the 1.6 ML $SiCl_4$ film are negligible remaining near zero through 20 eV of incident electron energy. However, the neutral chlorine ESD yields from the 2.1 ML $SiCl_4$ film is non-zero. The resonance structure at 10 eV which is probably a product of a DEA resonance is present, and the $Cl(^2P_{3/2})$ yield increases from 12 to 20 eV. The change in neutral chlorine ESD yields is quite drastic for only adding half a monolayer to the 1.6 ML film, but the full second monolayer is completed with the addition. There is also an interesting trend in the ESD yields of Cl^- as a function of $SiCl_4$ coverage as well. The bottom portion of Figure 5.3 shows the dependence of the total relative Cl^- ion ESD yield on $SiCl_4$ coverage on the Si(100) surface [32]. Evident from the figure, the Cl^- ion yield increases as the submonolayer

$SiCl_4$ coverage is increased until a maximum Cl^- yield intensity is reached at ~1 ML. Above 1 ML, the Cl^- yield decreases monotonically until a $SiCl_4$ coverage of approximately 4 ML where the Cl^- yield remains unchanged. In this portion of the figure, the vertical dashed lines denote the $SiCl_4$ coverages on the Si(111) surface in our experiments. It is interesting to note that the Cl^- ion yield decreases from 1.6 to 2.1 ML as the neutral $Cl(^2P_{3/2})$ yield increases. This can occur since the neutral chlorine channel can be a decay pathway for Cl^- ions. For example, the DEA resonance at 10 eV is observed in the $Cl(^2P_{3/2})$ (Chapter 4) and the Cl^- yields [32]. As discussed above in Chapter 4, there are multiple mechanisms where neutral chlorine can be produced from a DEA process that primarily yields Cl^- ions. If the electron attached to the transient negative ion ($SiCl_4^-$) autodetaches prior to dissociation, the parent $SiCl_4$ molecule can be left in a vibrationally excited state inducing dissociation that yields a neutral chlorine atom. Another possible pathway for producing $Cl(^2P_{3/2})$ is a post-dissociated mechanism where the Cl^- ion either reactively scatters with the surrounding medium or the electron autodetaches, thus liberating the electron and desorbing as a neutral chlorine atom. It is the cross-sections of these reaction pathways that dictate the relative ESD yield intensities of Cl^- and $Cl(^2P_{3/2})$. By accounting for the correlations between Cl^- and $Cl(^2P_{3/2})$, the inverse relationship in the ESD yields of Cl^- and $Cl(^2P_{3/2})$ can be understood. As the inelastic electron scattering event is removed from the silicon substrate effects due to an increase in $SiCl_4$ coverage, the reaction cross-sections for producing $Cl(^2P_{3/2})$ must increase causing the desorption yields of the Cl^- ion to decrease.

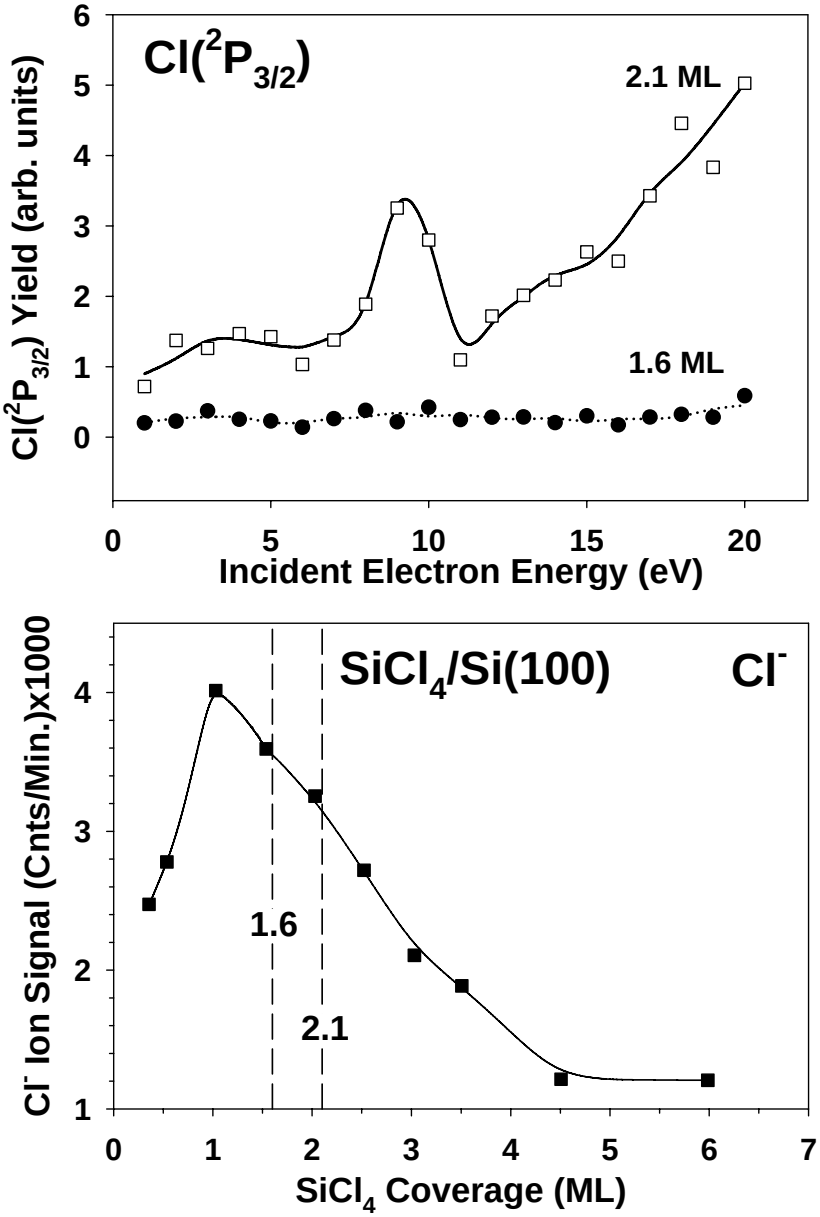

Figure 5.3 ESD yields of the ground spin-orbit state of neutral chlorine ($Cl(^2P_{3/2})$ from 1.6 ML(●) and 2.1 ML(□) coverages of $SiCl_4$ on a Si(111) surface (top). ESD yields of anionic chlorine (Cl^-) as a function of $SiCl_4$ coverage on the Si(100) surface. The vertical dashed lines denote the $SiCl_4$ coverages studied on the Si(111) surface. The Cl^- data were taken by Guo and co-workers Ref. [32] (bottom).

5.3.4 Evidence of surface reactions

Besides desorbing from the silicon surface, the anions, cations, and non-thermal neutral species that have been discussed to this point can and do reaction with the silicon surface. $SiCl_4$ primarily etches silicon surfaces specifically after dissociating into reactive chlorinated radicals. To investigate whether electron irradiation assists the etching ability of $SiCl_4$, a designated area of the Si(111) surface was irradiated with electrons while the entire surface was exposed to $SiCl_4$. This experiment was conducted by heating and holding the silicon substrate at ~1000 K where the background pressure of $SiCl_4$ gas was held constant at 1.3 - 1.5x10^{-5} Torr for 30 min. During this time, half of the Si(111) surface was irradiated with 100 eV electrons. At this incident electron energy, all of the electron initiated reactions discussed above are possible. The onset of etching silicon with $SiCl_4$ occurs near 1000 K due to the presence of $SiCl_2$ desorption in TPD spectra where remaining dissociated Cl from $SiCl_4$ react with the surface producing $SiCl_2$ [51, 52]. The etching process is initiated when chlorine atoms insert into the Si-Si backbond [73]. The resulting SEM images of the a) non-irradiated and the b) irradiated Si(111) surfaces are shown in Figure 5.4. The surface areas in the images are identical where a distance of 2.0 μm is indicated on the images. The scanning electron energy was 15.0 kV. When comparing the images, there is a significant difference in the etching quality. The irradiated surface has a much smoother finish than the non-irradiated surface indicating a more constant etch rate over a very large surface area. The large trenches that appear in both images could be a result of inhomogeneous

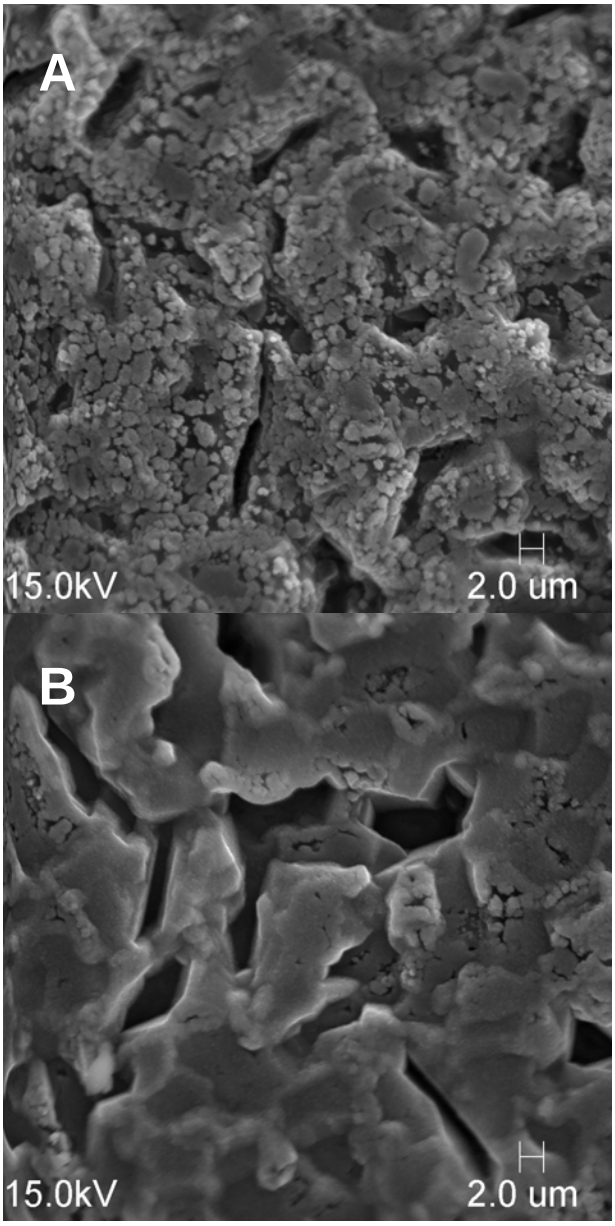

Figure 5.4 SEM images of Si(111) surfaces that were etched with $SiCl_4$ while simultaneously a) not irradiated and b) irradiated with 100 eV electrons.

etching that could be a function of changes in the instantaneous $SiCl_4$ vapor flux or local surface temperatures during the etch process. Although the $SiCl_4$ etching process was quite inhomogeneous across the Si(111) surface, the effects of the 100 eV electron beam are evident, and justify more experimentation.

5.4 Conclusions

As adsorbate films become thinner, the substrate effects have a profound influence on the chemical reactions initiated by electrons. In the case of the $SiCl_4$ film thickness dependence, the substrate influence is manifested in the $Cl(^2P_{3/2})$ and Cl^- ESD yields. As these reactant fragment species are produced, they frequently react with the substrate surface itself. The electron assisted etching experiments with $SiCl_4$ presented are preliminary results that have stimulated further investigations in our laboratory. Utilization of low energy electrons can make a significant difference in controlled chemical vapor deposition (CVD) of silicon for instance with $SiCl_4$ in the presence of H_2 [74] or with other silicon precursor molecules such as SiH_4 [75]. CVD of silicon carbide films are also possible using carbon sources such as acetylene [76, 77], acetylene/dichlorosilane [78], and ethylene [79]. As demonstrated above, resonant reactions stemming from DEA resonances are dependent upon the incident electron energy. A variety of surface reactions induced by excitation of the DEA resonances of selected adsorbates have been performed on silicon substrates [80-83]. It is in the direction of surface reactions tailored toward silicon carbide film growth through DEA resonances of aromatic precursor molecules that our investigations are progressing.

CHAPTER 6

WATER INTERACTIONS WITH THE TITANIUM DIOXIDE(110) SURFACE

6.1 Introduction

Titanium dioxide is an environmentally abundant material that has become a lucrative commodity for its uses and applications [84]. Besides its industrial relevance, TiO_2 is the most studied transition metal oxide and TiO_2(110) is considered a model surface to understand thermal and non-thermal reaction dynamics. Fujishima et al. have demonstrated hydrogen production via the photocatalytic dissociation of water on the TiO_2(110) surface [85]. Water dissociation producing molecular hydrogen from a non-organic source is a possible route for manufacturing a fuel that is free of greenhouse gas emissions, specifically carbon dioxide. Understanding the thermal and non-thermal reaction landscape for water adsorbed on the TiO_2 interface is relevant for the possible realization of this system as a potential photocatalytic water splitting hydrogen fuel source.

For the rutile TiO_2 crystal, the band gap energy is 3.05 eV [86]. The valence band and the conduction band are derived from O 2p and Ti 3d contributions, respectively [87]. An extensive overview of the electronic structure and surface chemistry of TiO_2 have been reviewed [84, 88-90]. The (110) surface of rutile TiO_2 has a corrugated structure composed of rows of bridge bonding oxygen (BBO) atoms and fivefold coordinate titanium atoms in the [001] direction. A cartoon of the TiO_2(110) surface depicting the adsorption sites of water is shown in Figure 6.1. Whether water

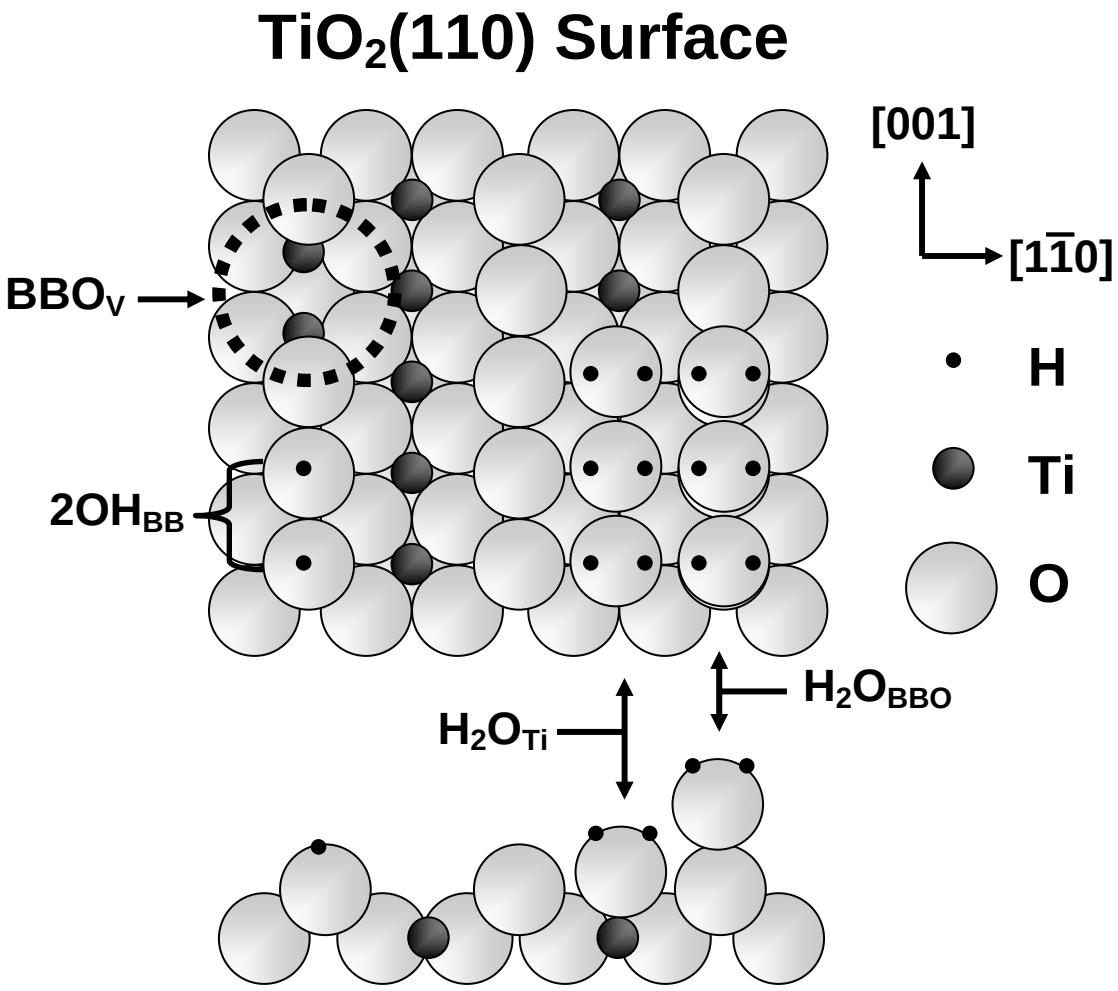

Figure 6.1 A cartoon of the H_2O deposited on the $TiO_2(110)$ surface. Water adsorbed to the BBO and Ti atoms are illustrated along with a bridge bonding oxygen vacancy (BBO_V) and hydroxyls ($2OH_{BB}$) resulting from H_2O reaction with a BBOv.

dissociatively or molecularly adsorbs on this surface has been the subject of much debate. Scanning tunneling microscopy (STM) suggests that water dissociates upon adsorption at the defect oxygen vacancy sites creating two hydroxyls by depositing an OH in the vacancy and an H on the BBO next to the vacancy [91]. These hydroxyls thermally recombine and desorb as H_2O at ~500 K, thereby regenerating the oxygen vacancy site. Experimentally, there has been no evidence for water to dissociate at any other adsorption sites on the surface.

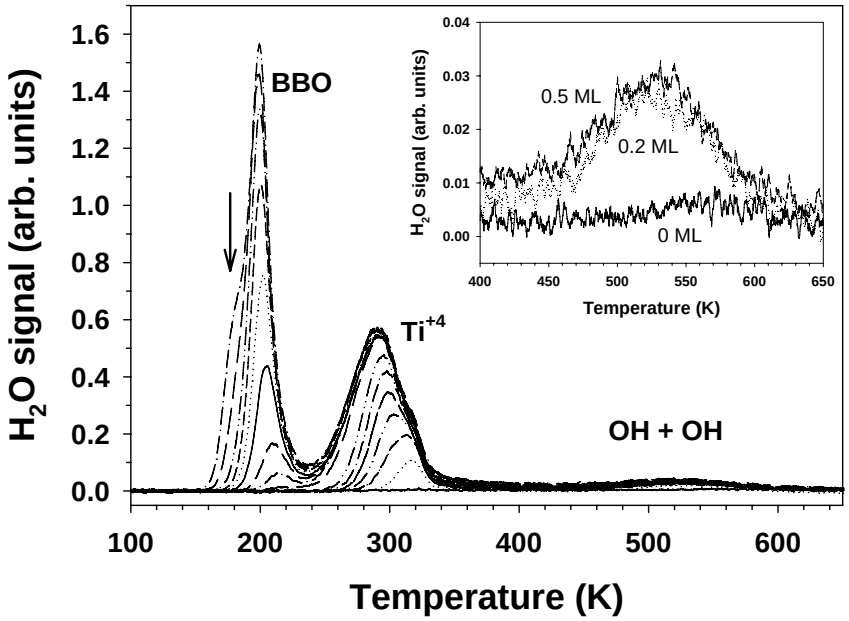

Figure 6.2 H_2O TPD spectra from the TiO_2(110) surface (total coverage = 2.2 ML). Water desorbing from the Ti^{+4} sites (~200 K), BBO's (~300 K), and the recombinative desorption of hydroxyls (~540 K) are labeled. A zoomed depiction of the high temperature recombinative peak is shown in the inset. The low temperature shoulder on the Ti^{+4} peak denoted by the arrow indicates the onset of the multilayer.

An example of TPD spectra of H_2O from the TiO_2(110) surface is shown in Figure 6.2. The figure depicts the water desorption states from the Ti^{+4} sites (~200 K), BBO's (~300 K), and the recombinative desorption of hydroxyls (~540 K). A zoomed

depiction of the high temperature recombinative peak is shown in the inset. The low temperature shoulder on the Ti^{+4} peak denoted by the arrow indicates the onset of the H_2O multilayer.

Rutile TiO_2 crystals are reduced by annealing in vacuum which introduces oxygen vacancies into the bulk and on the surface [92]. Removal of the surface oxygens leaves two paired reduced Ti^{+3} ions where the remaining electrons exhibit Ti 3d character [84]. Ultraviolet photoelectron spectroscopy (UPS) measurements have shown that the electrons occupy a state that is ~0.8 eV below the Fermi level within the band gap [93, 94]. The reaction of H_2O with these vacancy sites is exothermic where the H_2O diffusion is the rate limiting step [91, 95]. Following hydroxyl creation, the Ti^{+3} ions below the reacted vacancy are not fully reoxidized retaining a partial negative charge. The charge associated with the defect remains delocalized below the reacted vacancy site [96-98] and has been shown to extend into the fivefold coordinate Ti^{+4} row [99]. Ultrafast charge transfer from the TiO_2 defect state below the hydroxyl group to wet electron states of H_2O and CH_3OH have been demonstrated [100, 101], and due to dissimilar hydrogen hopping rates, the hydroxyl groups are thought to be inequivalent attributed to the residual negative charge below the reacted defect site [102].

6.2 Experimental Details

The experiments were performed in an UHV system that has been described previously [103, 104] and illustrated in a top-down view in Figure 6.3. Briefly, the system consists of a low-energy electron gun, a closed-cycle helium cryostat, a molecular

beamline for adsorbate deposition, an Auger electron spectrometer, and a QMS equipped with an integrating cup [105]. In Figure 6.3, the QMS is mounted to the bottom of the chamber where the integrating cup directs desorbates into the quadrupole ionizer. The typical base pressure for the system was 1×10^{-10} Torr. The $10\times10\times1$ mm $TiO_2(110)$ crystal (CrysTec GmbH or Princeton Scientific) was mounted on a resistively heated tantalum base plate using a thermoconductive cement (Aremco Ceramabond 865). For temperature monitoring and control, we used a K-type thermocouple that is spot-welded to the tantalum base plate. A secondary electron image of the sample holder configuration in Figure 6.4 shows the TiO_2 single crystal pressed between a molybdenum ring and a tantalum base plate. The outer dashed ring indicates the $TiO_2(110)$ surface where the diameter is 10 mm.

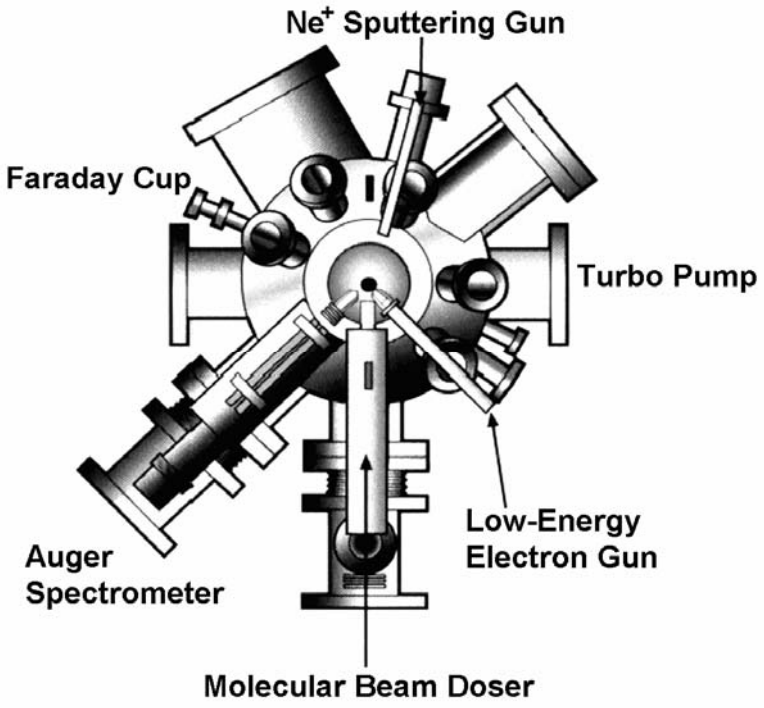

Figure 6.3 A top-down representation of the UHV apparatus at PNNL.

Prior to experiments, the TiO_2 sample was sputtered with Ne^+ ions and then annealed in vacuum for 2 or 10 min at ~850 K. After multiple sputtering/annealing cycles, the TiO_2 sample is reduced attaining an intensive blue color, related to the bulk defects. The bulk reduction increases the sample conductivity and greatly reduces charging effects during electron irradiation experiments. This process also introduces ~5 – 8 % of oxygen vacancies at the (110) surface, preferentially in the bridge-bonded oxygen row [106, 107].

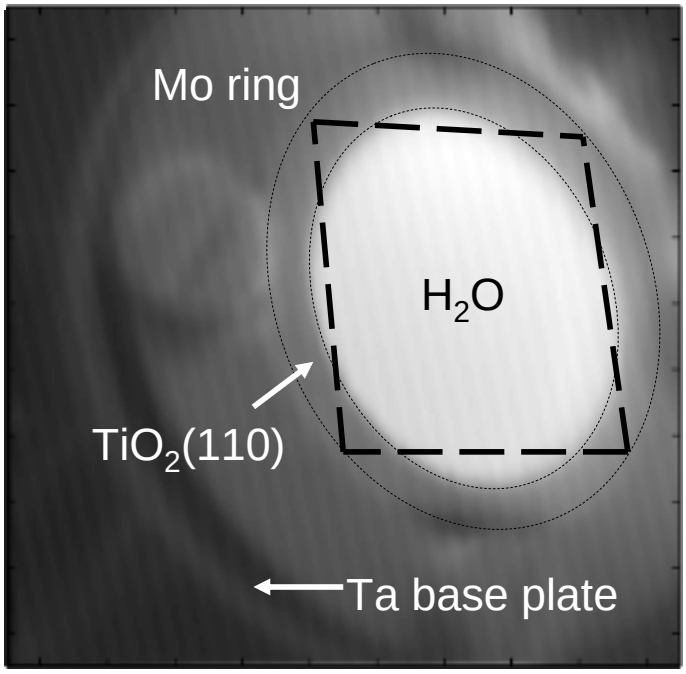

Figure 6.4 Secondary electron image of the TiO_2 single crystal pressed between a molybdenum ring and a tantalum base plate. The outer dashed ring indicates the $TiO_2(110)$ surface where the diameter is 10 mm. The bright area is adsorbed H_2O within the inner dashed ring. The electron irradiated area is denoted as the long dashed square.

The amorphous solid water (ASW) ice films were deposited with the molecular beam (~$2x10^{14}$ molecules/cm^2 s) at normal incidence to the $TiO_2(110)$ surface (typically

at 100 K). The molecular beam produced a film centered on the substrate having an outer diameter of ~8 mm which is shown as the bright area within the inner dashed ring in Figure 6.4. One monolayer coverage of water was defined as the desorption yield from the Ti^{+4} rows in the TPD spectra ($5.2x10^{14}$ molecules/cm^2) although the actual density in the saturated monolayer is somewhat uncertain [107]. The second ML is completed when water saturates the bridge bonding oxygen adsorption sites. Note, a 2 ML coverage on the TiO_2(110) surface is comparable to a 1 ML coverage on a Pt(111) surface (~$1.0x10^{15}$ molecules/cm^2).

During ESD experiments, the electron beam was oriented 35° to the sample normal where the films were irradiated with 100 eV incident electrons. A typical instantaneous current density per scan is ~$2x10^{14}$ e^-/cm^2 s with a beam spot size of ~1.5 mm. The water films were uniformly irradiated by repeatedly scanning the electron beam in a grid pattern over an area slightly larger than the film. This area is denoted by the dashed square in Figure 6.4. The pressure rise during irradiation depended on various parameters such as the beam current, the film thickness, and the sample temperature but was typically no more than ~$1x10^{-9}$ Torr.

CHAPTER 7

ELECTRON-STIMULATED OXIDATION OF THE TITANIUM DIOXIDE(110) SURFACE

7.1 Introduction

The interaction of energetic electrons with TiO_2(110) has been studied and used to prepare various surfaces. For example, irradiation of TiO_2(110) by electron energies greater than ~30 eV results in the desorption of O^+ (presumably from BBO sites) via the Knotek-Feibelman mechanism[108, 109]. Energetic electrons can also desorb H^+ from hydroxylated TiO_2(110) [110], healing BBO vacancies in the process. This fact has been used to prepare "fully-oxidized" TiO_2(110) surfaces both with energetic electron beams (e.g. ~20 eV) [111] and STM tips (with a bias voltage of only a few volts) [111, 112]. However, little is known about the interaction of energetic electrons (e.g. ~10-100 eV) with water covered TiO_2(110).

Here, we investigate the low energy electron-stimulated reactions in thin (< 3 ML) water films on the TiO_2(110) surface. During irradiation of water on the TiO_2(110) surface with 100 eV electrons, atomic hydrogen is the primary electron stimulated desorption (ESD) product, along with some molecular H_2. However, at low electron fluences, no desorption of molecular O_2 is detected. Therefore irradiation of the water films leads to the production OH adsorbed on the TiO_2(110). The TPD of the remaining H_2O film reveals features indicative of oxidation of the TiO_2(110) surface. We observe a shift to higher temperature in the 1 ML water TPD state from the Ti^{+4} rows along with a decrease in the OH recombinative desorption peak near 500 K (oxidation of the vacancy

sites). These observations are essentially identical to the results observed by exposing the surface to molecular O_2 prior to depositing water on a TiO_2(110) surface. For both irradiated and O_2 pre-dosed water films, the TPD spectra characteristic of the clean, annealed surface are recovered when the surface is heated above ~600 K. The rate of electron-stimulated oxidation is independent of the initial vacancy concentration, but increases linearly with the water coverage in the Ti^{4+} rows suggesting that these molecules are the "targets" for dissociation by the incident electron. As the coverage increases above 1 ML, the electron-stimulated oxidation of the substrate is suppressed. Initially, the OH's in the Ti^{+4} row that are produced by the H ESD react with hydroxyls adsorbed on the bridging oxygen rows to (re)form water and heal the oxygen vacancies associated with the bridging OH's. When the bridging OH's have been titrated, the OH's in the Ti^{+4} row begin to react with each other to form species (possibly H_2O_2 and/or HO_2) which block H_2O adsorption sites in the Ti^{+4} rows, and ESD of molecular O_2 increases. The results are compared to previous work on the oxidation of TiO_2(110) after exposure to molecular oxygen [113, 114].

7.2 Results

7.2.1 Electron-stimulated desorption of D, D_2, and O_2 from D_2O/TiO_2(110)

Insights into nonthermal electron stimulated reactions in amorphous solid water (ASW) and crystalline water ice (CI) can be made via measurement of the desorbing species produced during electron irradiation such as H^-, H, H_2, O, O_2, etc. [13, 115-119].

To this end, the electron-stimulated desorption yields of the dissociated water fragments D, D_2, and O_2 were measured from the TiO_2(110) surface with and without a monolayer of D_2O during irradiation with 100 eV electrons. Deuterated water was used to distinguish desorbing species from the TiO_2 surface from the background signals due to H_2O. These ESD yields from the water monolayer (filled squares) and from the bare TiO_2 surface (open circles) are plotted as a function of irradiation time (electron fluence) in Figure 7.1. The atomic D signal is derived from the 3 amu mass which corresponds to molecular HD in the QMS. Although this is not a direct measurement of D atoms, the 3 amu (HD) signal is the result of D atoms reactively scattering with adsorbed H_2, H, OH, and H_2O on the surfaces of the UHV chamber and mass spectrometer. The scattering event induces isotopic exchange which occurs prior to reaching the QMS ionizer. Therefore, the 3 amu mass signal is a qualitative indirect measurement of the atomic D yield. D_2 molecules do not contribute to the HD signal. As seen from the plot, the amplitude of the D yield is an order of magnitude greater than that of the D_2 ESD yield indicating that HD is not a product of the D_2 isotopic exchange on the walls prior to detection. The ESD yields of O_2 from the surface with and without water are indistinguishable implying zero electron induced desorption of O_2 from the D_2O film within the duration of the irradiation period in Figure 7.1 (At longer irradiation times, this is not the case and will be discussed in detail below). This is contrary to the D and D_2 yields where desorption occurs immediately upon interaction with 100 eV electrons and where the yields become constant within the irradiation period. For the conditions shown in Figure 7.1, electron-stimulated desorption of D_2O is also significant.

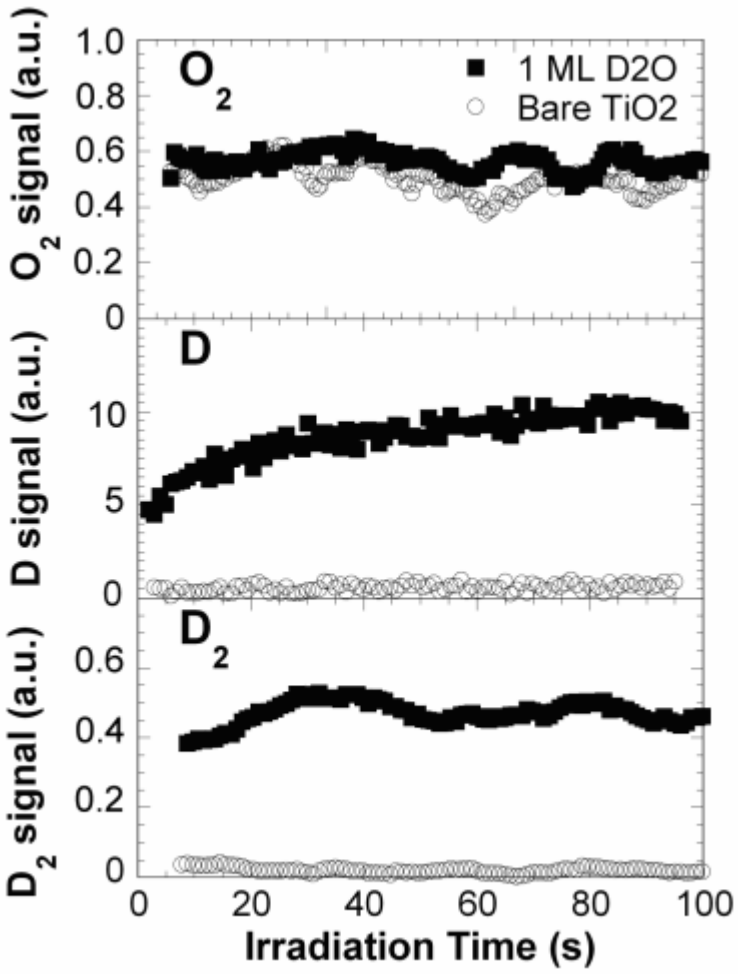

Figure 7.1 O_2, D, and D_2 ESD yields vs. 100 eV electron irradiation time at 100 K from bare TiO_2(110) surface (○, control experiment) and 1.0 ML D_2O (■) on TiO_2(110). The D atom yield is actually the 3 amu signal of HD being a product of the reactive scattering (see details in the text). *

* See Appendix for acknowledgement of data acquisition for Chapters 7 and 8

The extensive desorption of D atoms and D_2 molecules from the water film could indicate a stoichiometric imbalance in the products of dissociated water remaining on the surface. If the atomic D yield is primarily produced by dissociation of D_2O to D and OD, the end result of these electron stimulated reactions leaves an adsorbed OD and to a lesser extent O at the site in the Ti^{+4} row where D_2O resided. In the discussion below, we suggest that these adsorbed species oxidize the TiO_2(110) surface as well as alter the TPD spectra of the remaining irradiated water and additionally deposited water.

7.2.2 Electron-stimulated oxidation of TiO_2 (110)

On many surfaces, water TPD spectra change in characteristic ways in the presence of other adsorbates [89, 120], and previous research has shown that water TPD spectra obtained after irradiation provide valuable information regarding the electron-stimulated reactions [104]. When a 2 ML H_2O film on the TiO_2(110) surface is irradiated with energetic electrons, the oxide surface is irreversibly altered as evident in post-irradiated TPD measurements. These effects are illustrated when comparing the 1) *Not Irradiated* and 2) *Irradiated* TPD spectra in Figure 7.2(a). The TPD spectrum of pristine adsorbed water from the sputtered and annealed TiO_2 (110) surface is composed of three peaks at approximately 195 K, 290 K, and 550 K which have been attributed to water desorbing from the BBOs, the Ti^{+4} rows, and from the recombinative desorption of BBO hydroxyls, respectively [106, 107]. In the discussion below, the desorption peaks in the TPD spectra at 195 K, ~295 K and 525 K will be referred to as the second layer, ML, and

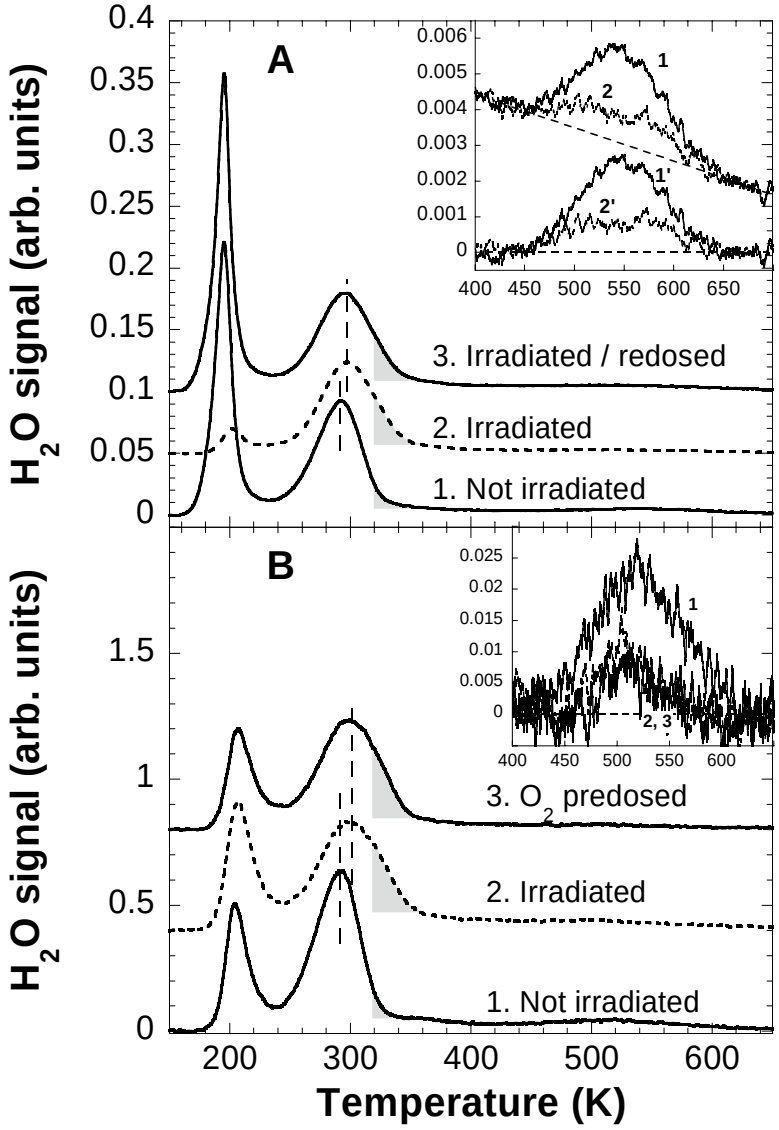

Figure 7.2 A) TPD spectra of 2 ML H_2O films from the TiO_2(110) surface taken 1) before (solid) and 2) after (dashed) irradiation with 100 eV electrons at 100 K. 3) 2 ML of H_2O was irradiated, then molecular water was desorbed up to 400 K, and a new 2 ML H_2O film was re-dosed, of which the TPD spectrum is shown (solid). Zoomed high-temperature peak of H_2O recombinative desorption is shown in the inset for the experiments (1) and (2) along with linear baseline subtraction (curves 1' and 2' respectively). B) TPD spectra of 1.2 ML H_2O dosed at 100 K on a TiO_2(110) surface taken (1) before (solid) and (2) after (dashed) irradiation of 2 ML H_2O film with 100eV electrons or (3) after O_2 pre-dose of at 90 K (solid). For the irradiated (2) TPD, 2 ML of H_2O was irradiated, desorbed up to 350 K, and 1.2 ML H_2O was re-dosed, of which the TPD is shown. The inset is an enlargement of ~500 K recombinative H_2O TPD peak, base line subtracted. The "Not Irradiated" data in A and B are taken at different multiplier sensitivities. Dashed vertical lines show the position of the ~300 K peak shifted after the irradiation. The grey-shaded fragments represent integrated portions of the TPD spectra. See details in text.

OH recombination peaks, respectively. Note that the magnitude of the high temperature water TPD state provides a measurement of the initial oxygen vacancy concentration on the surface [107]. For the irradiated H_2O TPD in Figure 7.2(a), a 2 ML H_2O film was deposited and irradiated at 100 K with 100 eV electrons ($8x10^{15}$ e^-/cm^2). In general, the second layer peak decreases as a result of electron-induced sputtering of H_2O, the ML peak broadens and shifts to higher temperature (~305 K), and the OH recombination peak at 550 K decreases. The vertical lines in the figure illustrate the shift in the ML peak position. The inset is the zoomed area of the decrease in the OH recombination peak where 1 and 2 correspond to the *Not Irradiated* and *Irradiated* data, respectively. To compare the OH recombination peaks, the backgrounds were linearly subtracted, and the data are re-plotted as 1' and 2'. To quantify the electron induced shift in the ML peak, the difference from the irradiated and the non-irradiated H_2O TPD spectra is integrated from 320-360 K for the shifted ML peak and 400-630 K for the OH recombination peak. The temperature range for the shifted ML peak integral is represented as the gray areas in Figure 7.2.

The electron induced changes in the H_2O TPD spectrum remain after desorbing the irradiated water and re-depositing a fresh 2 ML H_2O film. The TPD spectrum of the re-dosed film is labeled as 3) *Irradiated/Re-dosed* in Figure 7.2(a) and obtained after removing the irradiated water film by heating to 425 K then re-dosing 2 ML of H_2O at 100 K. When spectrum 2 is compared to 3, the second layer peak has returned to its initial height (as seen in 1), but the shift in the 1 ML TPD peak is unaffected by heating and re-dosing H_2O. This phenomenon will be discussed in more detail below; however, experimentally, it is helpful. The procedure of removing the irradiated H_2O film by

annealing to ~400 – 425 K and redosing with a fresh H_2O layer (typically 1 ML) precludes effects in the TPD due to removal of H_2O by electron sputtering and allows accurate quantification of the ML peak shift and OH recombinative peak height. This approach will be used repeatedly in what follows.

The changes in the post-irradiation water TPD spectra are essentially identical to the changes in the water TPD spectra when the $TiO_2(110)$ is pre-dosed with O_2. The TPD spectra from 1) *Not Irradiated*, 2) *Irradiated*, and 3) *O_2 pre-dosed* 1.2 ML films of H_2O on the annealed $TiO_2(110)$ surface are plotted in Figure 7.2(b). The irradiated TPD spectrum (2) is obtained from a 1.2 ML H_2O film that has been re-deposited after a 2 ML H_2O film was subsequently irradiated ($8x10^{15}$ e^-/cm^2) then thermally desorbed to 400 K. The O_2 pre-dosed H_2O TPD spectrum (3) is from a 1.2 ML H_2O film after pre-dosing the annealed $TiO_2(110)$ surface with ~1.5×10^{14} molecules/cm^2 of O_2 at 90 K. In both the 2) *Not Irradiated* and 3) *O_2 pre-dosed* TPD spectra, the OH recombination peak has decreased shown clearly in the figure inset where the backgrounds have been linearly subtracted, and the ML peak exhibits similar broadening and shifting to higher temperatures.

Henderson and co-workers have previously demonstrated that exposure of oxygen to the $TiO_2(110)$ surface reduces the number of BBO vacancy sites which affects the TPD spectrum of co-deposited H_2O [98, 113]. The similarity in the TPD spectra from irradiated H_2O and O_2 pre-dosed surfaces indicates that electron irradiation of water films on $TiO_2(110)$ oxidizes the surface. This conclusion is supported by the ESD results presented in Figure 7.1 indicating that D and D_2 desorb during irradiation, but very little O_2. According to the mechanism proposed by Henderson and co-workers [113], O_2

adsorbs dissociatively at the BBO vacancy, healing the vacancy and depositing the other oxygen atom on the Ti^{+4} row (O_{Ti}). Scanning tunneling microscopy experiments also support this mechanism [121]. Upon the subsequent deposition of water, the water reacts with the oxygen adatom yielding two hydroxyls:

$$H_2O + O_{Ti} \rightarrow 2\ OH_{Ti} \tag{5.1}$$

The two hydroxyls now residing in the Ti^{+4} row were proposed to induce the ML TPD state to broaden and shift to higher temperatures upon heating and reproduce water which desorbs at ~300 K leaving behind the oxygen adatom:

$$2\ OH_{Ti} \rightarrow H_2O + O_{Ti} \tag{5.2}$$

As shown in Figure 7.2, the ML TPD peak is not restored to its original pristine position after heating the surface to 400 K; however, the transition back to the original peak position does occur upon annealing the surface to ~500 - 600 K. Oxygen adatoms are removed only after annealing above ~500 - 600 K [113], thus accounting for the observation that heating to ~400 - 425 K and subsequently redosing with water results in essentially the same shift in the ML peak to higher temperature. The results from heating the surface to remove the electron irradiated H_2O and pre-deposited O_2 induced effects in the H_2O TPD spectra are compared in Figure 7.3(a). Each data point was taken by subtracting a pristine H_2O TPD from an affected H_2O TPD spectra then integrating the fraction of the water in the ML peak shift from 320 to 360 K. The integral of the shift in the ML peak is represented by *320 – 360 K* in Figure 7.2 and the following figures. The irradiated data (filled circles) were taken by irradiating (~3.2×10^{16} e^-/cm^2) a 1 ML H_2O

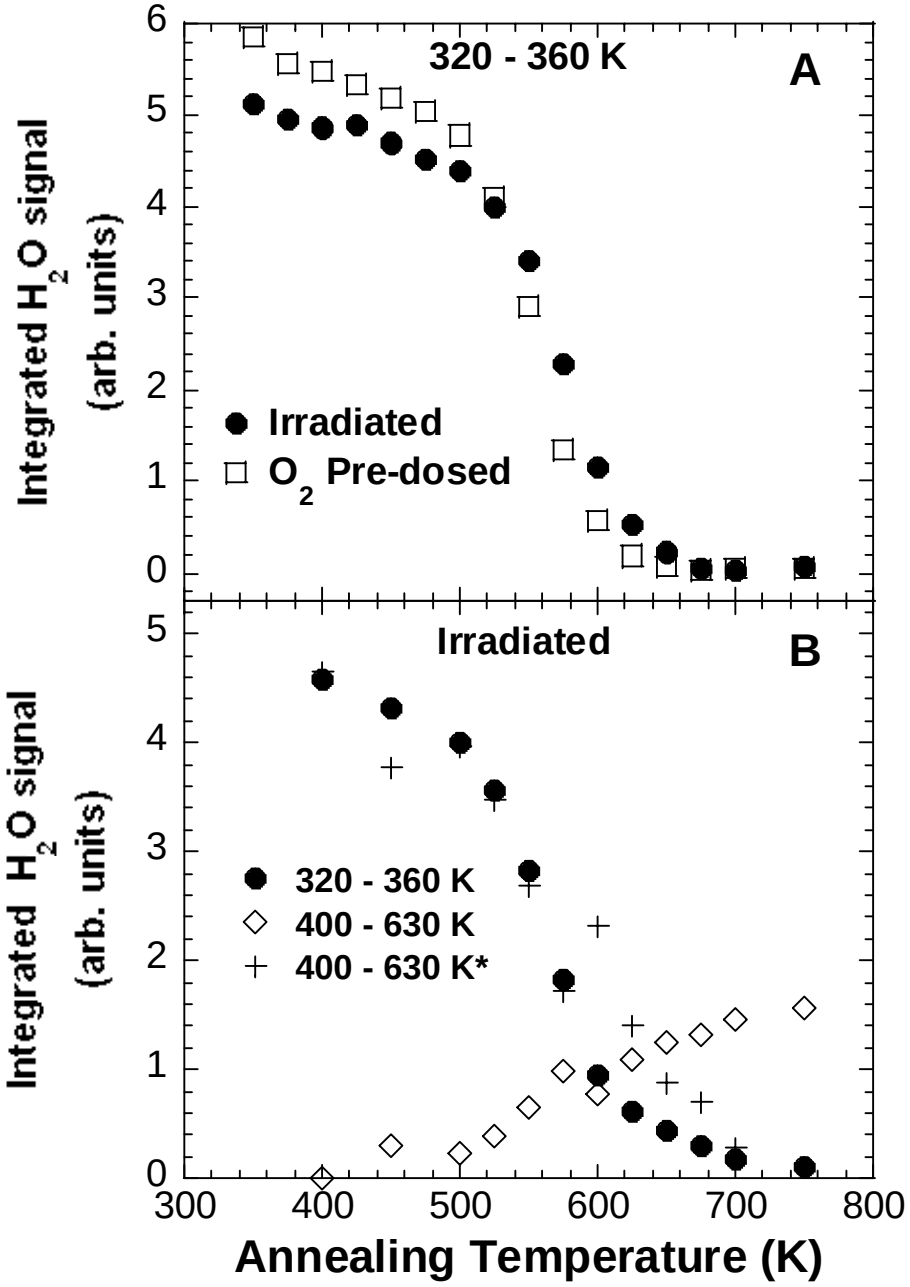

Figure 7.3 A) 320-360 K: ML shift integral from 1 ML H_2O TPD on TiO_2(110) vs. annealing temperature after irradiation with 100 eV electrons at 100 K (●) and after pre-deposition of O_2 (□). Irradiation time = 400 s; O_2 dose = ~4 × 10^{15} molecules/cm^2 at 120 K. B) Irradiated: Integrated portions of 1 ML H_2O TPD from TiO_2(110) vs. annealing temperature after irradiation with 100 eV electrons at 100 K : 320 – 360 K reflects shift of the ML peak to higher temperature (●), 400 – 630 K reflects area of the OH recombinative peak (◇), 400 - 630 K* reflects the 400 - 630 K data that has been inverted and normalized to the 320 - 360 K data (+). Irradiation time = ~300 s. Procedures for taking data in A) and B) are described in text.

film on the TiO_2(110) surface at 100 K. The final temperature of the TPD measurements or annealing temperature was set incremently higher within the 300 - 800 K temperature range. After each TPD measurement, a 1 ML H_2O film was re-deposited at 100 K, and the H_2O TPD was measured to the next higher temperature. As for the O_2 pre-dosed data (open squares), ~$4x10^{15}$ molecules/cm^2 of O_2 were pre-dosed on the TiO_2(110) at 120 K, 1 ML H_2O was deposited on the surface at 100 K, then followed by identical TPD measurement and H_2O re-deposition cycles. As the annealing temperature increases, the amount of water in the shifted ML peak in both experiments begins to decrease at ~500 K, and by 600 K the state in each case has virtually returned to its initial (unaffected) position. During these experiments, no O_2 desorption is observed in the temperature range from 500 to 800 K. If the ML peak shift to higher temperatures is due to O_{Ti} adatoms deposited onto Ti^{+4} rows, the fate of these atoms during the annealing experiments remains unclear. Our detection arrangement using an integrating cup attached to the QMS does not allow measurement of reactive species such as O atoms.

In addition to the ML peak reverting toward its initial peak position typical of a sputtered and annealed surface, the OH recombinative peak increases within the equivalent annealing temperature range. This result is plotted as the open diamonds labeled *400 - 630 K* in Figure 7.3(b). These data points were taken by subtracting the non-irradiated from the irradiated TPD spectra then integrating the difference in the 400 - 630 K range reflecting the change in signal intensity of the OH recombinative desorption state. For this series of experiments, an irradiation/re-dose water/measure TPD cycle was performed for each point due to the OH recombinative peak desorbing within the annealing temperature range (400 – 800 K). This is opposed to a single irradiation

followed by multiple re-dose water/measure TPD cycles to determine the integrated change in signal intensity over 320 – 360 K due to the ML peak shift which is below the annealing temperature range (400 – 800 K). The amount of water in the OH recombinative peak begins to increase at 500 K and continues past 700 K as the annealing temperature is increased. This transition occurs concurrently with the ML peak shift to its initial position. To facilitate the comparison, the OH recombinative peak integrals (*400 - 630 K**, crosses) have been inverted and normalized to the shifted ML integrals (*320 – 360 K*, filled circles) at 400 K in Figure 7.3(b). When the OH recombinative peak is low, few BBO hydroxyls are present reflecting a surface that is oxidized. During this oxidized state of the surface, the ML peak has shifted to higher temperatures. As the annealing temperature increases through the 500 - 600 K transition, the hydroxyl concentration increases or the surface reduces. At these temperatures the ML peak shifts back to its initial position. The results presented in Figures 7.2 and 7.3 indicate that electron irradiation of monolayer films of water are identical to O_2 pre-dosing experiments which induce a shift in the ML peak and oxidation of the TiO_2(110) surface. Additionally, the shift in the ML peak and the oxidative state of the surface are restored to the initial condition upon annealing to 600 K.

7.2.3 Water coverage dependence

The electron-stimulated reactions in thin water films depend on the water coverage and the electron fluence, providing valuable insights into the reaction mechanisms. As mentioned above, integration of the difference from 320 to 360 K yields

the relative changes in the amount of water in the ML peak shift; likewise for the OH recombinative peak from 400 to 630 K. In Figure 7.4, the ML peak shift integral (*320-360 K*, filled squares) and the OH recombinative peak integral (*400 - 630 K*, open circles) are plotted as a function of the irradiated H_2O coverage under low electron fluence on the

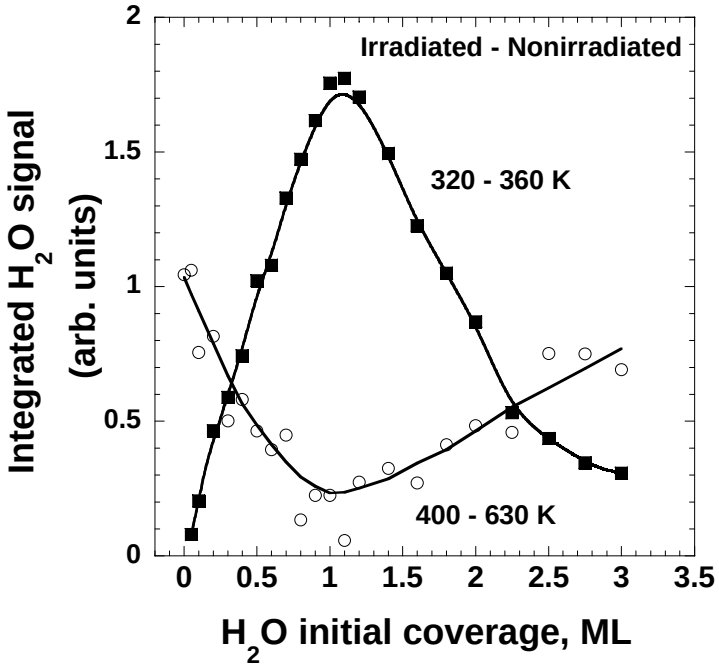

Figure 7.4 ML peak shift integral (320 - 360 K, ■) and 500 K H_2O TPD peak integral (400 - 630 K, ○) vs coverage of initially irradiated H_2O at low electron fluence (N=80). Procedure for taking data is described in text.

annealed TiO_2(110) surface. Due to the decrease of BBO hydroxyls upon oxidation of the surface, the OH recombinative integral is negative; therefore, the *400 - 630 K* data have been shifted to positive values for facile comparison to the *320 - 360 K* data. To acquire the data in Figure 7.4, the TiO_2(110) surface was first exposed to H_2O (0.5 ML) at 400 K to convert all BBO vacancies to hydroxyl groups. Then the H_2O film was deposited where deposition temperature varied with film thickness: 190 K (0 – 1 ML);

150 K (1.1 – 2 ML) and 120 K (2.1 – 8 ML). The procedure insures defect free H_2O films by increasing the mobility and reactivity of the H_2O prior to irradiation. After depositing the H_2O film, it was irradiated with 100 eV electrons (~$6.4x10^{15}$ e^-/cm^2) at the last deposition temperature 190 K (0 – 1 ML); 150 K (1.1 – 2 ML) and 120 K (2.1 – 8 ML), respectively. The low electron fluence was used to minimize effects due to electron stimulated sputtering of H_2O. After electron irradiation, the post-irradiated water was removed by heating to 400 K where a subsequent 1 ML H_2O film was re-deposited at 100 K. The integrals from the TPD spectrum of the newly deposited 1 ML H_2O film are plotted in Figure 7.4.

When no water is irradiated (H_2O coverage = 0), the TPD spectrum is characteristic of water desorbing from the annealed surface. The ML peak has not shifted (320 – 360 integral is low) and all the surface hydroxyls desorb as water in the OH recombinative peak (400 – 630 K integral is high). During oxidation of the surface, the ML peak shifts to higher temperatures and the OH recombinative peak decreases as depicted in Figure 7.2. These electron induced effects in the TPD occur as the coverage of the irradiated H_2O film is increased from 0 to 1 ML. However, at a H_2O coverage of 1 ML, the ML peak shift integral reaches a maximum, and the OH recombinative peak integral lowers to a minimum. As the irradiated H_2O coverage is increased from 1 to 3 ML the electron induced effects begin to reverse where the ML peak shifts toward its original position and the OH recombinative peak integral increases. Since the effects of electron irradiated water on the TPD spectrum are indicative of oxidation of the surface, the oxidation process is related to the amount of water present during irradiation. Irradiation induced oxidation of the TiO_2(110) surface is optimal when water has filled

the Ti^{+4} rows (1 ML) and is suppressed when additional water adsorbs on the BBO sites (1 - 3 ML). The results in Figure 7.4 suggest that all the water molecules within the first monolayer are targets for the initial excitation.

7.2.4 Electron fluence dependence

To examine the dependence of the electron-stimulated surface oxidation on electron fluence, 1 ML water films were irradiated and changes in the post-irradiation water TPD spectra were used to monitor the oxidation of the substrate as a function of the electron fluence. For these experiments, a 1 ML H_2O film was irradiated for a variable duration of time, the water was removed by heating to 400 K, a 1 ML coverage of H_2O was re-dosed, and followed by a TPD measurement. Changes in the integrals from this TPD measurement are plotted as a function of low electron fluence ($< 2x10^{16}$ e^-/cm^2) in Figure 7.5(a) where the second ML peak integral (*170 - 225 K*), the ML peak shift integral (*320 - 360 K*), and the OH recombinative peak integral (*400 - 630 K*) are represented. As the irradiation time increases, the ML peak begins to shift to higher temperature (the *320 - 360 K* integral increases), and the OH recombinative peak integral decreases immediately upon irradiation and continues through 150 s of irradiation. This is not the case for the second ML peak integral where the amount of water in this feature (*170 - 225 K* integrals) remains unchanged through 140 s of irradiation where it then begins to increase. These data suggest that the electron induced effects on the ML and OH recombinative peaks are related as mentioned above, but are not directly correlated to those affecting the second ML peak at 200 K (*170 - 225 K* integrals).

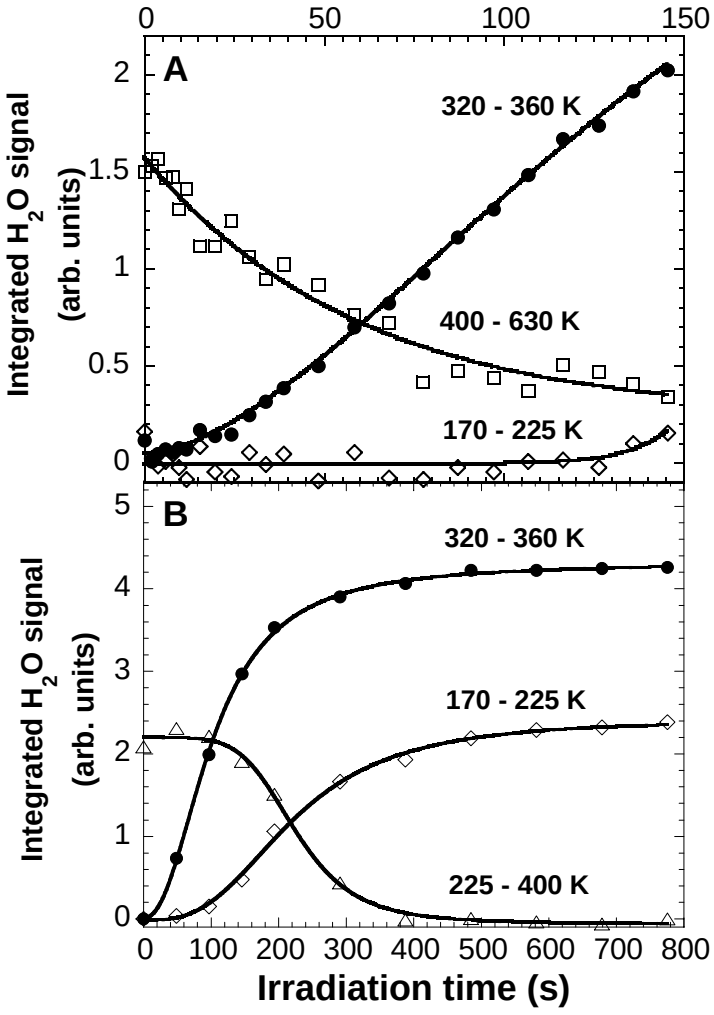

Figure 7.5 A) The ML H_2O peak shift integral (320 - 360 K, ●), OH recombinative peak integral (400 - 630 K, □), and second ML peak integral (170 - 225 K, ◇) from 1 ML coverage of H_2O at 100 K vs. 100 eV electron irradiation time (low fluence). B) The ML peak shift integral (320 - 360 K, ●), second ML peak integral (170 - 225 K, ◇), and entire ML peak integral (225 - 400 K, △) from 1 ML coverage of H_2O at 100 K vs. 100 eV electron irradiation time (high fluence). Procedure for taking data in A) and B) is described in text.

As in Figure 7.5(a), the second ML peak integrals (*170 - 225 K*) and the ML peak shift integrals (*320 - 360 K*) are plotted in Figure 7.5(b) along with the total ML peak integrals (*225 - 400 K*). For this plot, the irradiation time duration is extended to 800 s (~$6x10^{16}$ e^-/cm^2). From the figure, the changes in the second ML peak integral and the ML peak integral are inversely related after an induction time. For the experimental conditions of Figure 7.5(b), this occurs at approximately 100 s of irradiation followed by reaching a saturation level near 400 s. Since the total ML peak integral (*225 - 400 K*) corresponds to the full amount of water in the ML TPD peak, a reduction of this integral implies that less water is required to saturate the ML TPD feature. The excess water seems to be added to the second ML TPD peak inducing an increase in the corresponding integral (*170 - 225 K*). Based on its temperature, the excess water could simply correspond to water desorbing from the BBO rows. However, it is also possible that the water could be desorbing from regions of the surface covered by electron-stimulated reaction products which are not desorbed by heating to 425 K. The results depicted in Figure 7.5 indicate that the ML peak shift integral (*320 - 360 K*) is correlated with variations in the OH recombinative peak integral (*400 - 630 K*), and the amount of water in the second ML peak integral (*170 - 225 K*) and total ML peak integral (*225 - 400 K*) are inversely correlated.

7.2.5 Initial OH concentration

Since electron irradiation of bare TiO_2(110) reduces the surface by creating additional BBO vacancies, it can be used to explore how the electron-stimulated reactions

in thin water films depend on the initial BBO vacancy concentration. The initial hydroxyl concentration can be increased by pre-irradiating the bare TiO_2(110) surface with electrons above ~ 33 eV which induces BBO vacancies via desorption of O^+ by the Knotek-Feibelman mechanism [122, 123]. Electron induced BBO vacancies are similar to those created by thermal annealing [124]; therefore, the subsequent deposition of water reacts with the newly created BBO vacancy site which increases the BB OH concentration compared to the annealed TiO_2(110) surface [125]. The TPD spectra from 1 ML coverages of H_2O as a function of irradiation time (0 – 400 s) from the A) pre-irradiated and the B) annealed TiO_2 surfaces are shown in Figure 7.6. Prior to depositing H_2O, the bare TiO_2(110) surface in Figure 7.6(a) was simply annealed; however, the bare TiO_2(110) surface in Figure 7.6(b) was pre-irradiated with electrons (~$1.2x10^{17}$ e^-/cm^2). For each experiment, the H_2O film was prepared by dosing 0.5 ML of H_2O at 400 K to insure all oxygen vacancies reacted with H_2O prior to depositing the 1 ML H_2O film at 100 K. The TPD spectra in Figure 7.6(a) and (b) were obtained by irradiating the H_2O films for 0, 100, 200, and 400 s corresponding to electron fluences of 0, 0.8, 1.6, and $3.2x10^{16}$ e^-/cm^2, respectively. The irradiated water was removed by heating to 400 K, and a 1 ML H_2O film was re-dosed. The TPD spectra of the re-dosed H_2O films are plotted in Figure 7.6(a) and (b). When the water films were not irradiated, the ML peak position from the pre-irradiated TiO_2 surface in Figure 7.6(a) shifted to lower temperature relative to the peak position from the annealed surface in Figure 7.6(b) indicated by the vertical dashed line. Additionally when water was not irradiated, the increased surface hydroxyl concentration is apparent in the OH recombinative peak of the pre-irradiated

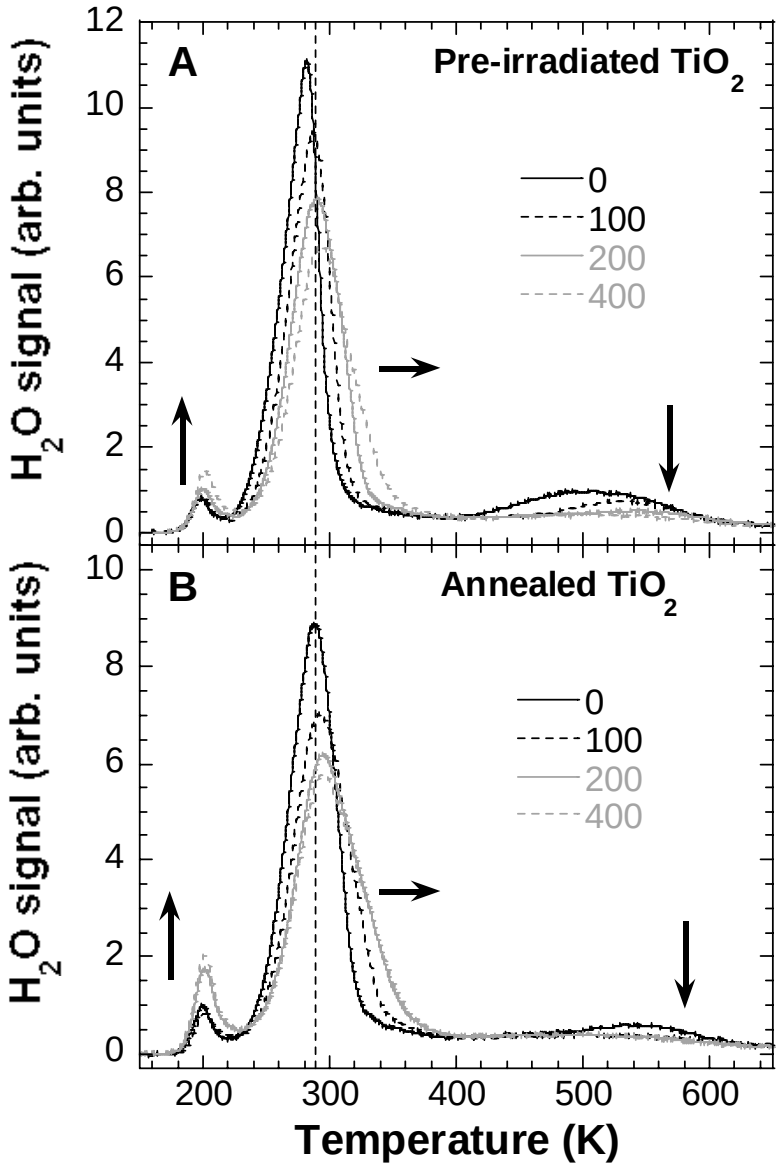

Figure 7.6 TPD spectra of irradiated 1 ML H_2O films from A) a pre-irradiated and B) an annealed TiO_2(110) surface. For A), the bare TiO_2 was pre-irradiated with 100 eV electrons (~1.2×10^{17} e^-/cm^2) at 100K, then the surface was hydroxylated (0.5 ML H_2O dosed at 400K) and 1.0 ML H_2O was dosed at 100 K. The H_2O film was irradiated (0, 100, 200, and 400 s), water was removed by annealing to 400 K, and 1 ML H_2O was re-dosed, which the TPD is shown in the figure. For B), similar experiment, but without pre-irradiation of the TiO_2.

TPD spectrum which is significantly larger than the OH recombinative peak from the annealed spectrum. Since the shift in the ML peak to lower temperature occurred without irradiating water, it can not be a result of electron dissociated water fragments and must be dependent on the BB OH concentration.

As electron irradiation fluence upon the 1 ML H_2O film is increased from 0 to 400 s, the ML peak shifts to higher temperature. After 400 s of irradiation, the ML peak position from the pre-irradiation surface has not shifted more than that from the annealed surface. In fact, the amount that the ML peak shifted due to 400 s of irradiation from the pre-irradiated and annealed surfaces is equivalent. Although the initial starting conditions (hydroxyl concentrations) are different, the rate that the ML peak shifts due to irradiating water is constant for both pre-irradiated and annealed surfaces. This result implies that the initiation of the electron-induced oxidation process is independent of hydroxyl-H_2O complexes where all the water molecules in the monolayer film (Ti^{+4} rows) are targets.

In Figure 7.6, the second ML peak at 200 K increases as a function of irradiation time. This increase seems to be dependent on the surface hydroxyl concentration where the second ML peak increases after irradiating water for 400 s on the pre-irradiated surface, but only 200 s on the annealed surface. Since a constant 1 ML (5.2×10^{14} molecules/cm^2) of H_2O is deposited on the surface for each experiment, an increase in the second ML peak implies that the first ML peak saturation requires less H_2O. Accordingly, the amount of H_2O deposited in the monolayer is dependent on the irradiation time and the initial hydroxyl concentration suggesting that some water adsorption sites in the Ti^{+4} rows are blocked.

The results presented so far suggest the following sequence of events when thin water films are irradiated: Energetic electrons excite water molecules adsorbed on the Ti^{+4} rows, which can subsequently desorb or dissociate. Any water molecule in the Ti^{+4} row is a target for electron-stimulated dissociation, but coverages above 1 ML suppress the electron-stimulated oxidation of the substrate (Figure 7.4). The dominant channel for dissociation leads to desorption of a hydrogen atom (Figure 7.1) leaving a hydroxyl on the Ti^{+4} row, OH_{Ti}, that can react with OH_{BB} to form water adsorbed on the Ti^{+4} row and heal an oxygen vacancy associated with the two OH_{BB} (inset of Figure 7.2 and Figure 7.5(a)):

$$2OH_{Ti} + 2OH_{BB} + BBO_V \rightarrow 2H_2O_{Ti} + BBO \quad (5.3)$$

Note that this reaction should be energetically favorable since the reverse reaction corresponds to the dissociative adsorption of water at a regular (i.e. non-defect) Ti^{+4} site, which is not observed experimentally. Once the BBO vacancies are healed, reaction products begin to accumulate in the Ti^{+4} rows, blocking sites there and causing a decrease in the ML peak intensity (Figure 7.5(a)) and an increase in the 2nd ML peak (Figure 7.5(b)). The fluence at which the BBO vacancies are healed and the 2nd ML peak begins to increase depends on the initial BBO concentration (i.e. BB OH concentration after water deposition, Figure 7.6). Heating the surface above ~ 600 K regenerates BBO vacancies (Figure 7.3).

7.2.6 O_2 ESD at high electron fluences

When the H_2O monolayer covered TiO_2 (110) surface was initially irradiated at low fluence with 100 eV electrons, the ESD yield of O_2 was essentially zero as shown in Figure 7.1. However at higher electron fluences, the yield of O_2 is non-zero suggesting that production of O_2 is a multi-step process. This is expected since the electron stimulated production of molecular oxygen from water ice is precursor mediated [13, 117, 126]. The O_2 ESD yields from a 1.5 ML film of H_2O from TiO_2(110) surfaces prepared with varying concentrations of BB OH's produced from electron induced BBO vacancies are plotted in Figure 7.7. The amount of irradiation in seconds used to create BBO vacancies on the bare surface is denoted by N where the O_2 ESD yield from the annealed surface is labeled N = 0. The O_2 yield from the annealed TiO_2 surface has an appearance threshold at ~ 140 s increasing at a constant rate until the electron irradiation is terminated at 480 s. When the annealed TiO_2 (110) surface is pre-irradiated with 100 eV electrons, the appearance threshold for the ESD O_2 yield shifts to higher irradiation times as a function of the pre-irradiation electron dose. However, the rate of O_2 production remains constant. As mentioned previously, the pre-irradiation electron dose on the bare surface increases the BBO vacancy defects. Subsequently, this increases the surface hydroxyl concentration upon reaction with H_2O. In this experiment, the threshold of the O_2 ESD yield as a function of electron fluence is dependent on the initial hydroxyl concentration on the BBOs implying that the O_2 ESD precursor interacts with the

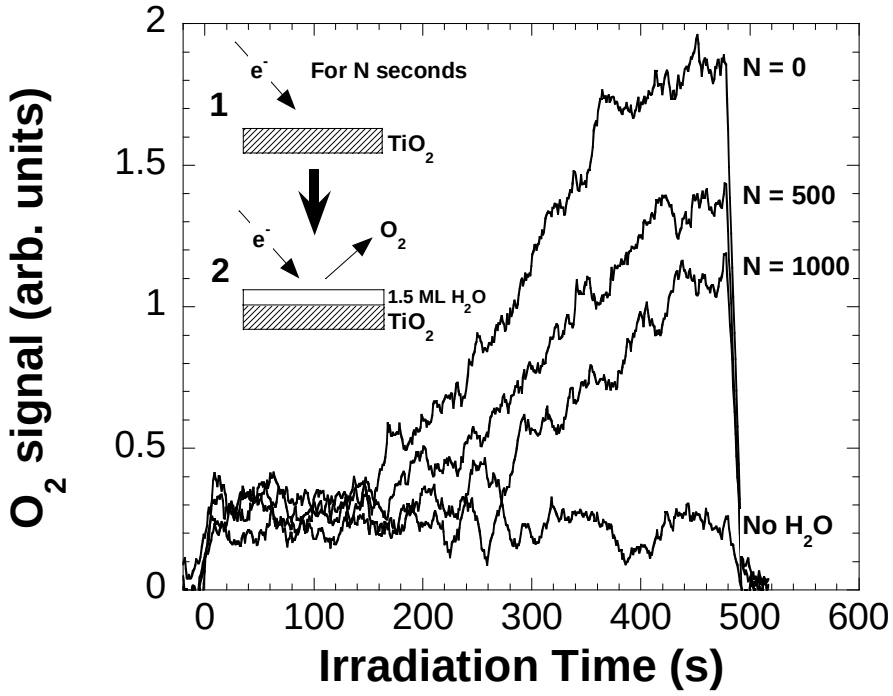

Figure 7.7 O_2 ESD yields from a 1.5 ML H_2O film on TiO_2(110) at 100 K vs 100 eV electron irradiation time for three initial surface conditions. The bare surface was pre-irradiated with N = 0 (annealed), 500, and 1000 where irradiation of the bare surface increases the BB OH concentration after reacting with H_2O. Procedure for taking data is described in text. Irradiation without the 1.5 ML H_2O film (No H_2O) was performed for comparison.

hydroxyls. Under the experimental parameters in Figure 7.7, the higher the surface hydroxyl concentration, the more delayed in time is the O_2 ESD threshold and the lower the O_2 ESD yield after 500 s of irradiation. These experiments indicate that hydroxyl groups inhibit O_2 ESD by reacting with the O_2 precursors. Only after titration of the BB OH groups does O_2 significantly desorb.

The O_2 ESD yield is a function of the precursor concentration on the surface and illustrates their creation and build up until a steady state is reached. A similar trend can be found in the second ML peak integral (*170 - 235 K*) versus electron fluence. Figure 7.8 depicts the relationship between the O_2 ESD yield from the annealed TiO_2(110)

surface and the integral of the second ML peak (similar to data plotted in Figure 7.5(b)) as a function of electron fluence. In Figure 7.8, the O_2 ESD yield and the second ML integrals were measured during 7 cycles of 100 s electron irradiation periods. A 1 ML H_2O film was deposited on the annealed surface and irradiated with 100 eV electrons for

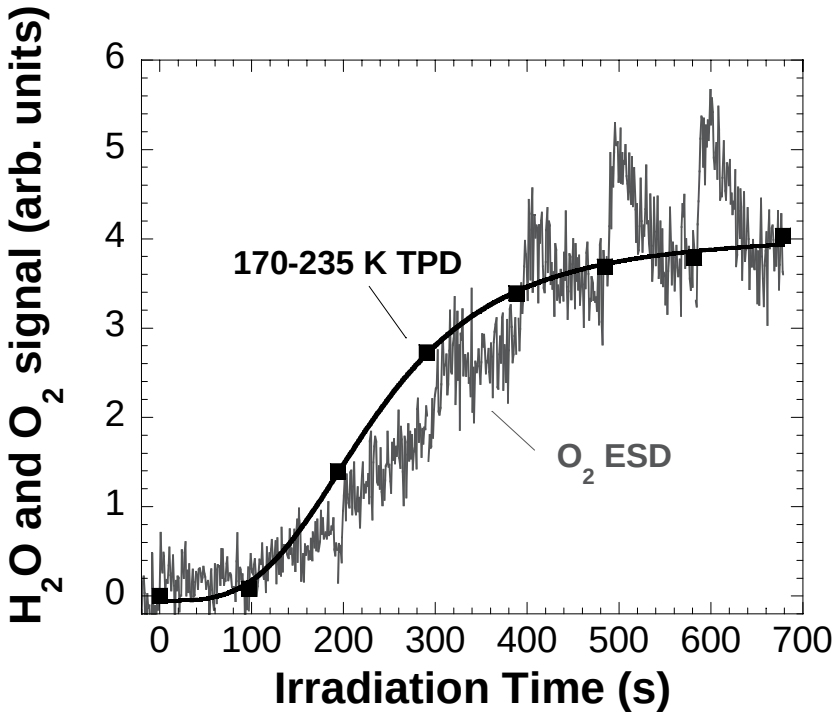

Figure 7.8 The O_2 ESD yields from 1 ML of H_2O adsorbed on an annealed $TiO_2(110)$ surface (gray) compared to the second ML peak integral of the post-irradiation 1 ML H_2O TPD spectra (170 – 235 K, ■) as a function of irradiation time. The figure compares the trends in H_2O adsorption site blocking of the first ML with the electron stimulated production of O_2. Details of the comparison and the experimental procedure are described in text.

100 s (0.8×10^{16} e^-/cm^2) where the O_2 ESD signal was monitored. After the electron dose, the irradiated water was desorbed up to 400 K, a new 1 ML H_2O film was re-deposited, followed by measurement of the amount water in the second ML peak by TPD to 400 K. These cycles were continued until the total irradiation time reached 700 s (5.6×10^{16} e^-

/cm^2). The resultant data in Figure 7.8 is the accumulation of the TPD and ESD measurements in each cycle. Since we are depositing a constant amount of H_2O onto the surface during each cycle, the integral of the second ML peak is indicative of the blocking of sites in the Ti^{+4} rows (ML TPD state) by species produced during irradiation.

7.3 Discussion

On the basis of the results presented above in Figure 7.2 and 7.3(a), we have demonstrated that an irradiated monolayer of H_2O on the TiO_2(110) surface with BBO hydroxyls has similar affects on the TPD spectra of a re-deposited H_2O film as pre-dosing O_2. These changes induced by molecular O_2 on the H_2O TPD spectra comprise of a shift in the ML peak to higher temperature and a decrease in the OH recombinative peak. Observations of the altered features are only present when molecular O_2 reacts with intrinsic surface defects such as BBO vacancy sites or BBO hydroxyls as previously reported [98, 113]. When a 1 ML film of H_2O is co-deposited with O_2, the species produced from the O_2 reaction with the defect sites (O adatoms) interact with the neighboring H_2O molecules and subsequently affect the H_2O TPD spectrum [98, 113]. This is an interesting observation prompting molecular dynamics and density functional theory calculations for the production feasibility and the stability of the intermediate oxygenated species [127, 128]. Recently, similar experiments on the Pt(111) surface were performed to gain an understanding of how O adatoms from dissociated O_2 as well as H adatoms from H_2 interact with coadsorbed H_2O on the well characterized metal surface [104]. In the presence of O adatoms produced by predosing the Pt(111) surface

with O_2, a new water TPD state was observed from the O adatom interaction with water. The new desorption state was separated by approximately 40 K from the undisturbed ML water TPD peak position. For H_2O coadsorbed with H adatoms, the resultant ML water TPD peak does not shift to higher temperature due to the presence of H adatoms, but a new TPD state evolves at a higher temperature separated by a well defined isosbestic point. In both instances, the O and H adatoms did not induce a shift in the ML H_2O TPD peak but initiated a new TPD feature at higher temperatures. These new TPD peaks arising from atomic O and H interactions with H_2O were also shown to be created when a thin film of H_2O was irradiated with 100 eV electrons. Thus, the electron stimulated dissociation of thin films of H_2O on the Pt(111) and the TiO_2(110) surface compare reasonably well with O_2 pre-deposition experiments. However, the fundamental interactions of the water film with the resultant dissociated H_2O fragments on the Pt(111) and TiO_2 (110) surfaces are quite different.

7.3.1 Electron-initiated oxidation

The induction period prior to the onset of O_2 ESD (Figures 7.7 and 7.8) suggests that more than one reaction step is involved in the production of O_2 (unlike the H atoms, which are produced from the water in a single non-thermal reaction, see Figure 7.1). The electron-stimulated production of O_2 in thicker water films is known to be a multi-step process that involves the creation of stable precursors [13, 117, 126]. In that case, O_2 probably results from a series of reactions involving OH to form H_2O_2 and HO_2 [117, 126, 129]. Irradiation of thin water films on TiO_2(110) results in the production of OH's

in the Ti^{4+} rows, OH_{Ti}. Thus it is reasonable to suppose that reactions among the OH_{Ti}'s could also lead to H_2O_2 and possibly HO_2.

$$2OH_{Ti} \rightarrow (H_2O_2)_{Ti} \tag{5.4}$$

$$OH_{Ti} + (H_2O_2)_{Ti} \rightarrow H_2O + (HO_2)_{Ti} \tag{5.5}$$

In support of this hypothesis, recent DFT calculations suggest that pairs of OH's will react to form H_2O_2 which is bound to Ti^{+4} sites and hydrogen bonded to BBO's [130]. However, some form of spectroscopic measurements of the electron-stimulated reaction products on the surface are needed to confirm this hypothesis.

The observation that the fluence threshold for O_2 ESD is larger for surfaces when the initial vacancy concentration is higher (Figure 7.7) supports the idea that O_2 results from a series of reactions starting with the production of OH's. Since the initially produced OH_{Ti}'s react with the BB OH's to reform water, it is only after all the BB OH's have been eliminated that OH's begin to significantly accumulate in the Ti^{+4} rows. Thus a surface with a higher initial vacancy concentration will need a larger electron fluence to eliminate the BB OH's. Once the BB OH's are gone, each surface is in essentially the same condition independent of the initial vacancy concentration and the rates of OH production, and subsequent reactions to produce O_2 are similar (if the same amount of water is also present). As the OH_{Ti} concentration increases they can react to produce H_2O_2 and/or HO_2 as suggested in equation 5.4 and 5.5. Once H_2O_2 and/or HO_2 are formed, O_2 can then be produced from them directly by another energetic electron [13, 117] or further reactions such as:

$$HO_2 + OH \rightarrow O_2 + H_2O \tag{5.6}$$

The surface oxidation dependence on the irradiated water coverage shown in Figure 7.4 is interesting because it illustrates how the surface oxidation process can be optimized or suppressed due to the amount of H_2O adsorbed on the BBO sites. These observations suggest that irradiation induced oxidation of the $TiO_2(110)$ surface is optimal when the full monolayer of H_2O is irradiated. Since the BBO hydroxyl concentration is constant for all data points in Figure 7.4, the results further support the conclusion that each water molecule in the Ti^{+4} rows is a potential target for dissociation. Furthermore if the entire H_2O monolayer is needed to induce the most oxidation, the H_2O target molecule must be near the BBO hydroxyl prior to dissociation and the mobility or diffusion of the OH_{Ti} species along the Ti^{+4} row is negligible. When H_2O is added to the BBO sites (the 2^{nd} monolayer) of the irradiated film, the added water must interact with the BBO hydroxyls to inhibit the surface oxidative reactions. Additionally, the oxidation process can be compensated by electron induced reduction of the surface originating from the irradiated H_2O on the BBO sites that creates BB OH's. The inhibition of the $TiO_2(110)$ surface oxidation by addition of the 2^{nd} ML of the irradiated water film could include a direct reaction with the reactive OH_{Ti} and the H_2O on the BBO sites or stabilization/protection of the BB OH's through hydrogen bonding with H_2O on the BBO sites. Initial experiments suggest the lower probability of excitation localization on H_2O in the Ti^{+4} sites in the presence of H_2O adsorbed on the BBO sites. This particular issue will be addressed in more detail in Chapter 8.

For many of the proposed photocatalytic applications of $TiO_2(110)$, the initial excitations occur in the substrate with energy subsequently being transferred to adsorbates to drive the desired chemistry. The results presented here for the electron-

stimulated reactions in adsorbed water do not directly address the nature of the electronic excitations which initiate the non-thermal chemistry. However, we believe that neutral electronic excitations of the water molecules (generated by a direct electron-impact excitation, electron detachment from a transient H_2O^-, or by ionization of water molecules followed by electron-ion recombination) are primarily responsible for the observed non-thermal chemistry.

Independent of the precise excitation pathway, the ESD results presented in Figure 7.1 indicate that, upon irradiation, excited water molecules can promptly dissociate resulting in desorption of both H and H_2. In the gas phase, most of the lowest energy, electronically excited states of neutral water molecules are dissociative [131, 132]. For example, the first electronically excited state is purely dissociative along the H-OH bond [133, 134]. Irradiation of amorphous solid water (ASW) and crystalline ice (CI) with energetic electrons also results in H and H_2 ESD. Therefore, it is not surprising that electronically excited water molecules adsorbed on the TiO_2(110) surface also dissociate leading to desorption of atomic and molecular hydrogen. In particular for the first monolayer, water apparently binds to the Ti^{+4} ions through the oxygen lone electron pairs with the hydrogen atoms pointing away from the surface [135]. This geometry should be well-suited for desorption of one (or both) of the hydrogen atoms. Since desorption of a (light) H atom will not give a large impulse to the OH fragment, we should expect the OH to remain bound to the Ti site, as the results presented here indicate. Once the initial OH's are formed on Ti^{+4} rows, the subsequent chemistry is remarkably similar to that observed when water and oxygen are co-deposited on TiO_2(110) since that chemistry also proceeds through the formation of OH's.

7.4 Conclusions

We have investigated the electron-stimulated oxidation of the TiO_2 (110) surface by irradiating an adsorbed monolayer of H_2O with 100 eV electrons. Utilizing the TPD spectra of H_2O as a quantitative tool for monitoring the oxidative state of the surface, the irradiation of water films ($\theta < 3$ ML) produced similar affects on the H_2O TPD spectra as depositing molecular O_2 prior to H_2O. Initially, electron-irradiation results primarily in desorption of H and H_2O, along with some H_2. After prolonged irradiation, O_2 ESD also becomes significant. Desorption of atomic hydrogen from water bound to the Ti^{+4} sites leaves OH's which oxidize the surface and are responsible for most of the subsequent chemistry. Each H_2O molecule adsorbed in the Ti^{+4} rows seems to be a target for the incoming electron, thus initiating the oxidation of the TiO_2 surface. However, water coverages greater than 1 ML limited the oxidation process.

CHAPTER 8

ELECTRON–STIMULATED SPUTTERING OF THIN FILMS OF WATER ON THE TITANIUM DIOXIDE(110) SURFACE

8.1 Introduction

The results presented in Chapter 7 pertained to the electron-stimulated production of reactive species that react directly with the TiO_2(110) surface. This chapter describes the electron-stimulated removal of water while the surface oxidation reaction is taking place. A review of the sputtering of water ice by a range of energetic particles at variable irradiation temperature and ice film growth temperature has been published [136]. Electron-stimulated sputtering of thin ASW films (~50 ML) has been performed on the Pt(111) surface [137]. In this case, the reactions at both the water/vacuum and the water/Pt interface govern much of the removal of water which was observed by the strong dependence of the sputtering yield on the water film thickness. At ~2 ML water coverages on the Pt(111) surface, the water is too thin for energy deposition into the water bulk. Therefore, reactions at the water/Pt interface were minimized, but sputtering was mediated by electron trapping preferentially at the water/vacuum interface [104].

Below, the total amount of water sputtered from the surface is measured by integration of TPD spectra before and after electron irradiation. These results are compared with the ESD measurements which accounts only for the non-dissociative water desorption. Possible mechanisms are suggested that take into consideration the dependency of the sputtering and ESD yields on the water coverage ($\theta < 2$ ML). The

ESD yields of molecular hydrogen as a function of coverage are also described and related to the proposed mechanisms.

8.2 Results

8.2.1 Sputtering of H_2O

Inelastic electron interactions with adsorbed water induce a variety of non-thermal reactions that result in desorption of molecular water and dissociated fragment neutrals and ions. The total removal of water or sputtering includes molecular desorption and all of the dissociative desorption channels. When irradiating a 2 ML film of water on the TiO_2(110) surface with 100 eV electrons, there is a surprising difference in the sputtering rates of H_2O from the Ti^{+4} and BBO adsorption sites. Figure 8.1 shows the H_2O TPD spectra as a function of irradiation time (0 – 600 s). The amount of H_2O removed from the BBO peak at 200 K occurs at a greater rate (requiring less electrons) compared to the H_2O removed from the Ti^{+4} peak at 290 K. For experiments in this figure, the 2 ML H_2O film was deposited and irradiated at 100 K, where a second of irradiation corresponds to 1.1×10^{13} e^-/cm^2 and the total electron fluence at 600 s equals 6.5×10^{15} e^-/cm^2. The inset of Figure 8.1, depicts the integrated amount of the H_2O in the Ti^{+4} and BBO peaks versus increasing electron irradiation time. It is clear that the rate of H_2O sputtering is not only different between the two adsorption sites, but H_2O is exponentially removed from the BBO sites compared to the Ti^{+4} sites which has a linear rate of removal. From the first

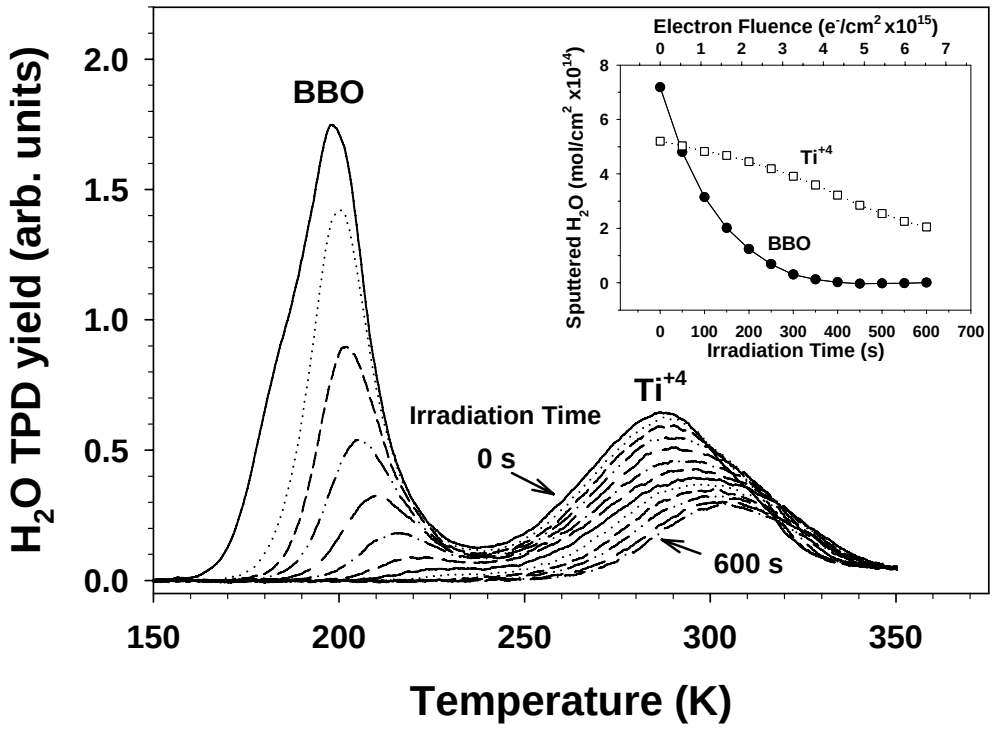

Figure 8.1 TPD spectra of a 2 ML film as a function of irradiation time with 100 eV electrons. The first ML (Ti^{+4}; $5.2x10^{14}$ molecules/cm^2) and second ML (BBO) are labeled. The inset depicts the integrated amount of H_2O in each peak versus irradiation time. (600 s = $6.5x10^{15}$ e^-/cm^2)

50 s of irradiation, ~0.03 H_2O mol/e^- is sputtered from the Ti^{+4} rows compared to ~0.43 H_2O mol/e^- from the BBO sites. During the first irradiation period of 50 s, the difference is more than an order of magnitude. Under similar conditions (irradiation of a 100 K H_2O film with 87 eV electrons) a constant sputtering rate of ~1.7 H_2O molecules/e^- was measured [137]. However, this measurement was taken from the multilayer (23.4 ML) on Pt(111) where a maximum in the sputtering rate was observed and attributed to dissociative losses via a maximum in D_2 and O_2 production at the D_2O/Pt interface [103, 137, 138].

8.2.2 ESD of H_2O

During electron irradiation, sputtered H_2O can possibly re-adsorb on the surface. Since the binding energy of H_2O with Ti^{+4} sites is higher than with the BBO sites, the post sputtered H_2O can preferentially re-adsorb to the Ti^{+4} sites. This would increase the amount of H_2O desorbing in the BBO TPD peak, and be a source of error for the sputtering rate from both adsorption sites. To eliminate this possibility, the molecular H_2O ESD yield can be monitored during electron irradiation. The ESD yield of neutral molecular water is the primary pathway for H_2O removal from the surface for less than 2 ML [137] and should reflect the dissimilarity between H_2O desorbing from the Ti^{+4} and the BBO sites. Figure 8.2 depicts the integrated ESD yield of molecular D_2O as a function of the D_2O coverage. For this experiment, the electron fluence was held constant while the D_2O films were deposited and irradiated at 100 K. Deuterated water was employed to eliminate contributions from background H_2O during detection of the water ESD yield. There is a constant rate of D_2O desorption as the D_2O coverage is increased to 1 ML or until the Ti^{+4} sites are saturated with D_2O. However, as D_2O is added to the second ML (BBO sites), the integrated ESD yield of D_2O abruptly increases and continues at a higher rate. The rate of desorption after H_2O has been added to the second ML ($k_{Ti^{+4}}$), is approximately three times the rate for submonolayer coverages (k_{BBO}). In the case for H_2O ESD from the BBO sites, there is no exponential trend in the desorption yield; however this only includes the non-dissociative molecular ESD channel.

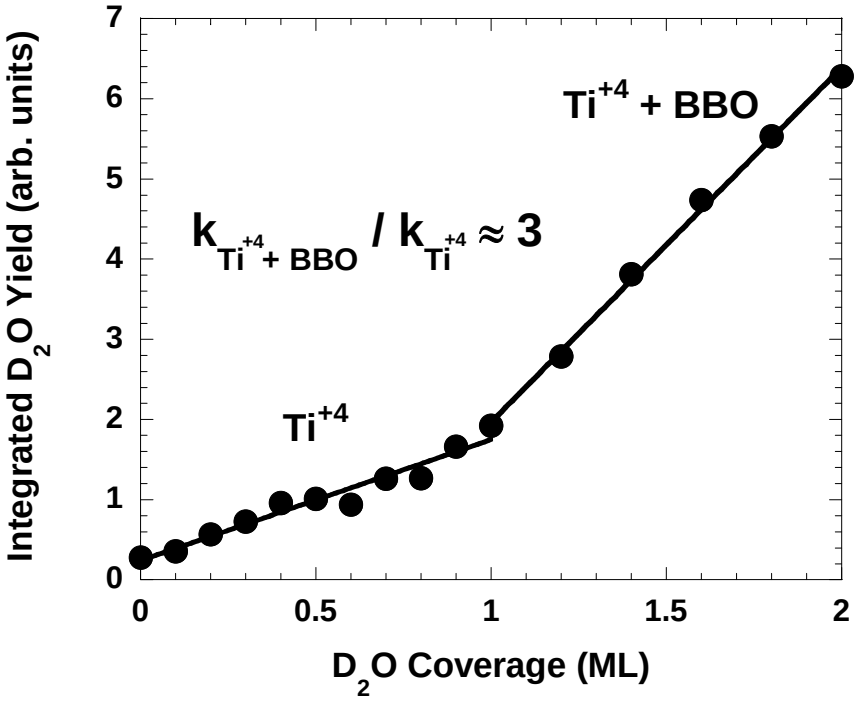

Figure 8.2 Integrated D_2O ESD yield during a constant electron fluence versus D_2O coverage in monolayers.

To develop an understanding of the electron-stimulated sputtering process from each surface site and the multilayer, the D_2O ESD yields were measured from 1 – 4 ML of coverage as a function of incident electron energy. The results are shown in Figure 8.3. The data was obtained by irradiating 1 ML (Ti^{+4}), 2 ML (Ti^{+4} + BBO), 3 ML, and 4 ML D_2O films at 100 K with electrons of the specified energy at a low constant fluence. The low electron fluence limited the total sputtering of the film during the experiment. At 100 eV, the ESD yield of D_2O from the Ti^{+4} + BBO sites is ~6.9 times more than the D_2O ESD yield from the Ti^{+4} sites. The increase in yields at 100 eV is followed by ~1.5 times more from the 3 ML film than the Ti^{+4} + BBO sites and ~0.11 times more from the

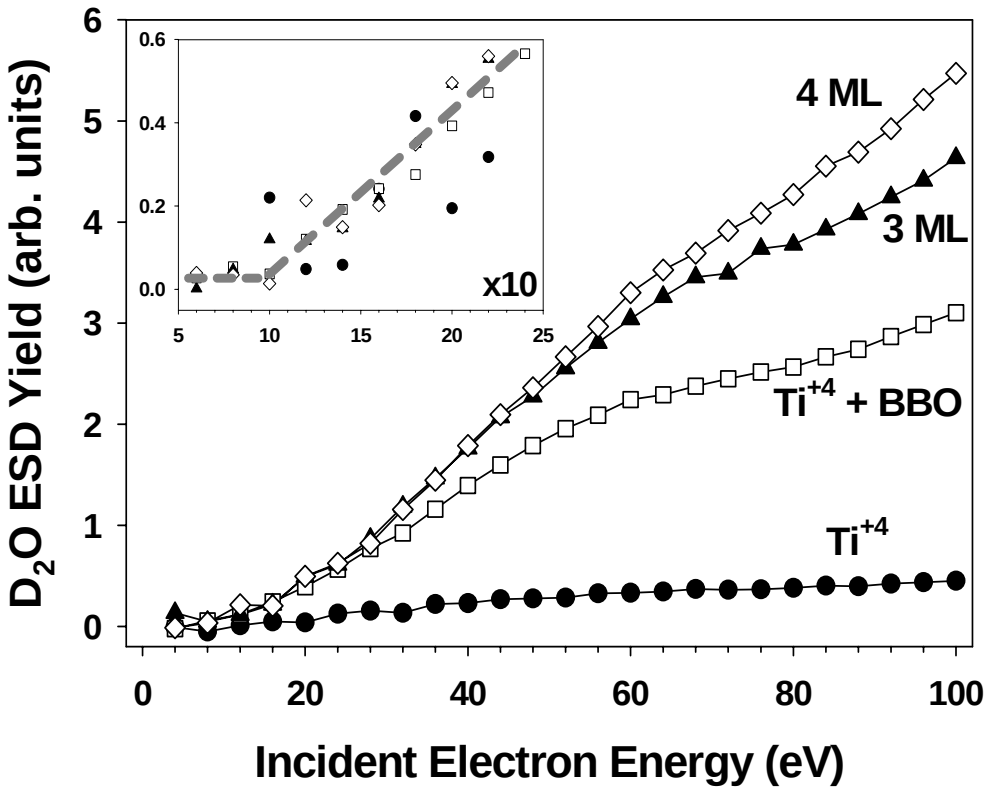

Figure 8.3 The D_2O ESD yields of 1 ML (Ti^{+4}, ●), 2 ML (Ti^{+4} + BBO, □), 3 ML (▲), 4 ML (◇) of D_2O at 100 K versus the incident electron energy. The inset is a zoomed depiction of the low energy threshold region where the ESD yields have been normalized to the 4 ML data at 100 eV.

4 ML film than from the 3 ML film. It is evident from the figure that there is a significant variance in the water ESD yields from the Ti^{+4} sites compared to desorption from the Ti^{+4} + BBO sites. As the multilayer forms, the difference in the D_2O ESD yields is not as sizable. The yield of D_2O desorbing from the BBO sites remains higher than that from the Ti^{+4} sites and is invariant to incident electron energy. However, the threshold for ESD of D_2O from each film is ~10 eV which is depicted in the inset of Figure 8.3. For comparison of the threshold energies, the y-axis has been multiplied by a factor of 10 and the yields were normalized to the 4 ML data at 100 eV. The identical threshold energy for the D_2O films indicates that the electron-stimulated desorption of

neutral molecular water from the films in Figure 8.3 proceeds through a similar process, but the efficiency of the process is dependent on D_2O coverage.

8.3 Discussion

From the data presented in Figures 8.1, 8.2, and 8.3, there is a marked difference in the desorption and sputtering rates of water from the Ti^{+4} and the BBO sites on the TiO_2(110) surface. If the water sputtering were due to direct excitation of the adsorbed water, the rates would correlate with the number of targets or amount of adsorbed water. This would suggest that the amount of water removed from the 2 ML film (Ti^{+4} + BBO sites) would be twice more than the 1 ML film (Ti^{+4}) which is not the case. The sputtering process is not simply dependent on the amount of adsorbed water on the surface, but varies according to the water interactions with neighboring water molecules and the TiO_2 substrate. These interactions include affects on H_2O/TiO_2 electronic structure, hydrogen bonding, and the electron trapping probability as the H_2O coverage is increased. To understand the sputtering process of water on the TiO_2(110) surface, these interactions must be considered.

Besides direct excitations stimulating water desorption, ionization of the water molecules followed by electron-ion recombination can induce desorption [137]. For the case of thin films of H_2O (θ < 2 ML) on the Pt(111) surface, the electron trapping probability was low, but the electrons localized at the water/vacuum interface leading mostly to the direct desorption of molecular water upon the electron-ion recombination event [104]. The trapping probability of electrons at the water/vacuum interface of water

adsorbed on the TiO_2(110) surface could render insights into the difference in sputtering rates. Recently, wet electron or partially solvated electron states have been observed in thin films of water adsorbed on the TiO_2(110) surface using time-resolved two-photon photoemission spectroscopy [100, 139]. These studies were performed on a partially reduced TiO_2(110) surface where an occupied electron level is introduced within the band gap ~0.8 eV below the Fermi level due to missing BBO's [93]. Upon adsorption of H_2O, the defect level persists [99]. From the occupied defect band, electrons were pumped with 3.1 eV photons then probed as the electron solvates in the wet electron state at 2.4 ± 0.1 eV above the Fermi level then decays into the conduction band of the TiO_2 [100]. In Ref. [100], the authors observe a maximum in the wet electron state intensity when a ML coverage of water is adsorbed on the surface. The precise amount of water on the surface present during this experiment may not be known within submonolayer certainty. However to observe the wet electron states, water formed a complex with the BB OH group. To effectively complex all the surface hydroxyls, a monolayer of water or greater must be present. The observation of wet electron states on the TiO_2(110) surface reveals insight into ion-electron recombination mechanism that could be associated with the data in Figures 8.1, 8.2, and 8.3. First, wet electron or partially solvated electron states are present and the probability of electron trapping increases from the submonolayer to the bilayer coverage. Secondly, the threshold for D_2O ESD in the inset of Figure 8.3 is ~10 eV which is roughly the ionization potential of water.

Another possible mechanism that could produce similar results as in Figures 8.1, 8.2, and 8.3 is the thermal energy transfer from electron-hole (e-h) pair recombination events in the near surface region of the substrate. The band gap of rutile TiO_2 is 3.05 eV

[86]. If the band gap energy is dissipated in the first few layers of the substrate as lattice vibrations (phonons) or heat, the adsorbed water on the surface can desorb from either the Ti^{+4} or the BBO sites. The binding energy of water to the Ti^{+4} and the BBO site is 0.74 eV and 0.64 eV, respectively [106]. If water desorbs through this mechanism, the e-h recombination probability in the near surface region would govern the ESD desorption yield of water. In fact as water adsorbs to the TiO_2 surface, the e-h recombination probability increases. This phenomenon is a direct result of the lowering of the valence and conduction band bending due to water adsorption and has been demonstrated on TiO_2 nanoparticles [140] and on the InP(110) surface [141]. The changes in the band bending were monitored with photoluminescence and angle-resolved photoelectron spectroscopy, respectively. At the TiO_2(110) surface, a depletion layer is formed where the valence and conduction bands bend upward in energy. As H_2O adsorbs to the surface, an increase in the luminescence intensity is observed which is a direct measurement of the e-h recombination events [140]. The enhancement in e-h recombinations is due to a decrease in the amount of upward band bending which signifies a lowering in the barrier height and width for the electron in the conduction band to return to the valence band [88]. Thus, the e-h recombination probability increases as that amount of water adsorbed on the TiO_2 surface increases which correlates with the data in Figures 8.1, 8.2, and 8.3. The onset of the H_2O ESD threshold at ~10 eV does not agree with the onset of e-h recombination which would be the band gap of the TiO_2 crystal at 3.05 eV; however, the threshold for e-h processes stimulated by an electron beam usually occurs ~2.5 times the band gap energy [142]. Ref. [142] refers to e-h recombination in alkali-halide crystals, but processes induced by radiation at low fluences should render a similar multiplicative

value of ~2.5 for metal oxides. This places contributions from e-h recombination events to the H_2O ESD yield close to the 10 eV threshold value for H_2O desorption.

8.3.1 ESD of D_2

Along with molecular water, the electron-stimulated desorption of molecular deuterium was monitored as a function of incident electron energy from first and second monolayer coverages of water. The results of this experiment are shown in Figure 8.4. Here, the rate of D_2 desorption is constant from both film coverages as incident electron energy increases, and similar to the water ESD yields of Figure 8.2. In this case, the rate from the 2 ML (Ti^{+4} + BBO) is approximately 3 times the rate of D_2 desorption from the monolayer (Ti^{+4}). The data in Figure 8.4 suggests that there is a similar water coverage dependence affecting the production and desorption of D_2 as for ESD of molecular water. The formation of molecular D_2 proceeds through a dissociative attachment resonance (DEA) or a multiple collision process (e.g., reactive scattering or ion-electron recombination) [43, 116]. From electron irradiation of ASW, molecular D_2 is produced from the $^2B_2$ core-excited negative ion resonance state at ~12.5 eV with another broad feature that begins near 20 eV [43]. The low energy resonance peak at 12.5 eV is not observed in the data of Figure 8.4, but the onset of the higher energy structure is present. The similarity of the ESD yields of D_2 with D_2O could indicate that DEA resonances are involved with the sputtering of water from the TiO_2(110) surface. The decay of transient

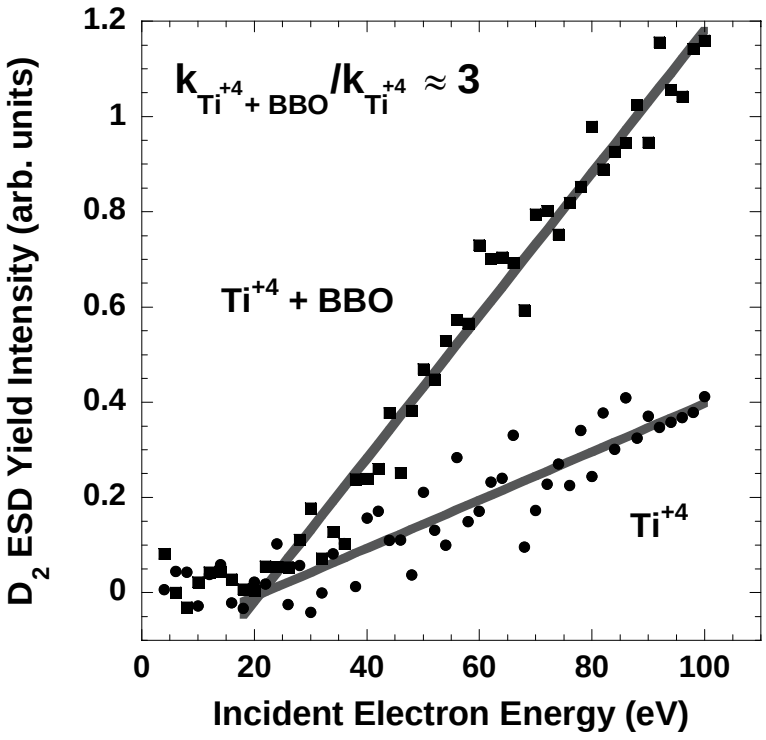

Figure 8.4 D_2 ESD yield as a function of incident electron energy from the monolayer (Ti^{+4} sites) and 2 ML (Ti^{+4} + BBO sites) coverages of D_2O.

negative ion, H_2O^-, via electron autodetachment could result in neutral D_2O desorption contributing to the total water sputtering yield. The desorption of D_2 from D_2O^+ recombination with quasi-free or trapped electrons has been reported [116]. If molecular hydrogen is produced via this mechanism for the case presented above, electron-stimulated sputtering of water from the TiO_2(110) surface would primarily be due to ion electron recombination with possible contributions from substrate e-h recombination events and electron attachment resonances.

8.4 Conclusion

The electron-stimulated desorption and sputtering yields of water from the TiO_2(110) surface have been measured as a function of water coverage. Surprisingly, the amount of water removal within the first irradiation period from the BBO adsorption sites is an order of magnitude more than that from the Ti^{+4} sites. This suggests that the amount of water on the surface ($\theta < 2$ ML) dictates the water sputtering rates. To explain the effects in the sputtering rates, the coverage dependency must be considered. The recombination of ionized water with wet or partially solvated electron states was suggested to be the primary mechanism along with contributions from recombination of substrate electron-hole pairs at the surface or in the near surface region. Both mechanisms are correlated with the amount of water present on the surface. In addition, the possibility of contributions from electron attachment resonances was proposed.

CHAPTER 9

CONCLUSION

A quantitative model of nonthermal chemical reactions at surfaces must account for the effects of charge and energy transfer between the adsorbed molecules and the surface. For example, it is well known that the most efficient mechanism for neutralizing an incident ion or quenching an excited molecule at a short distance from the surface is via resonant charge transfer to the substrate. The probability of charge transfer depends on the overlap of the excited state wave functions and the empty states of the surface. This overlap integral decays exponentially with increasing distance from the surface which is typically on the order of several Å. In condensed molecular films the coupling strength of each individual molecule, the electron target, to the substrate and surrounding media dictates how the energy imparted by the incident electron is dissipated. If dissociation occurs, the outcome of the dissociated fragment species is also affected. In addition, the positions and widths of the energy states associated with the adsorbate, relative to the substrate Fermi level and conduction band positions, are critical.

The clear thread through the results presented above is the variation of adsorbate coupling strengths with coverage which is evident in the ESD experiments. The stability of the TNI, $SiCl_4^-$, decreased upon completion of the second monolayer of $SiCl_4$. This was demonstrated by the increase in the $Cl(^2P_{3/2})$ signal while the Cl^- signal declined. The electron-stimulated sputtering yield of water from the $TiO_2(110)$ is significantly dependent on the water coverage as well. If water removal occurs via ion-electron recombination, the sputtering rate is dictated by the electron trapping probability which is

influenced by the adsorption geometry and overlapping wave functions with the substrate. In the case of electron-stimulated oxidation of the $TiO_2(110)$ surface, the excitation of the H_2O molecules bound to the Ti^{+4} sites initiated the oxidation process; however, water adsorption to the BBO sites limited the oxidation reaction. The results presented here reveal that the adsorbate interactions with the surrounding media dictate the pathway of the chemical reaction toward products whether occurring within non-polar adsorbates on a semiconductor surface or polar adsorbates on a metal oxide surface.

The resonance structure of the nonthermal neutral Cl yields from $SiCl_4$ adsorbed on Si(111) clearly demonstrate that negative ion resonances can be selectively excited and used to carry out energy selective chemical modification of a surface. Chemical reactions due to low energy electrons may not be the dominate mechanism driving plasma chemistry, but reactions specific to the DEA resonance can be selectively induced with monoenergetic electron beams. However, these reactions are dictated by the properties of the DEA resonance as well as de-excitation mechanisms which includes: the energy width of the resonance, the convolution of multiple resonances, curve crossings on the TNI state potential, branching ratios in the product channel, and the autodetachment probability. By selectively exciting a DEA resonance with favorable properties, specific surface reactions can be well controlled which have implications for film growth, surface patterning and masking, and etching. Since the mean free path of electrons at energies near 10 eV is about 10 Å in Si, reactions induced by low-energy electrons should be fairly localized if initiated with a localized electron source.

APPENDIX

Much of the preliminary work that guided experimentation leading to the results presented in Chapter 7 and Chapter 8 were recorded during my visit to PNNL. To obtain a complete description of the chemical system, several more focused experiments were performed by Nikolay Petrik and Gregory Kimmel. I would like to acknowledge their role in data acquisition and state that the results presented in Chapter 7 and Chapter 8 are a product of our collaborative effort.

REFERENCES

1. L. Sanche. Dissociative attachment in electron scattering from condensed molecular oxygen and carbon monoxide. *Phys. Rev. Lett.* **53**, (1984), 1638.

2. L. G. Christophorou and J. K. Olthoff. Electron interactions with plasma processing gases: present status and future needs. *Appl. Surf. Sci.* **192**, (2002), 309.

3. L. Sanche. Interactions of low-energy electrons with atomic and molecular solids. *Scanning Microscopy*. **9**, (1995), 619.

4. A. Chutjian, A. Garscadden and J. M. Wadehra. Electron attachment to molecules at low electron energies. *Phys. Rep.* **264**, (1996), 393.

5. O. Ingolfsson, F. Weik and E. Illenberger. The reactivity of slow electrons with molecules at different degrees of aggregation: gas phase, clusters and condensed phase. *Int. J. Mass Spectrom. Ion Process.* **155**, (1996), 1.

6. L. G. Christophorou, D. L. McCorkle and A. A. Christodoulides. *Electron-molecule interactions and their applications*. Academic Press Inc., Orlando, (1984).

7. A. D. Bass and L. Sanche. Absolute and effective cross-sections for low-energy electron-scattering processes within condensed matter. *Radiat. Environ. Biophys.* **37**, (1998), 243.

8. L. Sanche. Electron resonances in DIET. *Surf. Sci.* **451**, (2000), 82.

9. A. D. Bass and L. Sanche. Dissociative electron attachment and charge transfer in condensed matter. *Radiat. Phys. Chem.* **68**, (2003), 3.

10. A. D. Bass and L. Sanche. Reactions induced by low energy electrons in cryogenic films (Review). *Low Temp. Phys.* **29**, (2003), 202.

11. R. Balog, J. Langer, S. Gohlke, M. Stano, H. Abdoul-Carime and E. Illenberger. Low energy electron driven reactions in free and bound molecules: from unimolecular processes in the gas phase to complex reactions in a condensed environment. *Int. J. Mass Spectrom.* **233**, (2004), 267.

12. R. E. Johnson. Sputtering of ices in the outer Solar system. *Rev. Mod. Phys.* **68**, (1996), 305.

13. M. T. Sieger, W. C. Simpson and T. M. Orlando. Production of O_2 on icy satellites by electronic excitation of low-temperature water ice. *Nature*. **394**, (1998), 554.

14. X. Pan and L. Sanche. Mechanism and site of attack for direct damage to DNA by low-energy electrons. *Phys. Rev. Lett.* **94**, (2005), 198104.

15. L. Sanche. Low energy electron-driven damage in biomolecules. *Eur. Phys. J. D*. **35**, (2005), 367.

16. Q. B. Lu and L. Sanche. Effects of cosmic rays on atmospheric chlorofluorocarbon dissociation and ozone depletion. *Phys. Rev. Lett.* **87**, (2001), 078501.

17. P. Mozejko, B. Zywicka-Mozejko and C. Szmytkowski. Elastic cross-section calculations for electron collisions with XY_4 (X=Si, Ge; Y=H, F, Cl, Br, I) molecules. *Nucl. Instrum. Methods Phys. Res., Sect. B*. **196**, (2002), 245.

18. P. Mozejko, G. Kasperski, C. Szmytkowski, A. Zecca, G. P. Karwasz, L. Del Longo and R. S. Brusa. Absolute total cross-section measurements for electron scattering from silicon tetrachloride, $SiCl_4$, molecules. *Eur. Phys. J. D*. **6**, (1999), 481.

19. R. Basner, M. Gutkin, J. Mahoney, V. Tarnovsky, H. Deutsch and K. Becker. Electron-impact ionization of silicon tetrachloride ($SiCl_4$). *J. Chem. Phys.* **123**, (2005), 54313.

20. M. T. d. N. Varella, A. P. P. Natalense, M. H. F. Bettega and M. A. P. Lima. Low-energy electron scattering by CF_4, CCl_4, $SiCl_4$, $SiBr_4$, and SiI_4. *Phys. Rev. A*. **60**, (1999), 3684.

21. H. X. Wan, J. H. Moore and J. A. Tossell. Electron scattering cross sections and negative ion states of silane and halide derivatives of silane. *J. Chem. Phys.* **91**, (1989), 7340.

22. R. H. Vought. Molecular dissociation by electron bombardment; a study of silicon tetrachloride. *Phys. Rev.* **71**, (1947), 93.

23. C. R. Moylan, S. B. Green and J. I. Brauman. Electron attachment chemistry of tetrachlorosilane. Relevance to plasma reactions. *Int. J. Mass Spectrom. Ion Process.* **96**, (1990), 299.

24. J. L.-F. Wang, J. L. Margrave and J. L. Franklin. Interpretation of dissociative-electron attachment processes for silicon tetrachloride. *J. Chem. Phys.* **61**, (1974), 1357.

25. Y. Baba, K. Yoshii and T. A. Sasaki. Photon-stimulated ion desorption from condensed $SiCl_4$ by resonant excitation at the K-edges. *Surf. Sci.* **341**, (1995), 190.

26. Y. Baba, K. Yoshii and T. A. Sasaki. Desorption of molecular and atomic fragment-ions from solid CCl_4 and $SiCl_4$ by resonant photoexcitation at chlorine K-edge. *Surf. Sci.* **376**, (1997), 330.

27. J.-M. Chen, R. Klauser, S.-C. Yang and C.-R. Wen. Characterization of the electronic structure of $SiCl_4$ probed by X-ray absorption and ion desorption techniques. *Chem. Phys. Lett.* **246**, (1995), 285.

28. J. M. Chen, R. Klauser, S. C. Yang, Y. J. Hsu and S. I. Cheng. Electronic structure, electronic decay, and desorption processes of molecular solid $SiCl_4$ following core-level excitation. *Phys. Rev. B*. **54**, (1996), 1455.

29. J. M. Chen, K. T. Lu and J. M. Lee. State-specific photochemistry of $SiCl_4$ condensed on Si(100) with synchrotron radiation. *J. Chem. Phys.* **118**, (2003), 5087.

30. J. M. Chen and K. T. Lu. State-Specific Enhancement of Cl^+ and Cl^- desorption for $SiCl_4$ adsorbed on a Si(100) surface following Cl 2p and Si 2p core-level excitations. *Phys. Rev. Lett.* **86**, (2001), 3176.

31. Q. Guo, D. Sterratt and E. M. Williams. Chemical selectivity with ESD of chlorinated silicon species. *Surf. Sci.* **357-358**, (1996), 402.

32. Q. Guo, D. Sterratt and E. M. Williams. Negative ion formation from $SiCl_4$ adsorbed on Si(100). *Surf. Sci.* **352-354**, (1996), 327.

33. T. A. Carlson, A. Fahlman, M. O. Krause, T. A. Whitley, F. A. Grimm, M. N. Piancastelli and J. W. Taylor. Angle-resolved photoelectron spectroscopy of the valence orbitals of tetrachlorosilane as a function of photon energy from 14 to 80 eV. *J. Chem. Phys.* **84**, (1986), 641.

34. J. C. Green, M. L. H. Green, P. J. Joachim, A. F. Orchard and D. W. Turner. Study of the bonding in the Group IV tetrahalides by photoelectron spectroscopy. *Phil. Trans. R. Soc. London, Ser. A*. **268**, (1970), 111.

35. J. D. Bozek, K. H. Tan, G. M. Bancroft and J. S. Tse. High resolution gas phase photoabsorption spectra of tetrachlorosilane and tetramethylsilane at the silicon L edges: characterization and assignment of resonances. *Chem. Phys. Lett.* **138**, (1987), 33.

36. R. A. Rosenberg, C. R. Wen, K. Tan and J. M. Chen. Enhanced production of excited neutrals following core-to-Rydberg excitation in molecules: tetrachlorosilane. *Phys. Scr.* **41**, (1990), 475.

37. T. Ibuki, N. Washida, U. Ito, Y. Toyoshima and H. Onuki. Absorption spectra of tetrachlorosilane, hexachlorodisilane, methyltrifluorosilane and tetrafluorogermane in the VUV region. *Chem. Phys. Lett.* **136**, (1987), 447.

38. J. A. Tossell and J. W. Davenport. MS-Xa calculation of the elastic electron scattering cross sections and x-ray absorption spectra of CX_4 and SiX_4 (X = H, F, Cl). *J. Chem. Phys.* **80**, (1984), 813.

39. J. S. Tse, Z. F. Liu, J. D. Bozek and G. M. Bancroft. Multiple-scattering X.alpha. study of the silicon and chlorine core-level photoabsorption spectra of silicon tetrachloride. *Phys. Rev. A.* **39**, (1989), 1791.

40. H. Ishikawa, K. Fujima, H. Adachi, E. Miyauchi and T. Fujii. Calculation of electronic structure and photoabsorption spectra of silane, tetrafluorosilane, and tetrachlorosilane (SiH_4, SiF_4, and $SiCl_4$). *J. Chem. Phys.* **94**, (1991), 6740.

41. R. A. Rosenberg and S. P. Frigo. Silicon 2p core-level excitation in condensed tetrachlorosilane. *Chem. Phys. Lett.* **184**, (1991), 439.

42. G. A. Kimmel, T. M. Orlando, C. Vezina and L. Sanche. Low-energy electron-stimulated production of molecular hydrogen from amorphous water ice. *J. Chem. Phys.* **101**, (1994), 3282.

43. G. A. Kimmel and T. M. Orlando. Observation of negative ion resonances in amorphous ice via low-energy (5-40 eV) electron-stimulated production of molecular hydrogen. *Phys. Rev. Lett.* **77**, (1996), 3983.

44. T. M. Orlando, G. A. Kimmel and W. C. Simpson. Quantum-resolved electron stimulated interface reactions: D_2 formation from D_2O films. *Nucl. Instrum. Methods Phys. Res., Sect. B.* **157**, (1999), 183.

45. C. D. Lane and T. M. Orlando. Low-energy electron stimulated desorption of neutrals from multilayers of $SiCl_4$ on Si(111). *J. Chem. Phys.* **124**, (2006), 164702.

46. A. Alexandrov, M. Piacentini, N. Zema, A. C. Felici and T. M. Orlando. Role of excitons in electron- and ehoton-stimulated desorption of neutrals from alkali halides. *Phys. Rev. Lett.* **86**, (2001), 536.

47. F. M. Zimmermann and W. Ho. State resolved studies of photochemical dynamics at surfaces. *Surf. Sci. Rep.* **22**, (1995), 127.

48. S. Arepalli, N. Presser, D. Robie and R. J. Gordon. Detection of chlorine atoms and hydrogen chloride molecules by resonantly enhanced multiphoton ionization. *Chem. Phys. Lett.* **118**, (1985), 88.

49. P. M. Regan, S. R. Langford, D. Ascenzi, P. A. Cook, A. J. Orr-Ewing and M. N. R. Ashfold. Spin-orbit branching in $Cl(^2P)$ atoms produced by ultraviolet photodissociation of HCl. *Phys. Chem. Chem. Phys.* **1**, (1999), 3247.

50. Q. Gao, Z. Dohnalek, C. C. Cheng, W. J. Choyke and J. T. Yates, Jr. The adsorption and surface reaction of $SiCl_4$ on Si(100)-(2x1). *Surf. Sci.* **302**, (1994), 1.

51. L. J. Whitman, S. A. Joyce, J. A. Yarmoff, F. R. McFeely and L. J. Terminello. The chemisorption of chlorosilanes and chlorine on silicon(111)-(7x7). *Surf. Sci.* **232**, (1990), 297.

52. P. Gupta, P. A. Coon, B. G. Koehler and S. M. George. Adsorption and desorption kinetics for tetrachlorosilane on silicon(111)-(7x7). *J. Chem. Phys.* **93**, (1990), 2827.

53. K. T. Lu, J. M. Chen, J. M. Lee, S. C. Ho and H. W. Chang. Production of neutral fragments of gaseous $SiCl_4$ following Si 2p core-level excitation studied by dispersed fluorescence spectroscopy. *Radiat. Phys. Chem.* **75**, (2006), 2058.

54. B. H. Boo, S. M. Park and I. Koyano. Dissociative double ionization following valence and Si:2p core level photoexcitation of $SiCl_4$ in the range 38-133 eV. *J. Phys. Chem.* **99**, (1995), 13362.

55. Q. Guo, D. Sterratt and E. M. Williams. Valence excitation and ESD of Cl^+ ions from the Cl/Si(100) interface. *J. Electron Spectrosc. Relat. Phenom.* **72**, (1995), 31.

56. Q. Guo, D. Sterratt and E. M. Williams. The adsorption and bonding of chlorine at silicon (100) investigated using ESD/ESDIAD with Cl^+ and Cl^- ions. *Surf. Sci.* **356**, (1996), 75.

57. M. T. Sieger, G. K. Schenter and T. M. Orlando. Stimulated desorption by surface electron standing waves. *Phys. Rev. Lett.* **82**, (1999), 3348.

58. M. T. Sieger and T. M. Orlando. Incident beam diffraction in electron stimulated desorption. *Surf. Sci.* **451**, (2000), 31.

59. T. M. Orlando, D. Oh, M. T. Sieger and C. D. Lane. Electron collisions with complex targets: Diffraction effects in stimulated desorption. *Phys. Scr., T.* **T110**, (2004), 256.

60. N. Materer, R. S. Goodman and S. R. Leone. Laser single-photon ionization mass spectrometry measurements of SiCl and $SiCl_2$ during thermal etching of Si(100). *J. Vac. Sci. Technol., A.* **15**, (1997), 2134.

61. W. Muller-Markgraf and M. J. Rossi. The interaction of chlorine($^2P_{3/2}$) and chlorine($^2P_{1/2}$) with n-silicon(100): spontaneous etching. *J. Vac. Sci. Technol., A.* **9**, (1991), 217.

62. N. G. Petrik, K. Knutsen, E. Paparazzo, S. Lea, D. M. Camaioni and T. M. Orlando. Electron beam induced damage of $NaNO_3$ single crystals. An energy, temperature, and quantum state resolved study. *J. Phys. Chem. B.* **104**, (2000), 1563.

63. K. Du, X. Chen and D. W. Setser. Identification of the dichlorosilylene ($SiCl_2$)(~a $^3B_1$-X $^1A_1$) emission system and a flow reactor source of $SiCl_2$(a $^3B_1$). *Chem. Phys. Lett.* **181**, (1991), 344.

64. H. Biehl, K. J. Boyle, D. P. Seccombe, D. M. Smith, R. P. Tuckett, H. Baumgartel and H. W. Jochims. Vacuum-UV fluorescence spectroscopy of CCl_4, $SiCl_4$ and $GeCl_4$ in the range 9-25 eV. *J. Electron Spectrosc. Relat. Phenom.* **97**, (1998), 89.

65. J. Karolczak and D. J. Clouthier. Pyrolysis jet spectroscopy of dichlorosilylene. *Chem. Phys. Lett.* **201**, (1993), 409.

66. D. M. Smith, R. P. Tuckett, K. R. Yoxall, K. Codling, P. A. Hatherly, J. F. M. Aarts and M. Stankiewicz. Use of threshold electron and fluorescence coincidence techniques to probe the decay dynamics of the valence states of CF_4^+, SiF_4^+, $SiCl_4^+$, and $GeCl_4^+$. *J. Chem. Phys.* **101**, (1994), 10559.

67. L. Cooper, L. G. Shpinkova, D. M. P. Holland and D. A. Shaw. A study of the threshold photoelectron spectra and the photoionization yield curves of the silicon tetrahalides. *Chem. Phys.* **270**, (2001), 363.

68. D. M. Smith, R. P. Tuckett, K. R. Yoxall, K. Codling and P. A. Hatherly. Fragmentation of the C^2T_2 and D^2A_1 states of carbon tetrachloride cation (CCl_4^+) and silicon tetrachloride cation ($SiCl_4^+$) studied by threshold photoelectron-photoion coincidence spectroscopy. *Chem. Phys. Lett.* **216**, (1993), 493.

69. T. Ibuki, M. Kono, Y. Asari, A. Hiraya and K. Shobatake. Photoabsorption and fluorescence cross sections of $SiCl_4$ in the region of 6.2-31 eV. *J. Chem. Phys.* **106**, (1997), 4853.

70. L. Cooper, E. E. Rennie, L. G. Shpinkova, D. M. P. Holland and D. A. Shaw. A photoionization mass spectrometry study of the fragmentation of silicon tetrafluoride, tetrachloride and tetrabromide. *Int. J. Mass Spectrom.* **220**, (2002), 359.

71. C. D. Lane, K. R. Shepperd, A. B. Aleksandrov and T. M. Orlando. Electron stimulated desorption of cations from $SiCl_4$ multilayers adsorbed on Si(111). *Surf. Sci.* **593**, (2005), 173.

72. M. Crance. Multiphoton detachment from negative ions of halogens: angular distributions and excess photon absorption. *J. Phys. B.* **21**, (1988), 3559.

73. J. J. Boland and J. S. Villarrubia. Identification of the products from the reaction of chlorine with the silicon(111)-(7x7) surface. *Science*. **248**, (1990), 838.

74. R. Huang, X. Lin, W. Huang, R. Yao, Y. Yu, K. Lin, J. Wei and Z. Zhu. Effect of hydrogen on the low-temperature growth of polycrystalline silicon film deposited by $SiCl_4/H_2$. *Thin Solid Films*. **513**, (2006), 380.

75. Y. Ohshita, K. Yamaguchi, H. Motegi and M. Yamaguchi. Effects of ions and electrons in electron-beam-excited plasma assisted CVD on nanocrystalline silicon film properties. *J. Cryst. Growth*. **237-239**, (2002), 1394.

76. M. De Crescenzi, M. Marucci, R. Gunnella, P. Castrucci, M. Casalboni, G. Dufour and F. Rochet. $Si_{1-x}C_x$ formation by reaction of Si(111) with acetylene: growth mode, electronic structure and luminescence investigation. *Surf. Sci.* **426**, (1999), 277.

77. M. De Crescenzi, R. Bernardini, R. Gunnella and P. Castrucci. Structure and morphology of c-SiC films obtained by acetylene reaction with Si(111) surface. *Solid State Commun.* **123**, (2002), 27.

78. K. Yagi and H. Nagasawa. 3C-SiC growth by alternate supply of SiH_2Cl_2 and C_2H_2. *J. Cryst. Growth*. **174**, (1997), 653.

79. O. Guise, H. Marbach, J. Levy, J. Ahner and J. T. Yates. Electron-beam-induced deposition of carbon films on Si(100) using chemisorbed ethylene as a precursor molecule. *Surf. Sci.* **571**, (2004), 128.

80. D. Klyachko, P. Rowntree and L. Sanche. Oxidation of hydrogen-passivated silicon surfaces induced by dissociative electron attachment to physisorbed H_2O. *Surf. Sci.* **346**, (1996), L49.

81. D. V. Klyachko, P. Rowntree and L. Sanche. Dynamics of surface reactions induced by low-energy electrons. Oxidation of hydrogen-passivated Si by H_2O. *Surf. Sci.* **389**, (1997), 29.

82. W. Di, P. Rowntree and L. Sanche. Energy-selective reaction of the hydrogen-passivated Si surface with carbon tetrafluoride via dissociative electron attachment. *Phys. Rev. B*. **52**, (1995), 16618.

83. J. Xu, W. J. Choyke and J. T. Yates, Jr. Enhanced silicon oxide film growth on Si(100) using electron impact. *J. Appl. Phys.* **82**, (1997), 6289.

84. U. Diebold. The surface science of titanium dioxide. *Surf. Sci. Rep.* **48**, (2003), 53.

85. A. Fujishima and K. Honda. Electrochemical photolysis of water at a semiconductor electrode. *Nature*. **238**, (1972), 37.

86. H. Tang, F. Levy, H. Berger and P. E. Schmid. Urbach tail of anatase TiO_2. *Phys. Rev. B*. **52**, (1995), 7771.

87. A. T. Paxton and L. Thien-Nga. Electronic structure of reduced titanium dioxide. *Phys. Rev. B*. **57**, (1998), 1579.

88. A. L. Linsebigler, G. Lu and J. T. Yates, Jr. Photocatalysis on TiO_2 surfaces: principles, mechanisms, and selected results. *Chem. Rev.* **95**, (1995), 735.

89. M. A. Henderson. The interaction of water with solid surfaces: fundamental aspects revisited. *Surf. Sci. Rep.* **46**, (2002), 1.

90. T. L. Thompson and J. T. Yates, Jr. Surface science studies of the photoactivation of TiO_2-new photochemical processes. *Chem. Rev.* **106**, (2006), 4428.

91. R. Schaub, P. Thostrup, N. Lopez, E. Laegsgaard, I. Stensgaard, J. K. Norskov and F. Besenbacher. Oxygen vacancies as active sites for water dissociation on rutile TiO_2(110). *Phys. Rev. Lett.* **87**, (2001), 266104.

92. M. Li, W. Hebenstreit, U. Diebold, A. M. Tyryshkin, M. K. Bowman, G. G. Dunham and M. A. Henderson. The influence of the bulk reduction state on the surface structure and morphology of rutile TiO_2(110) single crystals. *J. Phys. Chem. B*. **104**, (2000), 4944.

93. V. E. Henrich, G. Dresselhaus and H. J. Zeiger. Observation of two-dimensional phases associated with defect states on the surface of titanium dioxide. *Phys. Rev. Lett.* **36**, (1976), 1335.

94. R. H. Tait and R. V. Kasowski. Ultraviolet photoemission and low-energy electron diffraction studies of titanium dioxide (rutile) (001) and (110) surfaces. *Phys. Rev. B*. **20**, (1979), 5178.

95. I. M. Brookes, C. A. Muryn and G. Thornton. Imaging water dissociation on TiO_2(110). *Phys. Rev. Lett.* **87**, (2001), 266103.

96. R. L. Kurtz, R. Stockbauer, T. E. Madey, E. Roman and J. L. De Segovia. Synchrotron radiation studies of water adsorption on titania(110). *Surf. Sci.* **218**, (1989), 178.

97. S. Krischok, O. Hofft, J. Gunster, J. Stultz, D. W. Goodman and V. Kempter. H_2O interaction with bare and Li-precovered TiO_2. Studies with electron spectroscopies (MIES and UPS(HeI and II)). *Surf. Sci.* **495**, (2001), 8.

98. M. A. Henderson, W. S. Epling, C. H. F. Peden and C. L. Perkins. Insights into photoexcited electron scavenging processes on TiO_2 obtained from studies of the reaction of O_2 with OH groups adsorbed at electronic defects on TiO_2(110). *J. Phys. Chem. B*. **107**, (2003), 534.

99. C. Di Valentin, G. Pacchioni and A. Selloni. Electronic structure of defect states in hydroxylated and reduced rutile TiO_2(110) Surfaces. *Phys. Rev. Lett.* **97**, (2006), 166803.

100. K. Onda, B. Li, J. Zhao, D. Jordan Kenneth, J. Yang and H. Petek. Wet electrons at the H_2O/TiO_2(110) surface. *Science*. **308**, (2005), 1154.

101. B. Li, J. Zhao, K. Onda, K. D. Jordan, J. Yang and H. Petek. Ultrafast interfacial proton-coupled electron transfer. *Science*. **311**, (2006), 1436.

102. Z. Zhang, O. Bondarchuk, B. D. Kay, J. M. White and Z. Dohnalek. Imaging Water Dissociation on TiO_2(110): Evidence for inequivalent geminate OH groups. *J. Phys. Chem. B*. **110**, (2006), 21840.

103. N. G. Petrik and G. A. Kimmel. Electron-stimulated production of molecular hydrogen at the interfaces of amorphous solid water films on Pt(111). *J. Chem. Phys.* **121**, (2004), 3736.

104. N. G. Petrik and G. A. Kimmel. Electron-stimulated reactions in thin D_2O films on Pt(111) mediated by electron trapping. *J. Chem. Phys.* **121**, (2004), 3727.

105. J. T. Yates, Jr. *Experimental Innovations in Surface Science*. Springer, New York, (1998).

106. M. B. Hugenschmidt, L. Gamble and C. T. Campbell. The interaction of H_2O with a TiO_2(110) surface. *Surf. Sci.* **302**, (1994), 329.

107. M. A. Henderson. An HREELS and TPD study of water on TiO_2(110): the extent of molecular versus dissociative adsorption. *Surf. Sci.* **355**, (1996), 151.

108. M. L. Knotek and P. J. Feibelman. Ion desorption by core-hole auger decay. *Phys. Rev. Lett.* **40**, (1978), 964.

109. P. J. Feibelman and M. L. Knotek. Reinterpretation of electron-stimulated desorption data from chemisorption systems. *Phys. Rev. B*. **18**, (1978), 6531.

110. M. L. Knotek. Characterization of hydrogen species on TiO_2 by electron-stimulated desorption. *Surf. Sci.* **91**, (1980), L17.

111. S. Suzuki, K. Fukui, H. Onishi and Y. Iwasawa. Hydrogen adatoms on TiO_2(110)-(1 x 1) characterized by scanning tunneling microscopy and electron stimulated desorption. *Phys. Rev. Lett*. **84**, (2000), 2156.

112. O. Bikondoa, C. L. Pang, R. Ithnin, C. A. Muryn, H. Onishi and G. Thornton. Direct visualization of defect-mediated dissociation of water on TiO_2(110). *Nature Materials*. **5**, (2006), 189.

113. W. S. Epling, C. H. F. Peden, M. A. Henderson and U. Diebold. Evidence for oxygen adatoms on TiO_2(110) resulting from O_2 dissociation at vacancy sites. *Surf. Sci.* **412/413**, (1998), 333.

114. M. A. Henderson, W. S. Epling, C. L. Perkins, C. H. F. Peden and U. Diebold. Interaction of molecular oxygen with the vacuum-annealed TiO_2(110) surface: molecular and dissociative channels. *J. Phys. Chem. B*. **103**, (1999), 5328.

115. G. A. Kimmel and T. M. Orlando. Low-energy (5-120 eV) electron-stimulated dissociation of amorphous D_2O ice: $D(^2S)$, $O(^3P_{2,1,0})$, and $O(^1D_2)$ yields and velocity distributions. *Phys. Rev. Lett.* **75**, (1995), 2606.

116. G. A. Kimmel, R. G. Tonkyn and T. M. Orlando. Kinetic and internal energy distributions of molecular hydrogen produced from amorphous ice by impact of 100 eV electrons. *Nucl. Instrum. Methods Phys. Res., Sect. B.* **101**, (1995), 179.

117. N. G. Petrik, A. G. Kavetsky and G. A. Kimmel. Electron-stimulated production of molecular oxygen in amorphous solid water. *J. Phys. Chem. B.* **110**, (2006), 2723.

118. P. Rowntree, L. Parenteau and L. Sanche. Electron stimulated desorption via dissociative attachment in amorphous water. *J. Chem. Phys.* **94**, (1991), 8570.

119. R. H. Stulen and P. A. Thiel. Electron-stimulated desorption and thermal desorption spectrometry of water on nickel(111). *Surf. Sci.* **157**, (1985), 99.

120. P. A. Thiel and T. E. Madey. The interaction of water with solid surfaces: fundamental aspects. *Surf. Sci. Rep.* **7**, (1987), 211.

121. C. L. Pang, O. Bikondoa, D. S. Humphrey, A. C. Papageorgiou, G. Cabailh, R. Ithnin, Q. Chen, C. A. Muryn, H. Onishi and G. Thornton. Tailored TiO_2(110) surfaces and their reactivity. *Nanotechnology*. **17**, (2006), 5397.

122. M. L. Knotek and P. J. Feibelman. Ion desorption by core-hole Auger decay. *Phys. Rev. Lett.* **40**, (1978), 964.

123. P. J. Feibelman and M. L. Knotek. Reinterpretation of electron-stimulated desorption data from chemisorption systems. *Phys. Rev. B.* **18**, (1978), 6531.

124. L.-Q. Wang, D. R. Baer and M. H. Engelhard. Creation of variable concentrations of defects on TiO_2(110) using low-density electron beams. *Surf. Sci.* **320**, (1994), 295.

125. C. L. Perkins and M. A. Henderson. Photodesorption and trapping of molecular oxygen at the TiO_2(110)-water ice interface. *J. Phys. Chem. B.* **105**, (2001), 3856.

126. W. Zheng, D. Jewitt and R. I. Kaiser. Temperature dependence of the formation of hydrogen, oxygen, and hydrogen peroxide in electron-irradiated crystalline water ice. *Astrophys. J.* **648**, (2006), 753.

127. A. Tilocca, C. Di Valentin and A. Selloni. O_2 interaction and reactivity on a model hydroxylated rutile(110) surface. *J. Phys. Chem. B.* **109**, (2005), 20963.

128. C. Zhang and P. J. D. Lindan. A density functional theory study of the coadsorption of water and oxygen on TiO_2(110). *J. Chem. Phys.* **121**, (2004), 3811.

129. C. Laffon, S. Lacombe, F. Bournel and P. Parent. Radiation effects in water ice: A near-edge x-ray absorption fine structure study. *J. Chem. Phys.* **125**, (2006), 204714.

130. A. Tilocca, C. Di Valentin and A. Selloni. O_2 interaction and reactivity on a model hydroxylated rutile(110) surface. *J. Phys. Chem. B*. **109**, (2005), 20963.

131. C. R. Claydon, G. A. Segal and H. S. Taylor. Theoretical interpretation of optical and electron scattering spectra of H_2O. *J. Chem. Phys*. **54**, (1971), 3799.

132. R. H. Stulen and P. A. Thiel. Electron-stimulated desorption and thermal desorption spectrometry of H_2O on nickel(111). *Surf. Sci.*. **157**, (1985), 99.

133. D. M. Chipman. Excited electronic states of small water clusters. *J. Chem. Phys*. **122**, (2005), 044111.

134. R. J. Sension, R. J. Brudzynski and B. S. Hudson. Resonance raman studies of the low-lying dissociative rydberg-valence states of H_2O, D_2O, and HDO. *Phys. Rev. Lett*. **61**, (1988), 694.

135. M. A. Henderson. Structural sensitivity in the dissociation of water on TiO_2 single-crystal surfaces. *Langmuir*. **12**, (1996), 5093.

136. R. A. Baragiola, R. A. Vidal, W. Svendsen, J. Schou, M. Shi, D. A. Bahr and C. L. Atteberrry. Sputtering of water ice. *Nucl. Instrum. Methods Phys. Res., Sect. B*. **209**, (2003), 294.

137. N. G. Petrik and G. A. Kimmel. Electron-stimulated sputtering of thin amorphous solid water films on Pt(111). *J. Chem. Phys.* **123**, (2005), 054702.

138. N. G. Petrik and G. A. Kimmel. Electron-stimulated reactions at the interfaces of amorphous solid water films driven by long-range energy transfer from the bulk. *Phys. Rev. Lett.* **90**, (2003), 166102.

139. K. Onda, B. Li and H. Petek. Two-photon photoemission spectroscopy of TiO_2(110) surfaces modified by defects and O_2 or H_2O adsorbates. *Phys. Rev. B*. **70**, (2004), 045415.

140. M. Anpo, K. Chiba, M. Tomonari, S. Coluccia, M. Che and M. A. Fox. Photocatalysis on native and platinum-loaded titanium dioxide and zinc oxide catalysts. Origin of different reactivities on wet and dry metal oxides. *Bull. Chem. Soc. Jpn.* **64**, (1991), 543.

141. V. Montgomery and R. H. Williams. The adsorption of water on indium phosphide and its influence on Schottky barrier formation. *J. Phys. C*. **15**, (1982), 5887.

142. V. P. Avdonin, I. A. Vasiliev, A. F. Nechaev and B. T. Plachenov. *Efficiency of electron-hole pairs and excitons production in alkali-halide crystals*. Proceedings of the LSSR Academy of Sciences, (1973).